SUBSTITUENT EFFECTS ON THE LUMINESCENT PROPERTIES OF EUROPIUM β-DIKETONATE COMPLEXES WITH DIPYRIDOPHENAZINE LIGANDS: A DENSITY FUNCTIONAL THEORY STUDY

A thesis presented to the faculty of the Department of Chemistry and Physics of Western Carolina University in partial fulfillment of the requirements for the degree of Masters of Science in Chemistry.

By

Christian Jensen

Advisor: Dr. Channa De Silva
Associate Professor of Chemistry
Department of Chemistry & Physics

Committee Members: Dr. David Evanoff, Chemistry & Physics
Dr. Scott Huffman, Chemistry & Physics

April 2017

ACKNOWLEDGMENTS

TABLE OF CONTENTS

LIST OF TABLES

LIST OF FIGURES

ABSTRACT

SUBSTITUENT EFFECTS ON THE LUMINESCENT PROPERTIES OF EUROPIUM β-DIKETONATE COMPLEXES WITH DIPYRIDOPHENAZINE LIGANDS: A DENSITY FUNCTIONAL THEORY STUDY

Christian Jensen

Western Carolina University (April 2017)

Advisor: Dr. Channa De Silva

A great deal of attention is devoted to creating and characterizing new and novel luminescent lanthanide complexes due to their impressive luminescent characteristics. Unique properties include line like emission bands, long luminescent life times, and large Stokes shifts, making lanthanides ideal for applications such as organic light emitting diodes, sensor technology, biomedical assays, biomedical imaging, and LASER technology. Lanthanides by themselves, though, suffer from low molar absorptivities as a result of quantum mechanically forbidden electric dipole transitions. To overcome these limitations, 'antenna' ligands are coordinated to the Ln(III) ion in order to sensitize lanthanide absorption by a series of energy transfer processes. Factors essential in controlling the efficiency of ligand sensitization are the ligand based singlet S_1 and triplet T_1 state energies. By controlling the substituents of the neutral donor ligand, we can effectively tune these energy levels. This study uses density functional theory (DFT) and time-dependent density functional theory (TD-DFT) to investigate the electronic properties of a series of Eu(TTA)DPPZ-R (R = H, NH_2, Br, CO_2H, $CO_2CH_2CH_3$, CO_2CH_3, OCH_3, CH_3, and NO_2) complexes where TTA = thenoyltrifluoroacetone, DPPZ = dipryrido[3,2-a:2′,3′-c] phenazine. DFT-optimized molecular structures agree within the experimental values. The results of the computational study reveal that

the electron withdrawing substituent groups decrease the intersystem crossing ΔE_{ISC} and energy transfer ΔE_{ET} energy gap with respect to unsubstituted DPPZ. Electron donating substituent groups will increase the ΔE_{ISC} and ΔE_{ET} energy gaps. Absorption spectra calculations show good agreement with available experimental absorption data. Luminescent quantum yield measurements of the complexes decreases with decreasing ΔE_{ISC} and ΔE_{ET}.

CHAPTER 1: INTRODUCTION

The properties of the lanthanides impart unique spectroscopic properties that can be exploited for use in a multitude of technologies. In the review article by Bünzli and Piguet[5] the authors layout a comprehensive accounting of the uses in which luminescent lanthanide complexes have been utilized. Examples of which are many different types of sensors[6], organic light emitting diodes[7], bioassays[8,9], solar cells[10], and imaging technology[11]. A combined approach of experiment and theory to aid in understanding the underlying electronic properties of these types of systems helps to facilitate continued improvement in current technologies and development of novel complexes with improved optical properties.

Luminescent europium complexes generally have octa-cordination geometry, and the type of ligands that surround the europium ion can affect the luminescent properties of the complex. One of the most widely studied systems is Eu(III) with ternary β-diketonate (β-DK) ligands and a conjugated heterocyclic chromophore coordinated around the europium ion. The β-DK ligands deprotonate an alpha hydrogen and act as Lewis bases while the chromophore ligand forms a dative bond between the metal center and two lone pairs of electrons of a nitrogen atom such as in phenanthroline derivatives. The ligands chosen for this project are the β-DK thenoyltrifluoroacetone (TTA) and the phenanthroline derivative dipryrido[3,2-a:2′,3′-c] phenazine (DPPZ).
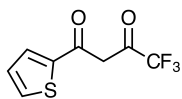
(a) Molecular structure of TTA
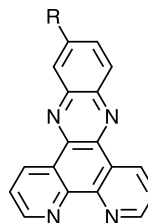
(b) Molecular structure of DPPZ

Figure 1: Structure of thenoyltrifluoroacetone and dipryrido[3,2-a:2′,3′-c] phenazine.

The use of β-DK ligands has received a good deal of attention because they posses desirable luminescent properties especially in the use of optoelectronic devices, but also because of their ability to transfer energy to other ligands particularly the neutral donor ligand. In the study by Freund et $al.$[12] the authors modified the β-diketone TTA by making substitutions to the thiophene part of the molecule. The substituent groups used to modify TTA were bromine (Br-TTA), 1-bromo octyl (BrC8-TTA), and methyl thiophene (MeT-TTA). The authors also made the modification of replacing the trifluoro methyl group with a second thiophene group (DTDK). These series of modified TTA ligands were coordinated to europium with phenanthroline as the neutral donor ligand with reported thin films and solution phase photoluminescence quantum yields.

Table 1: Reported photoluminescent quantum yields reported in Freund.

Complex	Thin Film	Solution
Eu(TTA)$_3$Phen	0.72	0.48
Eu(TTA)$_3$Phen	0.34	0.37
Eu(TTA)$_2$(Br-TTA)Phen	0.41	0.43
Eu(BrC8-TTA)$_3$Phen	0.41	043
Eu(MeT-TTA)$_3$Phen	> 0.01	> 0.01
Eu(DTDK)$_3$Phen	> 0.01	> 0.01

The results reported by Freund show that the unmodified TTA ligand gives the highest phtoluminescent quantum yields.

The choice of the neutral donor ligand such as phenanthroline derivatives is equally important to the function and luminescent properties of these complexes. Not only does the chromophore ligand need to have resonant energy levels that are able to accept charge transfer from the β-DK ligands but the accepting state (typically a triplet state) must have good resonance with europium's excited states. In addition to good resonant energy levels, an ideal neutral donor ligand would also minimize the amount of energy that is lost through non-radiative processes such as molecular vibrations. Furthermore, certain applications demand

the use of these conjugated phenanthroline derivatives. For example, Dasari and Patra[13] found that terbium and europium complexes of DPPZ, upon partial intercalation into DNA, both increased emission intensity and formed reactive oxygen species. These reactive oxygen species are known to actively damage DNA so that these complexes could potentially be used in therapeutic cancer treatments.

Europium β-diketonate phenanthroline complexes have experimentally demonstrated favorable light conversion capabilities. Regardless, experimental design can be costly in both specialized equipment and time often yeilding minimal results. The use of computational methods to determine ground and excited state properties can help guide project direction. The use of computational methods has been successfully utilized in determining the ground state properties of luminescent lanthanide complexes including vibrational frequencies, raman spectra, and absorption predictions.

In Greco $et.al.$[14] density functional techniques were used to investigate a series of europium thiophene based β-DK complexes (TTA, DTDK, Br-TTA, and MeT-TTA) phenanthroline complexes. Their study revolved around how specific dependence of the β-DK ligands affects these complexes structural and electronic properties. Their study used hybrid PBE1PBE and CAM-B3LYP exchange-correlation functionals and the 6-31G* basis set. The europium ion used the Stuttgart-Dresden[15] large-core quasi-relativistic effective core potential (ECP) with the related [5s4p3d]-GTO valence basis set. Excitation energies were found by the ΔSCF method. The authors found that of the four thiophene based β-DK ligands and spectroscopic properties of TTA, DTDK, and Br-TTA are well reproduced when comparing their results with experimentally available crystal structures and absorption data. The authors faced difficulty in their comparison with MeT-TTA stemming from experimental inconsistencies. Greco et al. concluded that their computational methods reproduced well the triplet state energy levels these complexes.

In Li $et\ al.$[16] DFT techniques were used to investigate the effect that variation on lig-

and size of substituted phenanthroline complexes has on the luminescent properties of the corresponding Eu(III) complexes. Calculations were performed using the B3LYP exchange-correlation functional with the 6-31G basis set for C and H and the 6-31G* basis set for N, O, S, and F. Europium is modeled using the Stuttgart-Dresden large-core ECPs with an optimized [7s6p5d][5s4p3d]-GTO valence basis set. Li found that the highest occupied molecular orbital (HOMO) energy, and the lowest unoccupied molecular orbital (LUMO) energy would increases as a result of increasing the number of methyl groups. Li also found in that same study that a significant decrease in the LUMO energy occurs with increased conjugation. The increase conjugation had negligible effect on the HOMO energy. The authors also found that the larger neutral donor ligands DPPZ, 11-methylpyrazino[3,2a:2'3'c]phenazine, 11,12-dimethylpyrazino[3,2a:2'3'c]phenazine, and benzo [i]dipyrido[3,2-a:2'3'-c]phenazine lead to incomplete energy transfer from the ligand based triplet state to the $^5D_0$ level of Eu(III).

In Nolasco et $al.$[10] density functional methods were used to model a series of Eu(III) complexes by varying the substitutions on the phenanthroline ligand. The authors use the B3LYP exchange-correlation functional and the 6-31G and 6-31G*basis sets. For the Eu(III) ion the Stuttgart-Dresden large-core ECPs were employed. Time-dependent DFT calculations were performed on the optimized geometries. All calculations were done in the gas phase. The authors found that absorption band position and transition characteristics is affected by different ligand substituents. The authors also reported that the substituents influence through the conjugation of the phenanthroline ligand effectively tune the triplet state.

In the project presented in this thesis, a systematic computational study is conducted on Eu(TTA)$_3$DPPZ-R (R = Br-, CH$_3$-, CH$_3$O-, CH$_3$CH$_2$COOC-, CH$_3$COOC-, NH$_2$-, NO$_2$-) complexes to see how the addition of substituent groups with varying electron donating and electron withdrawing capabilities modify the molecular orbital, excited state structure, and luminescent properties of the overall complexes. Ground state geometries are determined

and compared with crystal structure geometries where available. Ground state geometries are used in excited state calculations to determine lowest singlet and triplet energies of the complexes to compare with experimental absorption data where available. A final comparison of calculated data and quantum yield data will help give insight on how the substituents affect the luminescent properties of these complexes.

CHAPTER 2: BACKGROUND

2.1   Lanthanide Luminescence

The goal of this project is to help guide experimental design of europium based luminescent complexes using theoretical and computational techniques. Knowledge of the lanthanides, and their luminescent properties have been known of for a long time. Also known for some time is their unique spectroscopic properties such as narrow emission band widths, large Stokes shifts, and long luminescent lifetimes. These properties make them ideal for a plethora of applications especially in the fields of engineering and biology.

The electronic ground state of the lanthanides have the form $[\text{Xe}]4f^n6s^2$, where $n = 0-14$, except for lanthanum, cerium, gadolinium, and lutetium which have a $[\text{Xe}]4f^{n-1}5d^16s^2$ electronic configuration. The most common oxidation state for the lanthanides is Ln(III) with ground state electronic configuration of $[\text{Xe}]4f^{n-1}$. For Eu(III) the electronic ground state $[\text{Xe}]4f^6$ giving Eu(III) a less than half filled $4f$ shell. As a result of the poor shielding of the core electrons the $4f$ orbitals, which are the valence orbitals, have a radial distribution which is less than the filled $5s$ and $5p$ orbitals. It is this particular feature of the lanthanides which impart such unique luminescent and spectroscopic properties.

Moving from the overall electronic structure of the lanthanides, a discussion of the finer internal structure of the electrons or the microstates is necessary. A microstate is the particular arrangements of the electrons within any valence orbital. Mathematically it can be thought of as a permutation but with the caveat that certain states are allowed and certain states are not. Considering the Eu(III) ion with it's six valence electrons, the number of states attainable according to the combinatorial formula where m is the number of spin

8

orbitals and n is the number of electrons is

$$\frac{m!}{n!(m-n)!} = \frac{14!}{6!(14-6)!} = 3003 \tag{1}$$

microstates. The work of Friedrich Hund developed a series of rules for finding the ground state term of a multi electron system. These rules are[17],

1. The ground state term has the largest spin multiplicity

2. The ground state term has the largest orbital multiplicity

3. If $n < (2l+1)$, then $J = J_{min}$; else if $n > (2l+1)$, then $J = J_{max}$

Certain approximations for the coupling of orbital and spin angular momentum make it possible to identify the ground state electronic structure of Eu(III) ions.

The are several schemes in which the spin and orbital angular momenta couple which include LS coupling, jj coupling, or coupling schemes utilizing group theory of symmetric molecules[17]. In LS or Russell-Saunders coupling the total angular momentum J is formed from the sum of the total spin angular momentum S and the total orbital angular momentum L

$$J = L + S \tag{2}$$

where S is the sum of individual spin angular momenta

$$S = \sum_i s_i. \tag{3}$$

and L is the sum of individual orbital angular momenta

$$L = \sum_i l_i. \tag{4}$$

9

This coupling scheme is useful for lighter elements where individual couplings to do not have as great of an effect due to the size and charge on the nucleus.

For heavier elements the jj coupling scheme is utilized. In the jj coupling scheme there is more emphasis on how the individual spin and orbital angular momentum couple. The total angular momentum J is formed from the individual total angular momenta

$$J = \sum_i j_i \tag{5}$$

where each individual total angular momentum is formed from individual combinations of spin and orbital angular momenta

$$j_i = \sum_i (l_i + s_i). \tag{6}$$

For the Eu(III) ion, the ground state term symbol is formed as follows. For the $4f$ orbitals the principle quantum number $n = 4$ means that the orbital angular momentum can take the values $l = 0, 1, 2, 3$. Since the $4f$ orbitals are shielded from the outside by the inner $5s$ and $5p$ orbitals crystal field splitting of the $4f$ orbitals is minimized to virtually nothing which implies that the ion is in a high spin state with six unpaired electrons giving a total spin angular momentum of $S = 3$. The degeneracy of the $4f$ orbitals is lifted by Coulombic effects, the crystal field to a lesser extent, and spin-orbit coupling to the greatest extent. A spectroscopic term describing a atomic state takes the form

$$^{2S+1}L_J$$

where $2S+1$ is the spin multiplicity, L is the total orbital angular momentum in spectroscopic notation, and J is values for the total angular momentum. Given these details and the fact that $J = 0, 1, 2, 3, 4, 5, 6$ the atomic ground state for Eu(III) is split into the following terms

in Figure 2.

$$^{7}F_{0}, {}^{7}F_{1}, {}^{7}F_{2}, {}^{7}F_{3}, {}^{7}F_{4}, {}^{7}F_{5}, {}^{7}F_{6}$$

Figure 2: Term symbols for Eu(III)'s ground state, who's degeneracy is broken by spin-orbit interacttions.

All of these terms are able to be observed experimentally.

The excitation of the lanthanides in the gas phase are primarily the result of j-j induced dipole transitions. Note that the topology of the $4f$ orbitals has spherical symmetry which means that under inversion parity does not change. The electric dipole tensor operator, however, transforms with odd parity therefore these particular excitations are forbidden under the Laporte selection rule. This rule asserts that within a molecule or atom whose orbitals have an inversion center (spherical symmetry has an inversion center) electronic excitation must conserve parity. In terms of a group theoretic argument where g is even parity and u is odd parity, under excitation a $g \rightarrow g$ and $u \rightarrow u$ transitions are forbidden and $g \rightarrow u$ and $u \rightarrow g$ transitions are allowed.

In the table below are transitions from the $^{5}D_{0}$ excited state to the various levels of europium's ground state together with the transition type of electric dipole (ED) or magnetic dipole (MD) and the energy range of those transitions. As can be seen from Table 2 the predominant type of transition is an electric dipole transition which must conserve parity.

Table 2: Excited state transitions of Eu(III) ion, the transition character, and the energy range to the transition[1].

Transition	Transition Character	Energy Range (nm)
$^{5}D_{0} \rightarrow {}^{7}F_{0}$	ED	570 - 585
$^{5}D_{0} \rightarrow {}^{7}F_{1}$	MD	585 - 600
$^{5}D_{0} \rightarrow {}^{7}F_{2}$	ED	600 - 630
$^{5}D_{0} \rightarrow {}^{7}F_{3}$	ED	640 - 660
$^{5}D_{0} \rightarrow {}^{7}F_{4}$	ED	680 - 710
$^{5}D_{0} \rightarrow {}^{7}F_{5}$	ED	740 - 770
$^{5}D_{0} \rightarrow {}^{7}F_{6}$	ED	810 - 840

The strong electric dipole $^5D_0 \rightarrow ^7F_2$ transition for the Eu(III) ion is what is known as a hypersensitive transition. The intensity of this band is dependent upon the site symmetry and induced by the lack of inversion symmetry at the Eu(III) site[18]. Figure 3 shows the $^5D_0 \rightarrow ^7F_{J=0,1,2,3}$ transitions.
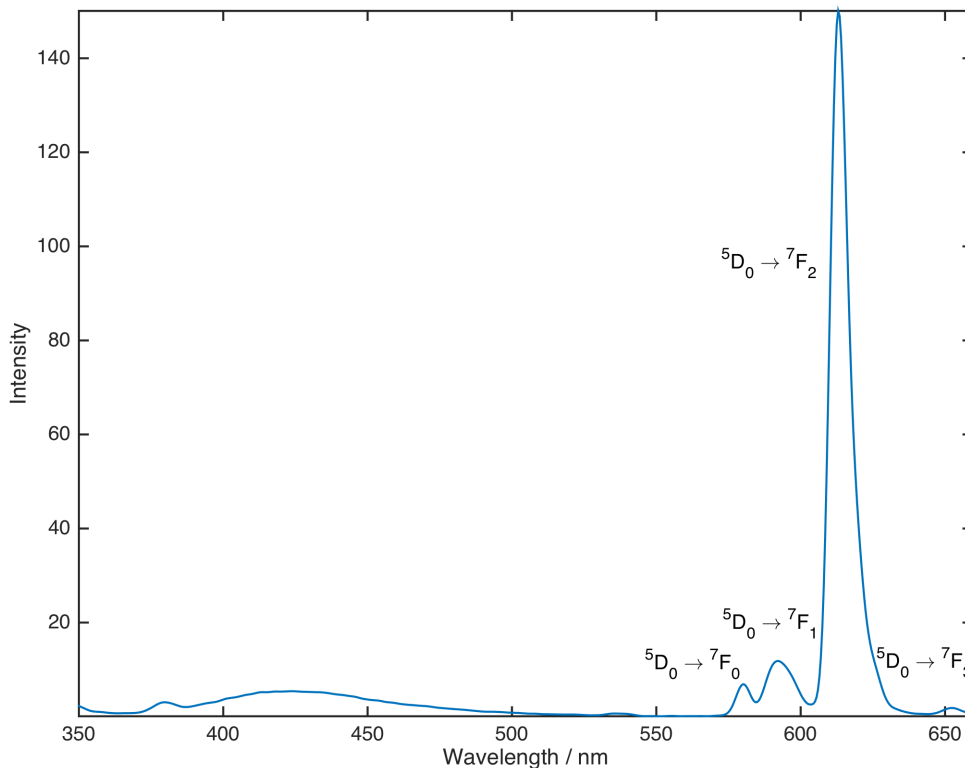
Figure 3: Luminescence of Eu(TTA)$_3$DPPZ displaying the $^5D_0 \rightarrow ^7F_{J=0,1,2,3}$ transitions. The $^5D_0 \rightarrow ^7F_{J=5,6}$ transitions are usually not observed primarily due to detection limits.

Lanthanide ions by themselves have particularly low molar absorptivities owing to the above discussion on the nature of the $4f$ orbitals, and its interaction with an applied electric field. Relaxing of the selection rules can be accomplished by changing the coordination environment to one that is not spherically symmetric so that mixing of the total angular momentum occurs via crystal field interactions[19,20]. By controlling the the coordination environment the efficiency with which light may be absorbed and re-emitted can be manipulated.

12

Quantifying that process, which is the topic of the next section, involves an understanding of the pathways in which energy may be transferred.

2.2 Luminescent Quantum Yields

Lanthanide metals have unique spectroscopic properties due to their shielding of the $4f$ orbitals as was explained in the previous section. Ligand resonance with europium's excited states help to populate europium's $^5D_1$ and $^5D_0$ excited states. As a means to quantify the efficiency of energy conversion, quantum yield experiments are performed. The quantum yield of a luminescent metal or complex is defined as the ratio of the amount of light emitted to the amount of light absorbed. The efficiency with which this process occurs is a balance between radiative and non-radiative pathways and the mechanisms that dictate these processes. For a generalized europium complex the process is illustrated in the following figure.
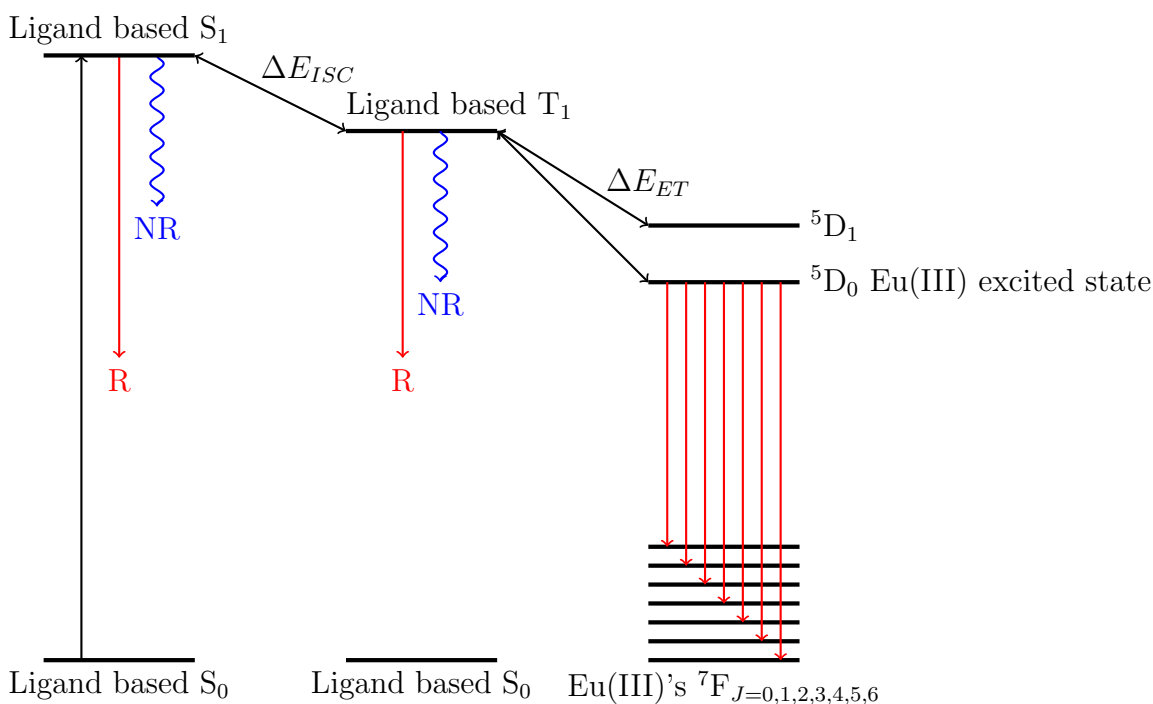
Figure 4: Energy pathway of ligand excitation showing possible routs of radiative (R) and non-radiative (NR) de-excitation and energy back transfer.

For ligand sensitized europium complexes, there are two main processes that contribute to the degree to which lanthanide emission will occur. The first process to be discussed is what is refered to as ligand sensitization η_{sens}.

This process is initiated by initial absorption of ultraviolet light into a ligand based singlet state. The ligand based singlet state may then transfer energy in several different pathways. The singlet state may undergo emission of photon in a fluorescence event. In general any kind of emission event is referred to as radiative deactivation. The ligand may also deactivate the excited state by bond vibrations as well as molecular collisions. These types of processes are referred to as non-radiative processes in order to contrast it with the aforementioned process. The last pathway for deactivation comes in the form an intersystem crossing where charge is transferred from a ligand based singlet state to a ligand based triplet state due to resonance between the two states. These two states can show greater or lesser coupling with careful choice of coordinated ligands.

Intersystem crossing places energy into the ligand based triplet state. Because the charge is still primarily centered on the ligands similar radiative and non-radiative deactivation processes may still occur. There is now one very distinct difference between this state and the singlet state. This difference arises from two new pathways in the form of charge back transfer to the previously occupied singlet state or charge transfer into europium's $^5D_0$ or $^5D_1$ excited states, commonly referred to as a ligand to metal charge transfer (LMCT).

Charge transfer into europium's $^5D_0$ or $^5D_1$ excited states can be deactivated in one of two ways. There is the probability of energy back-transfer into the ligand based triplet state if europium's excited states and the ligand based triplet state are closely matched in energy. The second deactivation pathway is by the characteristic europium emission at 614 nm due to the $^5D_0 \rightarrow ^7F_2$ transition. This transition is associated with an electric dipole transition and is the most dominant in europium's emission spectrum. There are other weaker contributions to europium's emission spectrum from weak magnetic dipole transitions, but the primary

contribution to the luminescence of these complexes comes from the $^5D_0 \rightarrow ^7F_2$ transition.

The overall process of ligand sensitization promoting europium luminescence is commonly referred to as the 'antenna' effect. The antenna effect is a the phenomenon of increased photoluminescence as a result of the resonance between ligand electronic states and europium excited states. This with the intrinsic europium emission constitutes the overall quantum yield for the complex

$$\Phi_{total} = \eta_{sens}\Phi_{Ln} \tag{7}$$

The overall quantum yield, Φ_{total} due to ligand sensitization is the probability of emission given a photon was absorbed. This problem is described mathematically as the product of emission from ligand absorption, η_{sens} and the intrinsic quantum yield of the trivalent europium ion, Φ_{Ln}.

There are two methods in which to determine the quantum yield of an emitting compound. Absolute quantum yields are a direct measure of quantum efficiency using an integrating sphere. This setup can be costly since integrating spheres are generally not standard laboratory equipment. Quantum yield measurements by reference, on the other hand, needs only a UV-Vis and fluorescence spectrometer. These measurements compare the absorption and fluorescence emission of a sample and reference fluorophore by equation 8

$$\Phi = \Phi_{ref}\frac{A_{ref}I_s\eta_s^2}{A_sI_{ref}\eta_{ref}^2} \tag{8}$$

where Φ_{ref} is the quantum yield of the known standard, A_{ref} and A_s are the absorption measurements of the reference and sample respectively, I_{ref} and I_s is the integrated emission area of the reference and sample respectively, and η_{ref} and η_s is the refractive index of the reference and sample solvent respectively.

2.3 Density Functional Theory

The beginning of the twentieth century bore witness to the quantum revolution in physics. The secrets of the atom were being unraveled and new ideas in physics were necessary. The result was the inception of the wave function of Erwin Schrödinger and the eigenvalue equation that bears his name. In the most general exposition of his formulation time is considered and is usually represented as:

$$-\frac{\hbar}{i}\frac{\partial}{\partial t}\Psi(\mathbf{x}, t) = H\Psi(\mathbf{x}, t) \tag{9}$$

where $\Psi(\mathbf{x}, t)$ is the wave function, a function of spatial and time variables, $\hbar$ is Dirac's constant, and H is Hamiltonian. Understanding of what the wave function is was not so intuitive as the wave function has no physical meaning, has no physical observable. And so working independently Llewellyn Thomas[21] and Enrico Fermi[22] developed a theory using the concept of the charge density, $\rho(\mathbf{r}) = \frac{Q}{V}$ (the amount of charge per unit volume). The charge density was intuitive and had physical meaning. Furthermore, since charge is quantized, an integration over all space of electron density will yield the total number of electrons

$$\int \rho(\mathbf{r})d\mathbf{r} = N. \tag{10}$$

The Born-Oppenheimer[23] approximation calculates the energy of a system with fixed nuclear coordinates. Looking at the energy of the system as a function of nuclear positions (the potential energy surface) the nuclei would correspond to local maxima. The implication of which is that analysis of the potential energy surface of the electron density can be used to form the Hamiltonian, which can be used to solve the Schrödinger equation to determine the wave functions and the energy eigenvalues.

Their method relied upon separating the kinetic and potential energies. The simplest

approximation of which comes from classical mechanics where the potential energies are relatively straightforward in determining using Coulomb's law. The potential energy due to interactions between the nuclei and the electron density is attractive and is represented by:

$$V_{ne}[\rho(\mathbf{r})] = \sum_k^N \int \frac{Z_k}{|\mathbf{r} - \mathbf{r}_k|} \rho(\mathbf{r}) d\mathbf{r} \tag{11}$$

where Z_k is the charge on the nucleus, r_k is the nuclear spatial coordinates, integration is performed over all space and the sum runs from the kth nucleus over all electrons N. The potential energy from self-repulsion of a classical charge distribution is represented as:

$$V_{ee}[\rho(\mathbf{r})] = \frac{1}{2} \int \int \frac{\rho(\mathbf{r}_1)\rho(\mathbf{r}_2)}{|\mathbf{r}_1 - \mathbf{r}_2|} d\mathbf{r}_1 d\mathbf{r}_2. \tag{12}$$

The above term is indicative of the repulsion potential experienced by two particles of the same charge. Having addressed the two typed of potential energy associated with this formulation only the kinetic energy term is left to be determined. What is left is to determine the kinetic energy term of a continuous charge distribution. The model assumes a uniformly distributed positive charge in an infinite volume of space occupied by an infinite number of electrons and has a constant non-zero electron density. This assumption is what is known as the uniform electron gas (UEG). Then, following from fermion statistical mechanics, the kinetic energy term for a UEG is:

$$T_{UEG}[\rho(\mathbf{r})] = \frac{3}{10}(3\pi^2)^{2/3} \int \rho^{5/3}(\mathbf{r}) d\mathbf{r} \tag{13}$$

The total energy equation can now be written as:

$$E[\rho(\mathbf{r})] = V_{ne}[\rho(\mathbf{r})] + V_{ee}[\rho(\mathbf{r})] + T_{UEG}[\rho(\mathbf{r})] \tag{14}$$

and, along with an assumed variational principle, represents a first attempt at formulating a quantum theory using the density as the basic variable or rather a density functional theory (DFT).

It would be nice if the theory was complete as it is but there are some major flaws associated with some of the assumptions that were used. The electron-electron repulsion potential is only an approximation as a result of the omission of exchange and correlation terms. The correlation energy arises from treating each electron in an average field of all other electrons, and the exchange energy arises from the antisymmetric properties of fermionic particles such as electrons. Introducing a 'hole' function, $h(\mathbf{r}_1; \mathbf{r}_2)$ is one way of accounting for errors associated with exchange and correlation written:

$$\left\langle \Psi \Big| \sum_{i<j}^{N} \frac{1}{r_{ij}} \Big| \Psi \right\rangle = \frac{1}{2} \int \int \frac{\rho(\mathbf{r}_1)\rho(\mathbf{r}_2)}{|\mathbf{r}_1 - \mathbf{r}_2|} d\mathbf{r}_1 d\mathbf{r}_2 + \frac{1}{2} \int \int \frac{\rho(\mathbf{r}_1)h(\mathbf{r}_1; \mathbf{r}_2)}{|\mathbf{r}_1 - \mathbf{r}_2|} d\mathbf{r}_1 d\mathbf{r}_2 \qquad (15)$$

where the left hand side is the exact quantum mechanical inter electronic repulsion and the second term on the right hand side is a correction for the errors associated with classical treatment of electron repulsion. J.C. Slater later determined that the exchange energy is orders of magnitude greater than the correlation energy. Slater started with the assumption that the exchange hole around any position could be approximated by a sphere of constant potential whos radius is the magnitude of the density at that point[24]. Prior to that and working within the regime of a uniform electron gas, Bloch[25] and Dirac[26] were able to formulate an approximation to the exchange energy as well

$$E_x[\rho(\mathbf{r})] = -\frac{9\alpha}{8} \left(\frac{3}{\pi}\right)^{1/3} \int \rho^{4/3}(\mathbf{r}) d\mathbf{r}. \qquad (16)$$

Both derivations of the exchange energy were essentially identical except that in Slater's case $\alpha = 1$ and in Block/Dirac's case $\alpha = \frac{2}{3}$, and incorporation of this term into the Thomas-Fermi

equations is referred to as Thomas-Fermi-Dirac theory.

Even with Thomas-Fermi-Dirac theory, results were still too inaccurate and still lacked an adequate way of accounting for molecular bonding. Nevertheless, the simplicity of Thomas-Fermi-Dirac theory over wave function based methods made it entirely too enticing to completely abandon despite lacking any formal mathematical foundation especially the establishment of a variational principle (as opposed to an assumed one). It would be several decades later when the next major advance but in 1964 Hohenberg and Kohn[27] published their famous paper in which they proved two theorems solidifying density functional theory as a legitimate (semi-classical) quantum theory with firm mathematical footing.

Thomas-Fermi-Dirac theory established that electrons interact with some external potential, which for a uniform electron gas is some uniformly distributed positive potential and for a molecule is the attraction to the positively charged nuclei. Hohenberg and Kohn's first theorem states:

Theorem 1. *For any system of interacting particles in an external potential $V_{ext}(\boldsymbol{r})$, the potential $V_{ext}(\boldsymbol{r})$ is determined uniquely, except for a constant, by the ground state particle density $\rho_0(\boldsymbol{r})$.*

In order to establish the dependance of the energy on the density it is necessary to consider the ground state electron density. The proof of theorem (1) proceeds via *reductio ad absurdum*. Assume that the non degenerate ground state density, ρ_0, is determined by two different external potentials, v_a and v_b. The two Hamiltonians in which v_a and v_b appear are denoted by H_a and H_b respectively and are associated with a ground-state wave function, Ψ_0 and it's associated eigenvalue, E_0. Referring back to the variational principle, the expectation value of Hamiltonian a over the wave function b must be greater than the ground state energy of a.

$$E_{0,a} < \langle \Psi_{0,b} | H_a | \Psi_{0,b} \rangle \tag{17}$$

Noting that $-H_b + H_b = 0$ we may rewrite the previous expression as

$$E_{0,a} < \langle \Psi_{0,b} | H_a - H_b + H_b | \Psi_{0,b} \rangle$$

$$< \langle \Psi_{0,b} | H_a - H_b | \Psi_{0,b} \rangle + \langle \Psi_{0,b} | H_b | \Psi_{0,b} \rangle \qquad (18)$$

$$< \langle \Psi_{0,b} | v_a - v_b | \Psi_{0,b} \rangle + E_{0,b}$$

Since v_a and v_b are one electron potentials we can write

$$E_{0,a} < \langle \Psi_{0,b} | v_a - v_b | \Psi_{0,b} \rangle + E_{0,b} = \int [v_a - v_b] \rho_0 d\mathbf{r} + E_{0,b} \qquad (19)$$

and since the argument is symmetric in a and b we also have

$$E_{0,b} < \langle \Psi_{0,b} | v_b - v_a | \Psi_{0,b} \rangle + E_{0,a} = \int [v_b - v_a] \rho_0 d\mathbf{r} + E_{0,a} \qquad (20)$$

Adding the inequalities for $E_{0,a}$ and $E_{0,b}$ we arrive at

$$E_{0,a} + E_{0,b} < \int [v_a - v_b] \rho_0 d\mathbf{r} + \int [v_b - v_a] \rho_0 d\mathbf{r} + E_{0,a} + E_{0,b} \qquad (21)$$

We observe that the integrals in the above expression sum to zero since

$$\int [v_a - v_b] \rho_0 d\mathbf{r} + \int [v_b - v_a] \rho_0 d\mathbf{r} = \int [v_a - v_b] \rho_0 d\mathbf{r} - \int [v_a - v_b] \rho_0 d\mathbf{r} = 0 \qquad (22)$$

And so we arrive at the contradiction that

$$E_{0,a} + E_{0,b} < E_{0,a} + E_{0,b} \qquad (23)$$

The following result shows that the original assumption is incorrect which implies that the nondegenerate ground state density uniquely determines the external potential which, then

20

determines the Hamiltonian and the wave function and ultimately the ground state energy.

In the second Hohenberg-Kohn theorem they provide a proof for a variational method.

Theorem 2. *A universal functional for the energy $E[\rho]$ in terms of the density $\rho(\boldsymbol{r})$ can be defined, valid for any external potential $V_{ext}(\boldsymbol{r})$. For any particular $V_{ext}(\boldsymbol{r})$, the exact ground state energy of the system is the global minimum value of this functional, and the density $\rho(\boldsymbol{r})$ that minimizes the functional is the exact ground state density $\rho_0(\boldsymbol{r})$.*

The first Hohenberg-Kohn theorem establishes the existence of some unique external potential determined by the ground state electron density. This in turn determines the Hamiltonian and wave function. With the wave function in hand all ground state observables of the system may also be determined.

$$E_0 = E[\rho_0(\mathbf{r})] = \langle \Psi_0 | H_0 | \Psi_0 \rangle \tag{24}$$

By variational principle

$$E_0 = E[\rho_0(\mathbf{r})] = \langle \Psi_0 | H_0 | \Psi_0 \rangle < \langle \Psi' | H' | \Psi' \rangle = E' \tag{25}$$

The functional for the energy is written in terms of the electron density. And so minimizing with respect to the electron density, i.e. find the global minimum, gives the true ground state density $\rho_0(\mathbf{r})$. And so with the proof of the second theorem Hohenberg and Kohn showed that density functional methods did indeed have a variational principle associated with it. What was still lacking was some characteristic variational equation in which to systematically converge to the ground state density. That problem was addressed a year later in 1965 by Kohn and Sham[28].

Hohenberg and Kohn showed that the density determines the external potential, which determines the Hamiltonian, which determines the wave function and finally the energy

eigenvalues. As it stands, simplicity over Hartree-Fock theory is not so apparent because of the interelectronic term. One of the main insights of Kohn and Sham is that simplification could be achieved by assuming a Hamiltonian operator for a system of non-interacting electrons expressed as a series of one-electron operators. These operators have eigenfunctions that are Slater determinants of individual one-electron eigenfunctions, and eigenvalues that are the sum of all one-electron eigenvalues. The next important insight is to take as your starting point a fictitious system of non-interacting electrons that has for their overall ground-state density a one-to-one correspondence with a ground-state density of some real system in which the electrons do interact. The flow chart below illustrates schematically the results of Kohn and Sham.

$$V_{ext}(\mathbf{r}) \quad \overset{\text{HK}}{\Longleftarrow} \quad \rho_0(\mathbf{r}) \quad \overset{\text{KS}}{\Longleftrightarrow} \quad \rho_0(\mathbf{r}) \quad \overset{\text{HK}_0}{\Longrightarrow} \quad V_{KS}(\mathbf{r})$$

$$\Downarrow \qquad\qquad \Uparrow \qquad\qquad \Uparrow \qquad\qquad \Downarrow$$

$$\Psi_i(\{\mathbf{r}\}) \quad \Longrightarrow \quad \Psi_0(\{\mathbf{r}\}) \qquad \psi_{i=1,\dots,N_e}(\mathbf{r}) \quad \Longleftarrow \quad \psi_i(\mathbf{r})$$
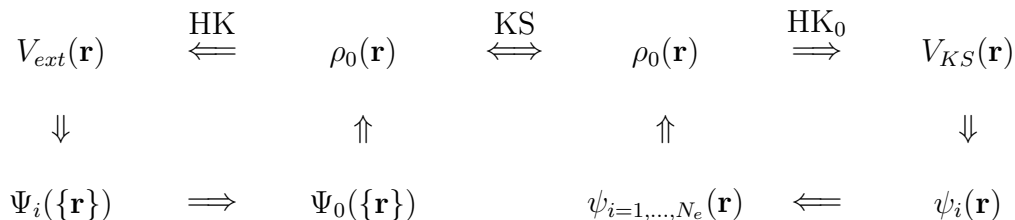
Figure 5: Schematic representation of the results of Kohn and Sham extending the results of Hohenberg and Kohn's density functional theory recreated from Martin[3]. The arrow labeled KS is the Kohn-Sham theorem and HK_0 is the Hohenberg-Kohn theorem applied to the system of non-interacting electrons. $\psi_i(\mathbf{r})$ is the independent particle wave function, which is formed from the non-interacting Kohn-Sham potential $V_{KS}(\mathbf{r})$. Once the non-interacting wave function $\psi_{i=1,\dots,N_e}(\mathbf{r})$ is found the non-interacting density, which is also the interacting density $n_0(\mathbf{r})$ can be calculated. Applying the HK theorems and the interacting potential $V_{ext}(\mathbf{r})$ the ground state density $\Psi_0(\{\mathbf{r}\})$ may be found.

Figure 5 represents the work of Kohn and Sham where the right hand side of the KS arrow is the system of non-interacting electrons and the left hand side is the system of interacting electrons. The prior work of Hohenberg and Kohn (HK) is represented by the labeled arrow where they proved rigorously that a unique ground state density uniquely determines the unique external potential, and thereby all of the ground state properties of the system. This is true for both the interacting and non-interacting system. The work of Kohn and Sham

is represented by the arrow labeled KS whereby they showed that the same density for a system of interacting electrons is the same as the density for some non-interacting system.

Facilitation of their analysis requires that the energy functional be further split

$$E[\rho(\mathbf{r})] = T_{ni}[\rho(\mathbf{r})] + V_{ne}[\rho(\mathbf{r})] + V_{ee}[\rho(\mathbf{r})] + \Delta T[\rho(\mathbf{r})] + \Delta V_{ee}[\rho(\mathbf{r})] \tag{26}$$

where the right hand side contains terms for the kinetic and potential energies of the non-interacting system as well as correction terms for the kinetic energy $(\Delta T[\rho(\mathbf{r})])$ representing the interacting nature of the electrons and nonclassical corrections to the electron repulsion energy $(\Delta V_{ee}[\rho(\mathbf{r})])$.

The kinetic energy for non-interacting electrons is the sum of individual electron kinetic energies. By reintroducing orbitals the expression for the energy in terms of the density may be rewritten

$$
\begin{aligned}
E[\rho(\mathbf{r})] = \sum_{i}^{N} & \left(\langle \chi_i | -\frac{1}{2}\nabla_i^2 | \chi_i \rangle - \langle \chi_i | \sum_{i}^{nuc} \frac{Z_k}{|\mathbf{r}_i - \mathbf{r}_k|} | \chi_i \rangle \right) + \\
& \sum_{i}^{N} \langle \chi_i | \frac{1}{2} \int \frac{\rho(\mathbf{r}')}{|\mathbf{r}_i - \mathbf{r}'|} d\mathbf{r}' | \chi_i \rangle + E_{xc}[\rho(\mathbf{r})]
\end{aligned}
\tag{27}
$$

where the density of a slater determinant wave function is

$$\rho(\mathbf{r}) = \sum_{i=1}^{N} \langle \chi_i | \chi_i \rangle \tag{28}$$

and the exchange-correlation energy is

$$E_{xc}[\rho(\mathbf{r})] = \Delta T[\rho(\mathbf{r})] + \Delta V_{ee}[\rho(\mathbf{r})] \tag{29}$$

Within the exchange and correlation functional is encapsulated effects for quantum mechanical exchange and correlation, correction for classical self-interaction, and differences in

kinetic and potenttial energies between the interacting and non-interacting systems.

Reintroducing orbitals, χ, and varying to minimize E gives the pseudoeigenvalue equation

$$h_i^{KS}\chi_i = \varepsilon_i\chi_i \tag{30}$$

where h_i^{KS} is the Khon-Sham one-electron Hamiltonian defined as

$$h_i = -\frac{1}{2}\nabla_i^2 - \sum_i^{nun} \frac{Z_k}{|\mathbf{r}_i - \mathbf{r}_k|} + \int \frac{\rho(\mathbf{r}')}{|\mathbf{r}_i - \mathbf{r}'|}d\mathbf{r}' + V_{xc}. \tag{31}$$

In the Kohn-Sham one-electron Hamiltonian the term for the exchange-correlation potential, V_{XC}, is the functional derivative of the exchange-correlation energy with respect to the density

$$V_{xc} = \frac{\delta E_{xc}}{\delta\rho}. \tag{32}$$

The functional derivative is part of variational calculus that generalizes the concept of the derivative for use in function spaces. Having defined the approach of Kohn and Sham determination of the orbitals are expressed within a basis set of functions, ϕ, where individual orbital coefficients are found by solution of a secular equation

$$K_{\mu\nu} = \left\langle \phi_\mu \left| -\frac{1}{2}\nabla^2 \sum_k^{nuclei} \frac{Z_k}{|\mathbf{r} - \mathbf{r}_k|} + \int \frac{\rho(\mathbf{r}')}{|\mathbf{r} - \mathbf{r}'|}d\mathbf{r}' + V_{XC} \right| \phi_\nu \right\rangle. \tag{33}$$

It is important to note that the density is required in order to compute the matrix elements of the secular equation, but the density itself is determined by using the orbitals found by solution of the secular equation. This implies that the process of Kohn and Sham must be carried out in an iterative self-consistent process. The numerical process for solving these equations is illustrated in the following flow chart.

Choose basis set(s)

Choose a molecular geometry $\mathbf{q}^{(0)}$

Compute and store all overlap and one-electron integrals

Guess initial density matrix $\mathbf{P}^{(0)}$

Construct and solve Kohn-Sham secular equation

Replace $\mathbf{P}^{(n)}$ with $\mathbf{P}^{(n-1)}$

Construct density matrix from occupied KS MOs

Choose new geometry according to optimization algorithm

no

Is new density matrix $\mathbf{P}^{(n)}$ sufficiently similar to old density matrix $\mathbf{P}^{(n-1)}$

yes

Optimized molecular geometry?

no

no

Does the current geometry satisfy the optimization criteria?

yes

yes

Output data for optimized geometry

Output data for unoptimized geometry

Figure 6: Flow chart recreated from Cramer[4] of the numerical process in solving the Kohn-Sham system.

The flow chart illustrates the process that the equations are solved in to determine the

optimized ground state geometry. When the difference in the old density and the new density reach a certain threshold value the system has attained self-consistency and the calculations will terminate and output the optimized geometry. The outputted geometry is then able to be used to determine all of the ground state properties of the system including excitation energies found from a time-dependent DFT calculation.

2.4 Time-Dependent Density Functional Theory

The work of Hohenberg and Kohn established density functional theory as a legitimate rigorously founded ground-state quantum theory. By extension of it being a ground state theory is able to resolve all the properties of the ground state, including in theory electron excitations. Kohn and Sham provided the tools to solve these systems in a self consistent way. What was still needed was a formal way to investigate the dynamics a system under some time-varying potential. It was Runge and Gross[29] in 1985 who much in the same way Hohenberg and Kohn gave foundation to DFT they gave a formal mathematical foundation for a time-dependent density functional theory (TD-DFT). Their approach begins with a system in the presence of some time-dependent potential with Hamiltonian

$$H(t) = T + V_{ext}(t) + V_{ee} \tag{34}$$

and evolves according to the time-dependent Shrödinger equation

$$i\frac{\partial}{\partial t}\Psi(t) = H(t)\Psi(t) \tag{35}$$

with initial condition

$$\Psi(0) = \Psi \tag{36}$$

By assuming that the external potential may be represented in a Taylor expansion and employing continuity equations, they were able to prove the following result:

Theorem 3. *In a many-body system evolving from some initial state, $\Psi(\vec{r}, t)$, there exists a one-to-one correspondence between some external time-dependent potential, $v_{ext}(\vec{r}, t)$, and the electronic density, $\rho(\vec{r}, t)$.*

The Runge-Gross theorem tells us that as some system evolves in time the time-dependent density uniquely determines the time-dependent potential. Their result can be extended into a Kohn-Sham formalism in which there exists a non-interacting time-dependent system with the same time-dependent density. The task is to be able to determine the correct potential which determines the Hamiltonian

$$H = T + V_{KS} \tag{37}$$

which determines the wave function. Under an orbital representation the time-dependent Kohn-Sham equation is written as

$$\left(-\frac{1}{2}\nabla^2 + V_{KS} \right) \phi_i(\mathbf{r}, t) = i\frac{\partial}{\partial t}\phi_i(\mathbf{r}, t) \tag{38}$$

with initial conditions

$$\phi_i(\mathbf{r}, 0) = \phi_i(\mathbf{r}). \tag{39}$$

From which can be generated the time-dependent density of a non-interacting system

$$\rho_0(\mathbf{r}, t) = \sum_i^N |\phi_i(\mathbf{r}, t)|^2. \tag{40}$$

This density is the same density of the interacting system. What remains is determining the form of the potential for the non-interacting system either exactly or approximately. The

27

Kohn-Sham potential decomposed into kinetic, Coulombic, and exchange-correlation terms is

$$V_{KS}(\mathbf{r}, t) = V_{ext}(\mathbf{r}, t) + V_J(\mathbf{r}, t) + V_{XC}(\mathbf{r}, t). \tag{41}$$

Runge and Gross developed their proof starting with the quantum mechanical action. The action of a system A describes the evolution of that system over some time period. It takes as its argument a function called the Lagrangian $L(x, \dot{x}, t)$, which summarizes the dynamics of the entire system. The action is an integral of the Lagrangian over some time period. The principle of stationary action states that the true path of a system is the one for which the action is stationary (or minimized) over small variations of the action $\delta A = 0$. Runge and Gross use the quantum mechanical action

$$A = \int_{t_0}^{t_1} dt \left\langle \psi(t) \left| i\frac{d}{dt} - H(t) \right| \psi(t) \right\rangle \tag{42}$$

The quantum mechanical action calculates the probability amplitudes for all possible outcomes of a system where the most probable path has the greatest probability amplitude. The minimization constraint of the action in the Runge-Gross formulation is with respect to the time-dependent density.

$$\frac{\delta A}{\delta \rho(\mathbf{r}, t)} = 0 \tag{43}$$

Returning to the idea of Kohn and Sham of a non-interacting system of independent particles leads to a time-dependent Schrödinger like equation

$$i\hbar \frac{d\psi_i(t)}{dt} = H(t)\psi_i(t) \tag{44}$$

with an effective Hamiltonian

$$H_{eff}(t) = -\frac{1}{2}\nabla^2 + V_{ext}(\mathbf{r}, t) + \int d\mathbf{r} \frac{\rho(\mathbf{r}, t)}{|\mathbf{r} - \mathbf{r}'|} + V_{xc}[\rho](\mathbf{r}, t) \tag{45}$$

28

The most common way in which excitation energies are found from TD-DFT is via a perturbative approximation by linear response and Green's function type methods. These methods can be imagined as a system evolving in time and then is 'hit' by some external field. The system evolves using the ground state density until such time the time dependent perturbation is 'switched on' by some linear response function. Considering an external potential v_{ext} that at some time t_0 a time-dependent perturbation is 'switched on'

$$v_{ext} = v_0 + \delta v. \tag{46}$$

And since the Hohenberg-Kohn theorem establishes a one-to-one correspondence between the external potential and the density, another perturbation series can be given in terms of the density

$$\rho(\mathbf{r}, t) = \rho^{(0)}(\mathbf{r}) + \delta\rho(\mathbf{r}, t) + \cdots \tag{47}$$

where the zeroth order term is the ground state density and the first order term is the time dependent perturbation. By taking the Fourier transform of $\delta\rho(\mathbf{r}, t)$ the density is represented then in terms of the frequency $\delta\rho(\mathbf{r}, \omega)$ and can be written as

$$\delta\rho(\mathbf{r}, \omega) = \int d^3\mathbf{r}' \chi(\mathbf{r}, \mathbf{r}', \omega) \delta v_{ext}(\mathbf{r}', \omega) \tag{48}$$

The key to linear response theory for TD-DFT is the form of the response function $\chi(\mathbf{r}, \mathbf{r}', \omega)$ for the system of interacting electrons. Construction of the interacting response function is complicated, but the Kohn-Sham theorem makes it possible to form the response function for the non-interacting $\chi_{KS}(\mathbf{r}, \mathbf{r}', \omega)$, which have poles at the excitation frequencies and relate that back to the system of interacting electrons. Please refer to the book by Carsten Ullrich[30] for a more in depth discussion of linear response TD-DFT.

2.5 Effective Core Potentials (Pseudopotentials)

As one moves down the periodic table to heavier and heavier elements the number of electrons associated with each atom also increases to balance the increase in positive nuclear charge. For each electron added there is the added burden of needing to do more and more calculations in order to converge to the proper ground state density. Heavier atoms consist mostly of core electrons greatly outnumbering valence electrons. Added to that is that the core electrons have fundamentaly no role in chemical reactions. This problem was addressed by Hellmann in 1935, where his solution consisted of replacing the core electrons with analytic functions that would reasonably approximate the combined nucleus-electron core. Since the core is replaced by some effective potential they became known as effective core potentials. And so only the valence electrons need be treated within a basis set approximation with the rest of the electrons being treated by the ECPs taking into account all the necessary requirements of electron interactions such as correlation, the Pauli principle, and even relativistic effects.

For the heavy elements it is essential to include relativistic effects. Electrons are not massless particles, and the level to which relativity affects the energy of the electron depends on its velocity. For an electron orbiting a nucleus the larger the nucleus implies the greater velocity of the electron.

Another important question that can be posed is how many electrons to include in the ECP. Should it be all the core electrons or should core electrons be left out of the ECP? ECPs can be of two varieties, large and small core. In large core ECPs all of the electrons except for the valence electrons are included in the ECP. For small core ECPs, all electrons except for the valence electrons and the next lower shell electrons are included in the ECP. This project utilizes the Stuttgart-Dresden large core relativistic ECPs developed by Dolg et al. Not only do these ECPs incorporate relativistic effects but they are also so called 'in-core'

ECPs meaning that the $4f$ valence electrons are included in the ECP. This is appropriate for the lanthanides as a result of the $5s$ and $5p$ orbitals having a larger radial distribution than the $4f$ orbitals.

2.6 Basis Sets

In *ab initio* calculations the exact form of the wave function used is not known. To address this particular issue the most common technique is to represent the wave function as a series expansion of basis functions. The choice of functions used can be anything from exponentials, Gaussians, polynomials, or even plane waves. The choice decided on the functions must also represent to the physical characteristics of the electrons being modeled. For example it would be improper to uses functions who's energy increases quadratically for an electron infinitely far away from the nucleus because we know that at some point equal to the ionization energy the electron will no longer be attached to the atom.

Two of the most common types of basis sets used in electronic structure theory are the Slater type orbitals and Gaussian type orbitals. Slater type orbitals have a general functional form of

$$\chi_{\zeta,n,l,m}(r,\theta,\varphi) = NY_{l,m}(\theta,\varphi)r^{n-1}e^{-\zeta r}. \tag{49}$$

Where N is a normalization constant and $Y_{l,m}(\theta,\varphi)$ represents spherical harmonic functions and $r^{n-1}e^{-\zeta r}$ represent the radial expansion of the function. Gaussian type orbitals on the other hand have the general functional form of

$$\chi_{\zeta,n,l,m}(r,\theta,\varphi) = NY_{l,m}(\theta,\varphi)r^{2n-2-l}e^{-\zeta r^2} \tag{50}$$

where N is a normalization constant, $Y_{l,m}(\theta,\varphi)$ are the spherical harmonics, and $r^{2n-2-l}e^{-\zeta r^2}$ are the radial expansion terms. The radial expansion terms dictate the behavior of the electron as a function of distance from the nucleus. The difference between Slater type

orbitals and Gaussian type orbitals may appear to be slight but has significant implications. In general Slater, type orbitals give a better representation of the behavior of the electron near the nucleus than do Gaussian type orbitals but Gaussian type orbitals are computationally more efficient and so in many cases are used more frequently than Slater type orbitals.

It was stated that a basis set is a series expansion used to represent a wave function and for an infinitely large basis set the representation is exact. This is theoretically unfeasible since there is no way of summing an infinite number of functions. This approximation now has the question of how many functions do you use to fully describe the system? A minimum basis set consists of just enough functions to contain all of the electrons. For example a hydrogen and helium atom means a single *s*-function. The second row would require two *s*-functions and a set of *p*-functions. And the trend continues for the remaining rows.

And so having described the minimum case the next improvement is a doubling or tripling of the number of functions used. These are referred to as *Double* and *Triple Zeta* type basis sets respectively. There are also Quadruple and higher zeta type basis sets. It is common to have molecular bonding where there is not an even distribution of charge. In these cases basis sets can include functions of higher angular momentum to accommodate this type of behavior. Diffuse functions are 'shallow' gaussian functions that augment the tail portion of the basis set. These functions are useful when considering systems with anions or with 'softer' atoms whos electrons are more loosely bound.

Another aspect of calculations with basis sets is the concept of the basis set contraction. Each function used in the basis has associated with it expansion coefficients which are energy optimized through a variational procedure. This procedure optimizes the core electrons more efficiently over the valence electrons since the core electrons are more energetically important where as the valence electrons are more important chemically. By making the coefficients for the inner basis functions constant so that they need to be determined by a variational method, it is then possible, for example, to represent the 1s-orbital as a fixed linear combination of six

basis functions. To combine the set of *primitive* type orbitals into a smaller set of *contracted* functions by fixing the coefficient and forming linear combinations is known as basis set contraction.

The basis set used in the experiments conducted in this thesis are the Pople style split valence basis sets of John Pople, who was also instrumental in the development of the Gaussian software package which was used in this study. A split valence basis set splits the number of primitive gaussian type orbitals (GTO) used for the core and valence electrons and has the form k-$nlmG$. The k indicates the number of primitive GTOs that are used to represent the core orbitals. The nlm terms indicate the number of functions the valence orbitals are split into and how many primitive GTOs are used to represent them. The two nl values represent a split valence were as nlm represent a triple split valence. In this project the basis set choice is 6-31+G**. Following the naming convention of Pople type basis sets, 6-31+G** is a split valence basis set with a contraction of six primitive GTOs, the inner part of the valence orbitals are a contraction of three primitive GTOs, and the outer part is represented by one primitive GTO. The addition of '+' represents the inclusion of diffuse functions and the ** represents the inclusion of polarization functions.

CHAPTER 3:   EXPERIMENTAL

3.1   Computational Methods

All calculations were done using the Gaussian 09[31] computational chemistry software on the Stampede supercomputer at the Texas Advanced Computing Center (TACC) at the University of Texas at Austin in Austin, Texas with a grant through the Extreme Science and Engineering Discovery Environment (XSEDE).

Geometry Optimization

All geometry optimizations were done in the gas phase without constraints on the symmetry, bond distances, or bond angles. The 6-31+G**[32–41] basis set was used for all atoms except bromine which used the 6-311+G** basis set and europium which utilized the Stuttgart-Dresden large core (53 electrons in the core and 10 electrons in the valence shell) effective core potential (ECP) and basis set developed by Dolg, et al. The B3LYP[42] hybrid exchange correlation functional was used for all ground state geometry optimizations. Gaussview was used to construct the initial structures using XYZ cartesian coordinates from an experimentally determined single crystal X-ray structure. The Mercury software package was used to extract the structural information using .cif file. Optimized geometry parameters and molecular orbital energies were extracted from the gaussian .log files using Chemcraft software package. Orbital energies were plotted using a MATLAB program written by the author and provided in the supporting information.

Excited State Calculations

Singlet state and triplet state calculations were done using time-dependent density functional theory (TD-DFT) as implemented by Gaussian 09. All excited state calculations were done in the gas phase without symmetry constraints using the same basis sets and exchange correlation functional that was employed for the ground state geometry optimisation. Ver-

tical excitation energies and oscillator strengths of the singlet states were calculated using time-dependent density functional theory (TD-DFT) to compare with the experimental UV-visible absorption data. The TD-DFT method was also employed to determine the lowest lying triplet state energy and orbital characteristics. Excited states and oscillator strengths were extracted using Chemcraft software package. Chemcraft was also used to generate TD-DFT plots of excited state orbitals. Excited states were plotted using a MATLAB program written by the author and provided in the supporting information.

3.2 Synthetic Methods

$EuCl_3 \cdot 6H_2O$, thenoyltrifluoroacetone, dichloromethane, acetone, and tetrahydrofuran were purchased from Fischer Scientific and used without any further purification. 18 Ω nano pure water was used for all synthetic procedures. All of the DPPZ substituted ligands were synthesized by Dr. Brian Dinkelmyer's research group at Western Carolina University.

Synthesis of $Eu(TTA)_3(H_2O)_2$

The synthesis of $Eu(TTA)_3(H_2O)_2$ complex requires a 3:1 molar ratio of TTA to $EuCl_3 \cdot 6H_2O$. A solution of TTA was made by dissolving NaOH (3 mmol, 0.12 g) in nano pure water (20 mL) to which TTA (3 mmol, 0.67 g) was added and stirred until dissolved. In a separate container, $EuCl_3 \cdot 6H_2O$ (1 mmol, 0.37 g) was dissolved in nano pure water (10 mL). The two solutions were combined and stirred under an inert argon atmosphere at 60 ^{o}C for 30 minutes. At the end of the thirty minute heating period, the solution was stirred at room temperature for 2.5 to 3 hours. The white precipitate was collected via vacuum filtration and washed with nano pure water (500 mL) and hexane (50 mL).

Synthesis of $Eu(TTA)_3DPPz$-R

The synthesis of $Eu(TTA)_3DPPz$-R requires a one to one molar ratio of $Eu(TTA)_3(H_2O)_2$ complex to substituted DPPZ ligand. $Eu(TTA)_3(H_2O)_2$ (0.1 mmol, 0.085g) was dissolved in HPLC grade acetone (10mL). DPPZ (0.1mmol, -H = 0.028g, -NO_2 = 0.033g, -$C_3H_5O_2$ =

0.035g, -$C_2H_3O_2$ = 0.034g, -Br = 0.036g) ligand was dissolved in HPLC grade dichloromethane (15mL). Once both complex and ligand were dissolved, the two solutions were combined in a round bottom flask which was then capped, with a vent, and allowed to react for 12 to 24 hours while being stirred. At the conclusion of the stirring period,the reaction mixture was allowed to slowly evaporate for possible formation of crystals.

3.3   Instrumental Characterization

UV-Vis and Fluorescence Spectroscopy

UV-visible absorption spectroscopy was performed using an Agilent 8453 UV-Vis spectrophotometer equipped with a deuterium discharge lamp as the ultra-violet source and a tungsten-halogen filament lamp as the visible source. The detector was a photodiode array operating in absorbance mode. Fluorescent spectroscopy was done on a Perkin-Elmer LS-55 fluorescence spectrophotometer using a xenon arc lamp source and a photomultiplier tube detector operating in emission mode with 5 nm slit width and excitation wavelength of 340 nm.

Luminescent Quantum Yield Measurements

Luminescent quantum yield measurements were carried out to evaluate the efficiency of ligand sensitization. A detailed description of overall quantum yield, intrinsic quantum yield, ligand sensitization, and the processes associated with each is given in chapter one. This project used a reference of Eu(TTA)$_3$Phen in tetrahydrofuran (with a reported luminescent quantum yield of 0.36[43]) to find the overall luminescent quantum yields of the synthesized complexes. The overall quantum yield was calculated by reference method using the following equation[44]:

$$\Phi_S = \Phi_R \frac{I_S}{I_R} \frac{A_R}{A_S} \frac{\eta_S^2}{\eta_R^2}. \tag{51}$$

Where I is the integrated area of Eu(III) emission, A is the absorbance value at the excitation

wavelength, η is the refractive index of the solvent, and Φ is the overall luminescent quantum yield. The subscripts R and S denote reference and sample, respectively.

Overall photoluminescent quantum yields were determined for complexes that have been previously synthesized (Ethyl Ester, Methyl Ester, Bromine, Nitro, and unsubstituted). Absorbance and fluorescence measurements were taken over a period of three days. For each day five absorbance and five fluorescence measurements were taken for each complex. Thus, giving a total number of 15 data points over those three days. Absorbance values at 340 nm and the integrated europium emission were recorded. Luminescent quantum yields were calculated for each day individually with the final reported quantum yield being the mean of the three.

CHAPTER 4: RESULTS AND DISCUSSION

The substituents of the neutral donor DPPZ ligand can have a significant effect on the energy transfer process with respect to the electron withdrawing or electron donating strength of the substituent. The substituents can be group in three ways. The first group are electron donating substituents where NH_2 is the strongest and methyl is the weakest. Hydrogen is in the middle and serves as the reference or zero for which all other substituents are compared to. The third group is electron withdrawing where bromine is the weakest and NO_2 is the strongest.

$$\underbrace{NH_2, MeO, CH_3,}_{\longleftarrow Donating} \underbrace{H,}_{0} \underbrace{Br, COOH, ME, EE, NO_2}_{Withdrawing \longrightarrow}$$
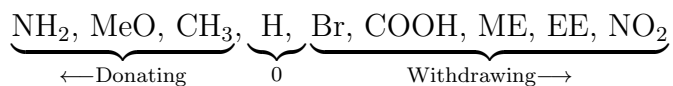
Figure 7: Qualitative scale of substituents ordered from most donating (NH_2) to most withdrawing (NO_2) with hydrogen in the middle serving as the reference point. The carboxylic acid, methyl ester, and ethyl ester all have very similar electron withdrawing capabilities with carboxylic acid being slightly strong due to its acidity.

Does a trend exist between the strength and character of the substituent that will allow us to make informed decisions on how well a substituent will affect the luminescent properties of these luminescent europium complexes? This question has been explored in the study by Nolasco[10] the authors use phenanthroline as the neutral donor ligand, which has been shown to have good quantum yields[45]. In this study we use the dipyridophenazine ligand, which is a more conjugated system with respect to phenanthroline. In Li[16] the authors found that a more conjugated system lowered both the S_1 and T_1 energies, thus making the system less effective at energy transfer. The following sections details the results of our study, and attempts to answer the question of if these substituents are capable of increasing the energy transfer efficiency.

4.1 Ground State Geometry

Density functional theory (DFT) is a ground state theory. Hence, we can use DFT to determine the excited state properties since all of the properties of a system can be be uniquely determined by the ground state configuration. As a means to validate theoretical calculations comparison of the optimized ground state geometry can be compared to experimental geometric parameters. Figure 8 is the DFT-optimized structure of Eu(TTA)₃DPPZ with atom labels for the oxygen and nitrogen that are bonded to europium.
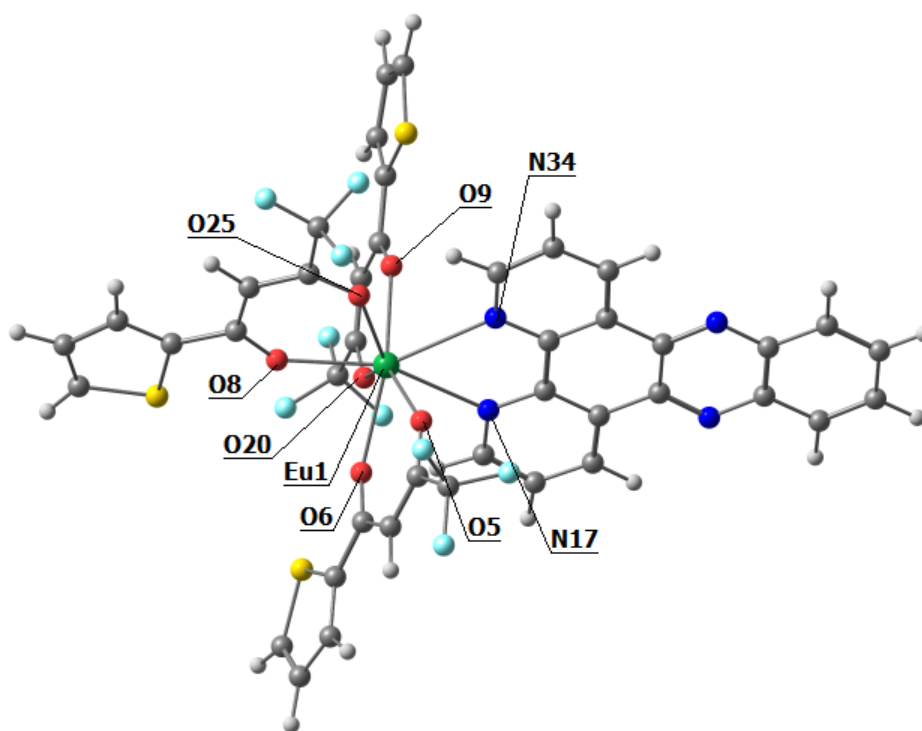
Figure 8: DFT-optimized structure of Eu(TTA)₃DPPZ with labels for the oxygens of the anion TTA that are bonded to europium and the nitrogens of the pheasanthroline part of the DPPZ ligand that are coordinated to europium.

Table 3 contains the calculated optimized bond length data for Eu_NH2, Eu_Br, Eu_COOH, Eu_H, Eu_EE, Eu_ME, Eu_MeO, Eu_CH3, and Eu_NO2. X-ray crystal structural data for Eu_EE is included in parenthesis.

Table 3: DFT-calculated bond length data (Å) for all Eu(TTA)$_3$DPPZ-R complexes.

Atom 1	Atom 2	Eu_NH2	Eu_MeO	Eu_CH3	Eu_H	EU_Br
Eu1	O5	2.417	2.417	2.417	2.416	2.416
Eu1	O6	2.414	2.414	2.413	2.412	2.412
Eu1	O8	2.391	2.390	2.390	2.389	2.388
Eu1	O9	2.423	2.423	2.422	2.422	2.422
Eu1	N17	2.672	2.675	2.676	2.677	2.679
Eu1	O20	2.423	2.422	2.421	2.421	2.420
Eu1	O25	2.414	2.413	2.413	2.412	2.411
Eu1	N34	2.680	2.681	2.682	2.684	2.685
		Eu_COOH	Eu_ME	Eu_EE (exp)	Eu_NO2	
Eu1	O5	2.416	2.416	2.416 (2.365)	2.415	
Eu1	O6	2.411	2.412	2.412 (2.355)	2.410	
Eu1	O8	2.387	2.388	2.388 (2.365)	2.385	
Eu1	O9	2.421	2.422	2.422 (2.361)	2.421	
Eu1	N17	2.680	2.679	2.679 (2.595)	2.685	
Eu1	O20	2.420	2.420	2.420 (2.353)	2.418	
Eu1	O25	2.410	2.411	2.411 (2.370)	2.407	
Eu1	N34	2.688	2.687	2.685 (2.637)	2.691	

DFT optimized structures show octa-coordination to europium with six europium-oxygen bonds (two from each TTA ligand) and two europium-nitrogen bonds from the DPPZ ligand with C1 symmetry. The average Eu-O bond length was found to be 2.412 Å, and the average Eu-N bond length was found to be 2.681 Å. The average Eu-O and Eu-N bond lengths from the X-ray crystal structure of Eu_EE are 2.362 Å and 2.616 Å respectively. Comparison of calculated and experimentally determined average Eu-O bond lengths show a difference of 0.050 Å. The difference between calculated and experimental Eu-N bond lengths are 0.065 Å. These results indicate good agreement between the DFT optimized geometry and the experimentally determined X-ray crystal structure.

In Li *et al.*[16] the authors used density functional theory (computational parameters are mentioned in the introduction chapter) to investigate how the neutral donor ligand's energy transfer process is affected by the secondary ligand size. In that study they calculated the

ground state and excited state properties for Eu_H and Eu_CH3. The average Eu-O bond lengths in Li was found to be 2.405 and the average Eu-N bond lengths were found to be 2.682. When comparing the Eu-O and Eu-N bond lengths in this study of 2.412 Å and 2.681 Å to the results of Li, we find there is a difference of 0.007 Å and 0.001 Å for Eu-O and Eu-N bond lengths respectively. In Nolasco[10] the average Eu-O and Eu-N bond length reported was 2.406 Å and 2.631 Å respectively for a series of substituted phenanthroline complexes. Furthermore, the paper by De Silva *et al.*[46] looks at the luminescence of Tb(III) complexes. In their study terbium's coordination sphere consisted of six oxygen atoms from three negatively charged 2,4-pentanedione (acac) ligands and two nitrogen from the neutral N-donor 2.2′-bipyridine (bipy) that has substituent modifications at the p, p' position. The average experimental and calculated bond length between Tb(III) and oxygen was reported to be 2.345 Å and 2.366 Å respectively. The average experimental and calculated bond length between Tb(III) and nitrogen was reported to be 2.566 Å and 2.681 Å respectively. Noting that the difference in ionic radius between Tb(III) and Eu(III) is only 0.024 Å the similarity between De Silva and this study is significant. The agreement between the results from Table 3, Li, Nolasco, and De Silva suggest that the $4f$ orbitals have little involvement in the bonding of the ligands, which validates the use of large core ECPs in which the valence electrons are included in the ECP.
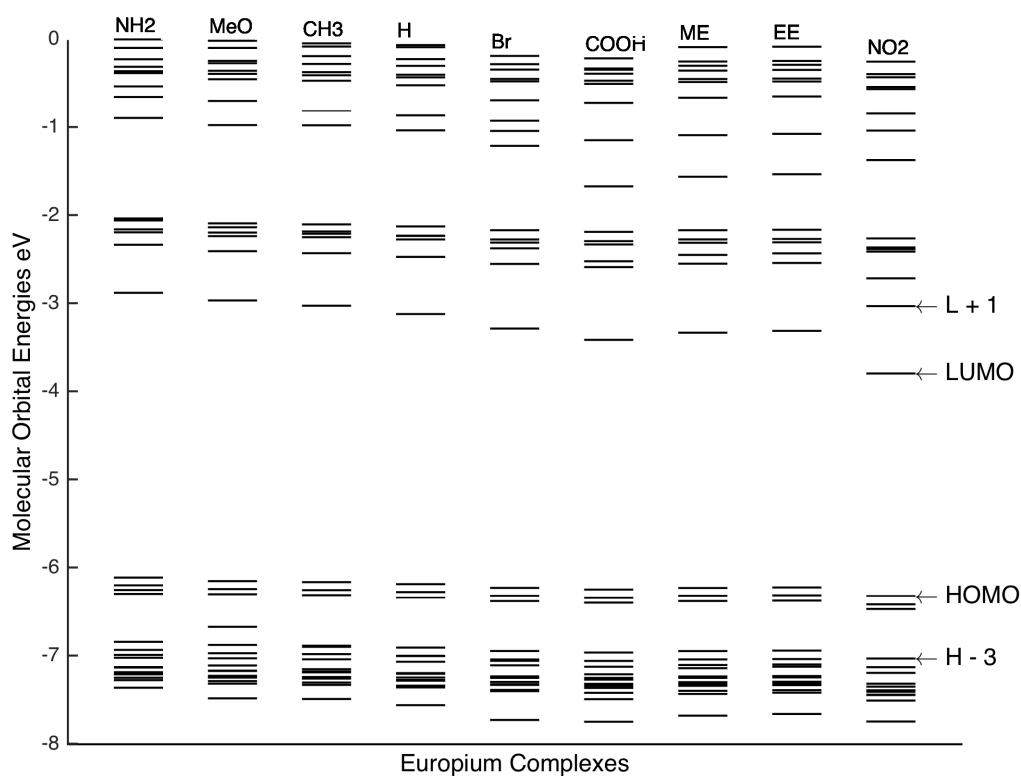
Figure 9: The HOMO-15 to LUMO+15 molecular orbitals of the europium complexes with different substituents

Looking at the distribution of molecular orbital energies in Figure 9, there are some immediate features that can be seen. The first such feature is the way in which the HOMO orbitals are only slightly affected by the substitutions. Second, is the significant gap in energy between the H-3 and H-4 orbitals. The LUMO orbitals show being significantly affected by the ligand substituents, but the L+1 orbitals remain only marginally affected except for Eu_NO2. Given the fact that the only difference between each complex is the substituent on the DPPZ ligand this would suggest that the LUMO orbital is located primarily on the DPPZ ligand and the HOMO and L+1 orbitals are located on the TTA ligands.

Table 4: HOMO-LUMO energy gap for all Eu complexes.

Substitution	HOMO (eV)	LUMO (eV)	ΔE (eV)
Eu_NH2	-6.115	-2.882	3.233
Eu_MeO	-6.155	-2.969	3.186
Eu_CH3	-6.167	-3.029	3.138
Eu_H	-6.190	-3.123	3.067
Eu_Br	-6.232	-3.288	2.944
Eu_COOH	-6.252	-3.416	2.836
Eu_ME	-6.233	-3.335	2.898
Eu_EE	-6.227	-3.313	2.913
Eu_NO2	-6.326	-3.798	2.528

Amines are strong aromatic electron donating groups as a result of resonance stabilized distribution of the lone pair of electrons on the nitrogen. This compared to only a hydrogen on the unsubstituted DPPZ ligand results in an increase in energy of the LUMO orbital relative to DPPZ's LUMO orbital.

Halogens are weak aromatic withdrawing groups as a result of inductive effects. Relative to the hydrogen of the DPPZ ligand, the LUMO energy of the bromine substitution is lower than the LUMO energy of the unsubstituted ligand.

Carboxylic acid, methyl ester, and ethyl ester were speculated to have relatively identical effects as aromatic electron withdrawing groups. In comparison to the hydrogen of the DPPZ, ligand resonance stabilization of positive charge lowers the energy of the LUMO orbitals. Hence, the LUMO energy of the carboxylic acid, methyl ester, and ethyl ester substituted complexes is lower relative to the unsubstituted complex.

Ether groups act as aromatic electron donating groups resulting from resonance stabilization of oxygen lone pairs. The effect that the methoxy group has on the electronic properties of the substituted DPPZ ligand is an overall lowering of the LUMO energy relative to the unsubstituted DPPZ ligand.

Nitro groups act as strong aromatic electron withdrawing groups resulting from resonance

stabilized positive charge. The effect that nitro groups have on the substituted DPPZ ligand is a drastic decrease in the energy of the LUMO orbital relative to the LUMO orbital energy of the unsubstituted DPPZ ligand.

Methyl groups inductively donate electron density to aromatic systems. For the methyl substituted DPPZ ligand there is very slight increase in the LUMO orbital energy relative to the LUMO orbital energy of the unsubstituted DPPZ ligand.

The trend shows that for electron donating groups (amine, methoxy, methyl) there is an increase in the LUMO orbital energy relative to unsubstituted DPPZ ligands. For electron withdrawing groups (bromo, ethyl ester, methyl ester, carboxylic acid, and nitro groups) there is a decrease in the LUMO orbital energy relative to unsubstituted DPPZ ligand. These trends are illustrated in Figure 9 with the calculated HOMO-LUMO energies and gaps presented in Table 4. In addition to the effect on the energy of the LUMO orbitals there is a trend associated with the HOMO to LUMO energy gap. For the aromatic electron donating substituents there is a calculated increase in the energy gap between the HOMO and LUMO orbitals relative to the unsubstituted HOMO-LUMO energy gap. For groups that are aromatic electron withdrawing groups there is an apparent decrease in the energy gap between the HOMO and LUMO orbitals relative to the energy gap between the unsubstituted complex.

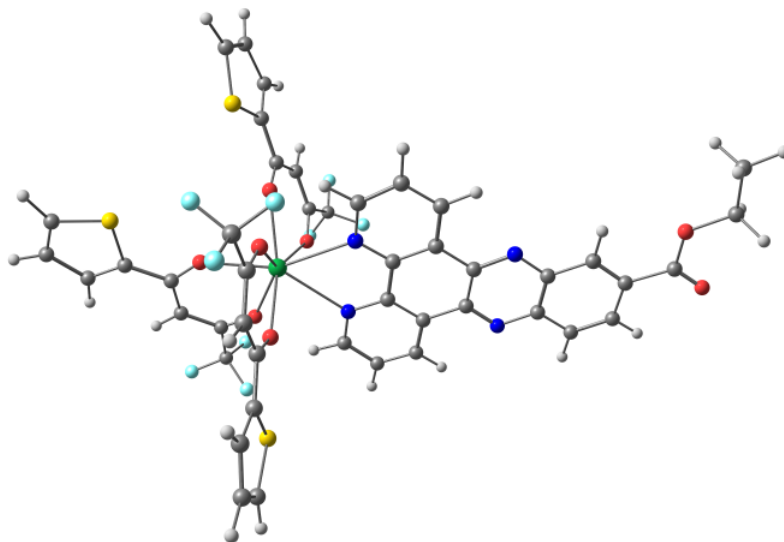## DFT Optimized Ground State Geometries
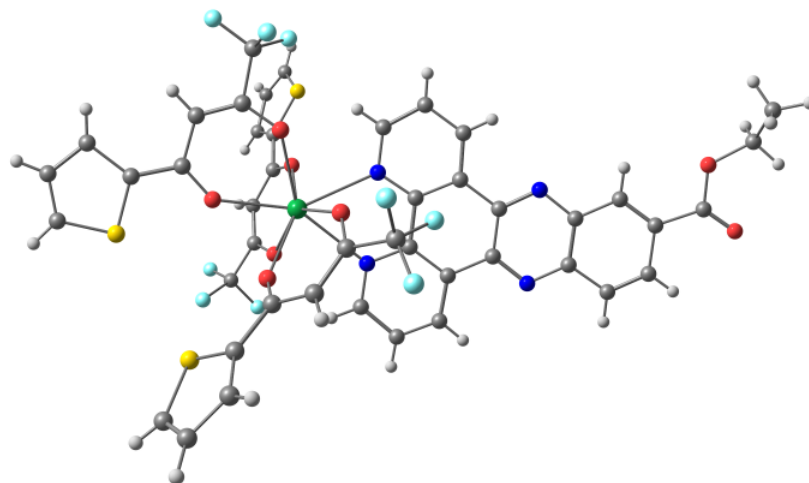

Figure 10: DFT optimized geometry of Eu_EE

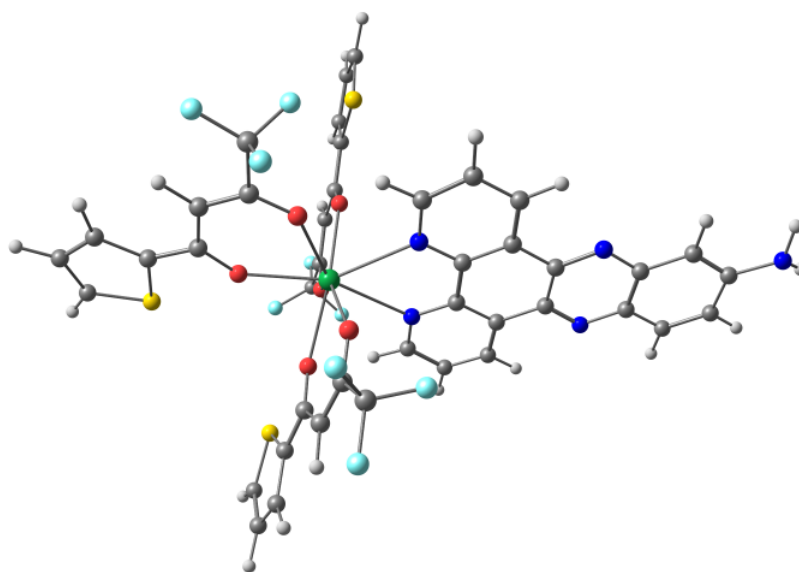Figure 11: X-ray crystal structure of Eu_EE
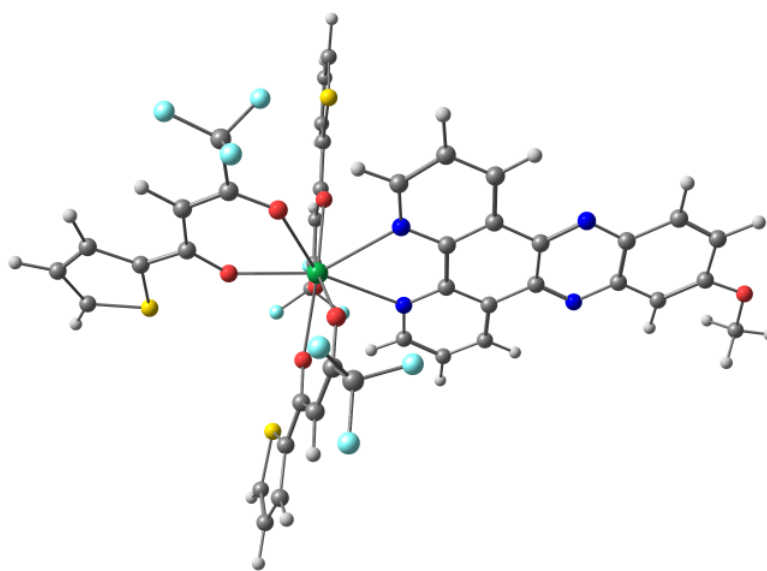
Figure 12: DFT optimized geometry of Eu_NH2

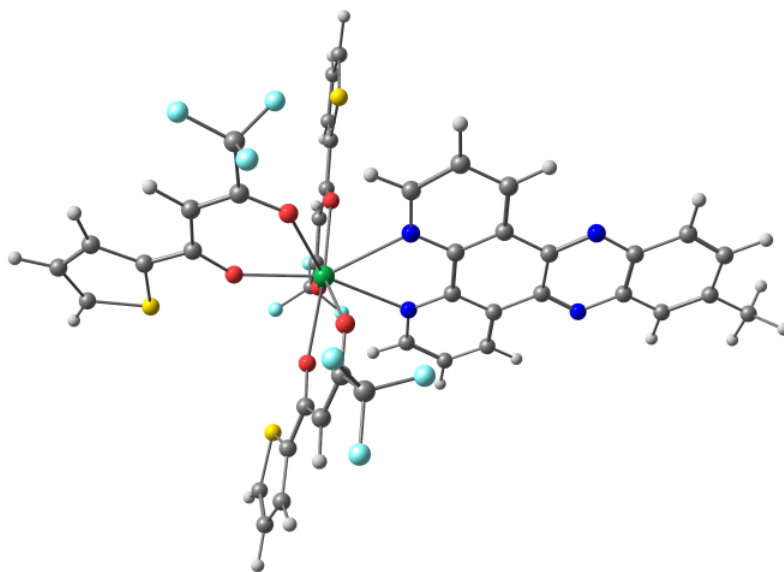Figure 13: DFT optimized geometry of Eu_MeO
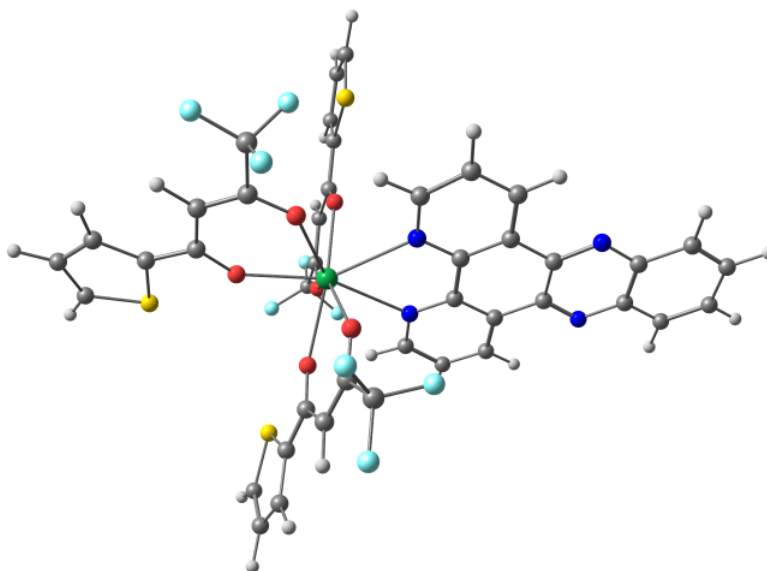
Figure 14: DFT optimized geometry of Eu_CH3

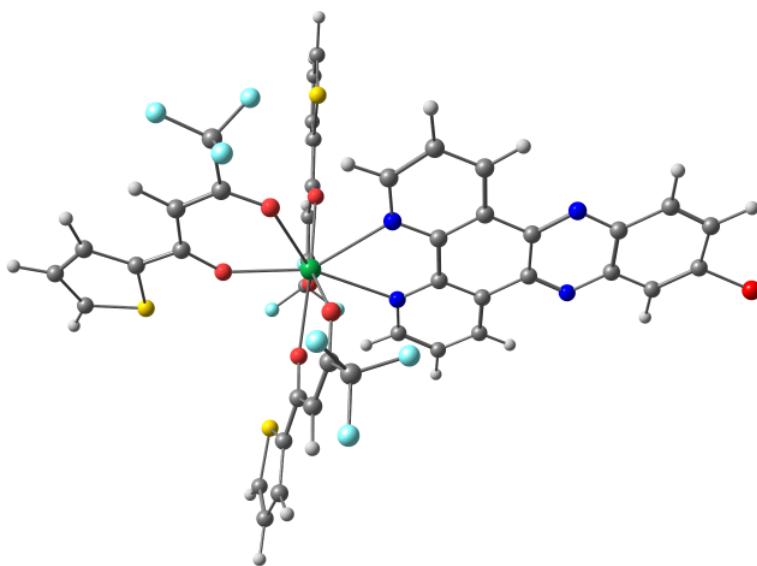Figure 15: DFT optimized geometry of Eu_H
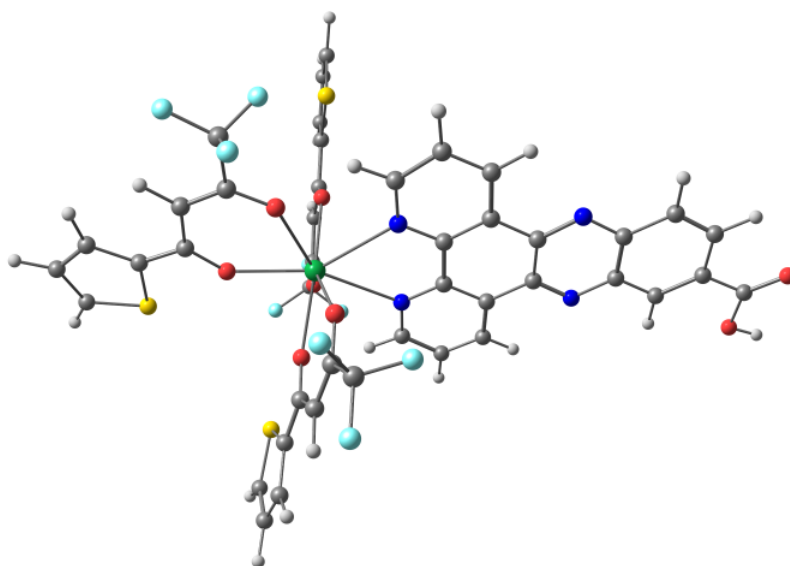
Figure 16: DFT optimized geometry of Eu_Br

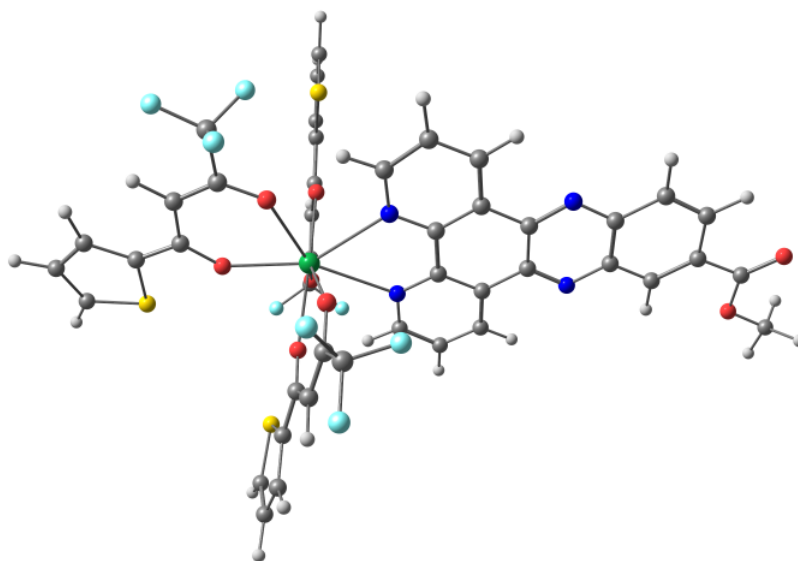Figure 17: DFT optimized geometry of Eu_COOH

Figure 18: DFT optimized geometry of Eu_ME
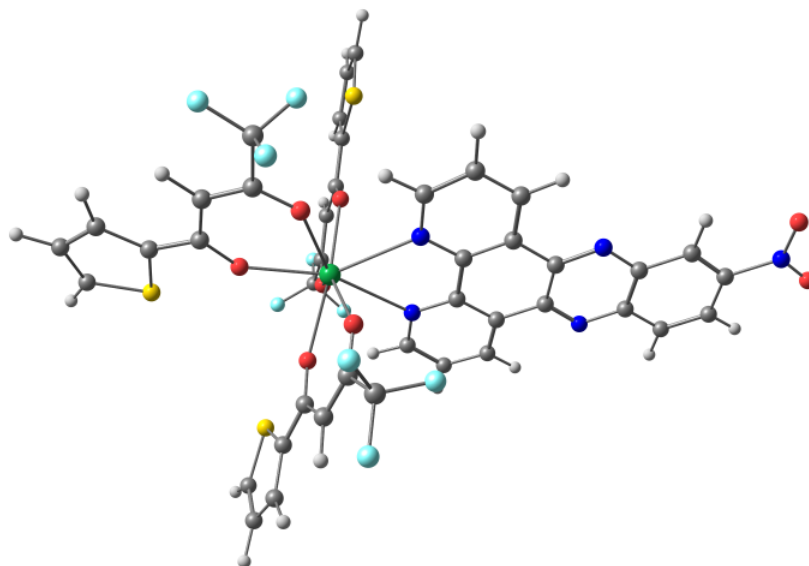
Figure 19: DFT optimized geometry of Eu_NO2

4.2 Absorption Spectra

Time-dependent DFT (TD-DFT) is performed on the optimized ground state geometries to determine the energy of the S_1 and T_1 states, ΔE_{ISC}, and the energy gap between the T_1 state and Eu(III)'s $^5D_0$ excited state, ΔE_{ET}. There are an infinite number of states that can be solved for in a TD-DFT calculation. Therefore, it is important for the experimenter to decide at the beginning of a calculation to define how many states are to be solved for by the program. The number of states chosen should be enough to capture all of the relevant information that is desired such as the correct energy ranges, the λ_{max}'s, and band shape after Gaussian broadening. The number of states solved for should also not be to many to make the calculation intractable for the machine that the calculation is being performed on.

The lowest energy λ_{max} is chosen to determine the orbital characteristics and to compare to experimental absorbance spectra. The lowest energy λ_{max} is chosen because photoluminescence is greater for excitation around the 340 nm band from excitation of the TTA ligands. Figure 20 shows the absorption spectra of the free bromine substituted DPPZ ligand, the free TTA ligand, and the Eu_Br complex all dissolved in dichloromethane. In Figure 20 the complex shows two absorption bands.
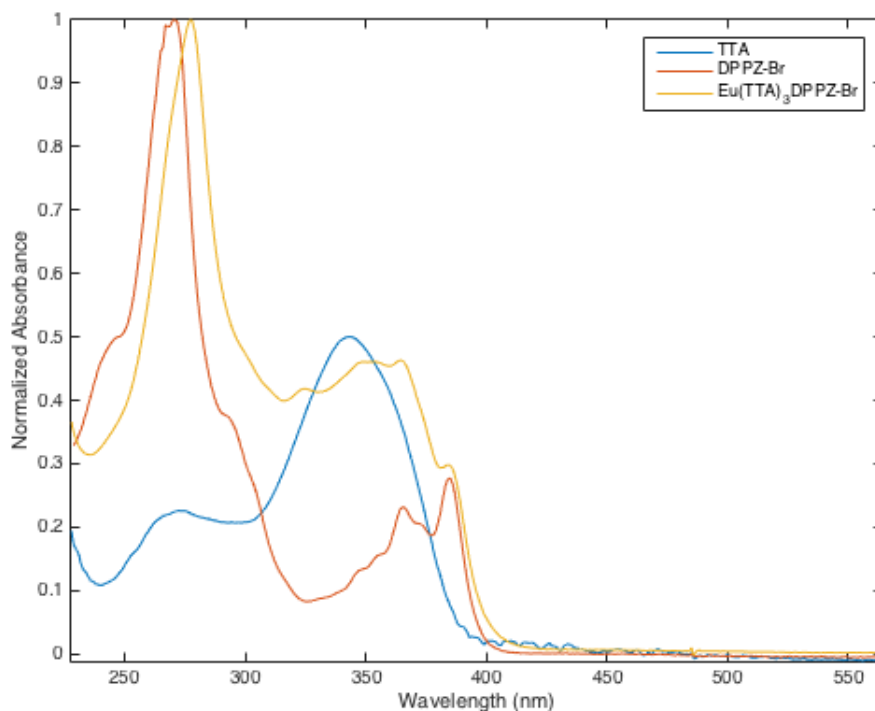
Figure 20: Normalized UV-Vis absorption spectra of the TTA and DPPZ-Br ligands.

There is a lower energy band located at around 350 nm and a higher intentsity band located at around 270 nm. When compared to the absorption bands of the free ligands the lower energy band can be attributed primarily to absorption by the TTA ligands. The higher intensity band can be attributed to absorption by the DPPZ ligand. The calculated oscillator strengths plotted with experimentally determined absorbance spectra when available are given in Figures 21 through 38.

51

Figure 21: DFT calculated singlet excited states for Eu_NH2. Oscillator strengths are plotted versus wavelength (nm)

Figure 22: DFT calculated singlet excited states for Eu_NH2. Oscillator strengths are plotted versus energy (eV).

Figure 23: DFT calculated singlet excited states for Eu_MeO. Oscillator strengths are plotted versus wavelength (nm)

Figure 24: DFT calculated singlet excited states for Eu_MeO. Oscillator strengths are plotted versus energy (eV).
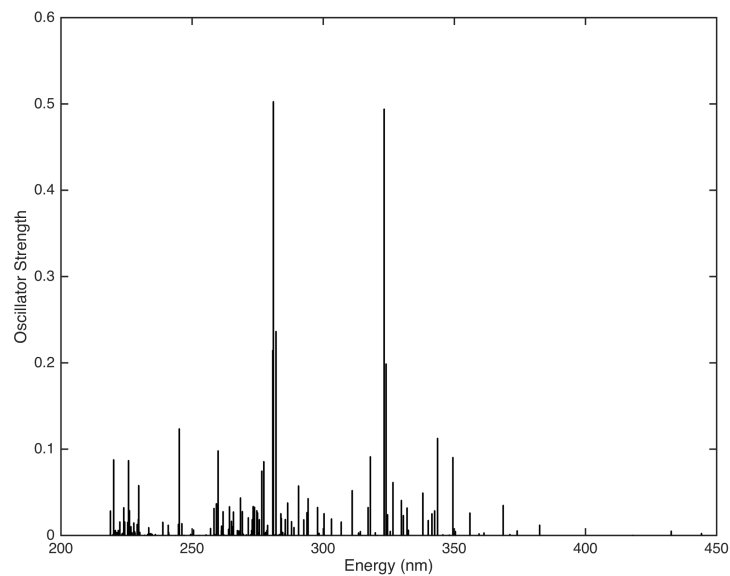
Figure 25: DFT calculated singlet excited states for Eu_CH3. Oscillator strengths are plotted versus wavelength (nm)
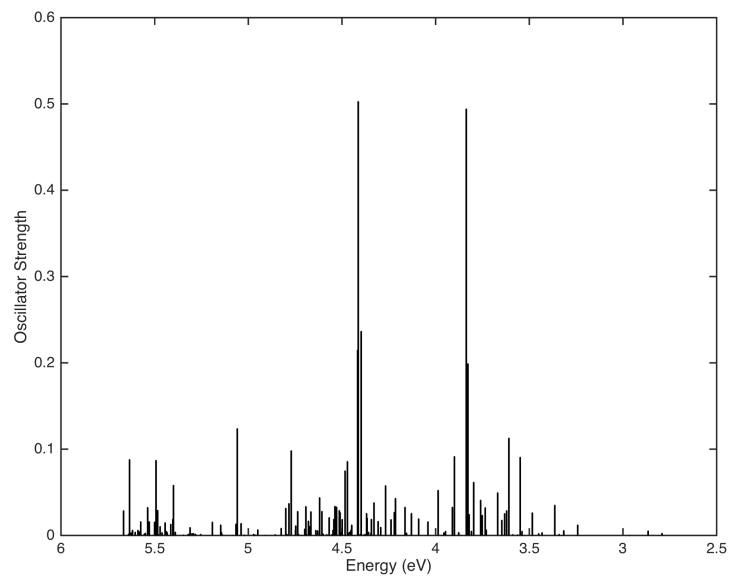
Figure 26: DFT calculated singlet excited states for Eu_CH3. Oscillator strengths are plotted versus energy (eV).
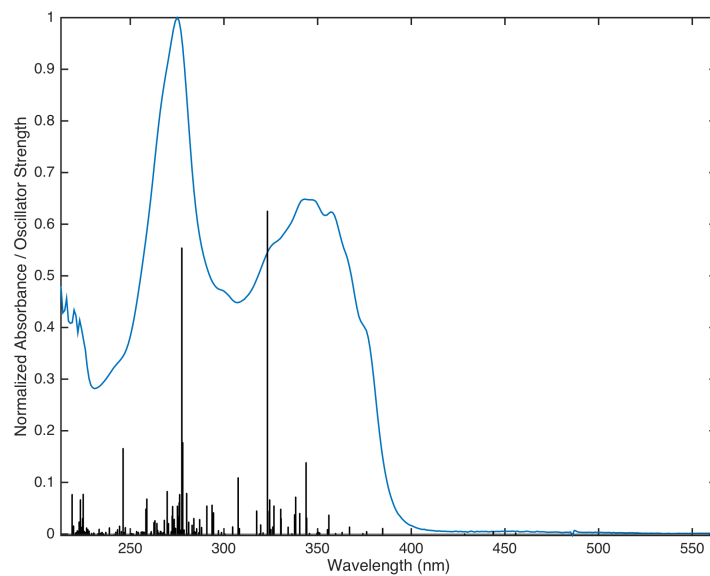
Figure 27: DFT calculated singlet excited states for Eu_H. Oscillator strengths are plotted versus wavelength (nm)
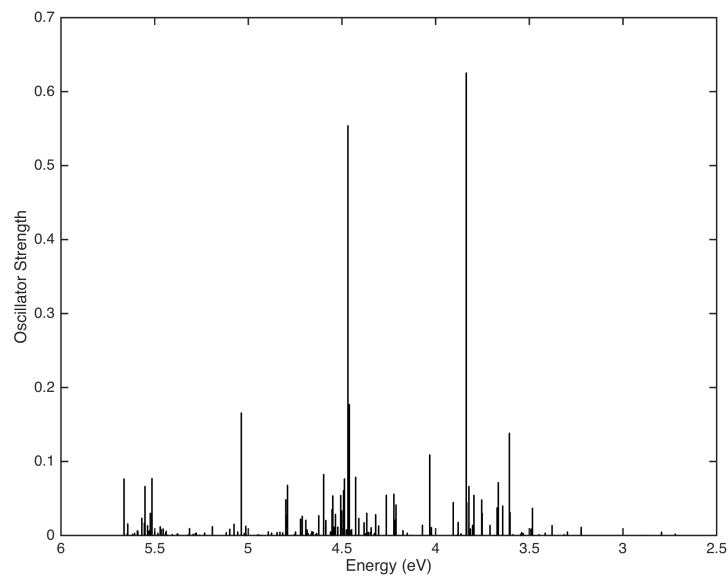
Figure 28: DFT calculated singlet excited states for Eu_H. Oscillator strengths are plotted versus energy (eV).
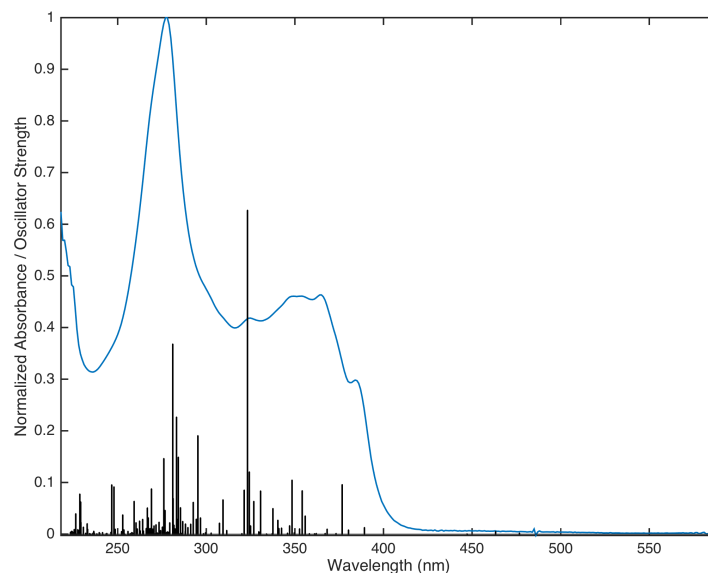
Figure 29: DFT calculated singlet excited states for Eu_Br. Oscillator strengths are plotted versus wavelength (nm)
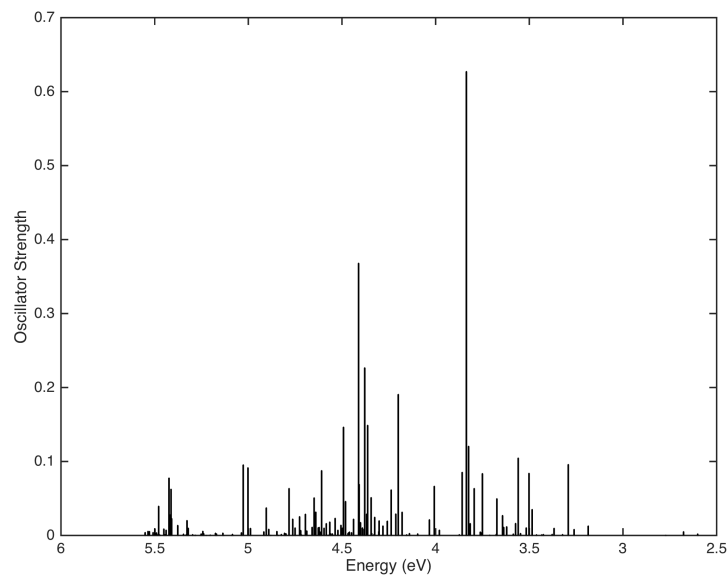
Figure 30: DFT calculated singlet excited states for Eu_Br. Oscillator strengths are plotted versus energy (eV).
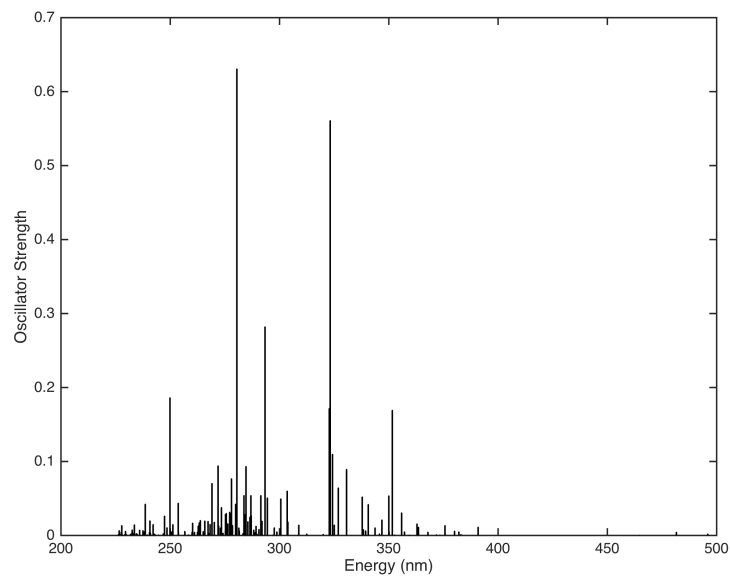
Figure 31: DFT calculated singlet excited states for Eu_COOH. Oscillator strengths are plotted versus wavelength (nm)
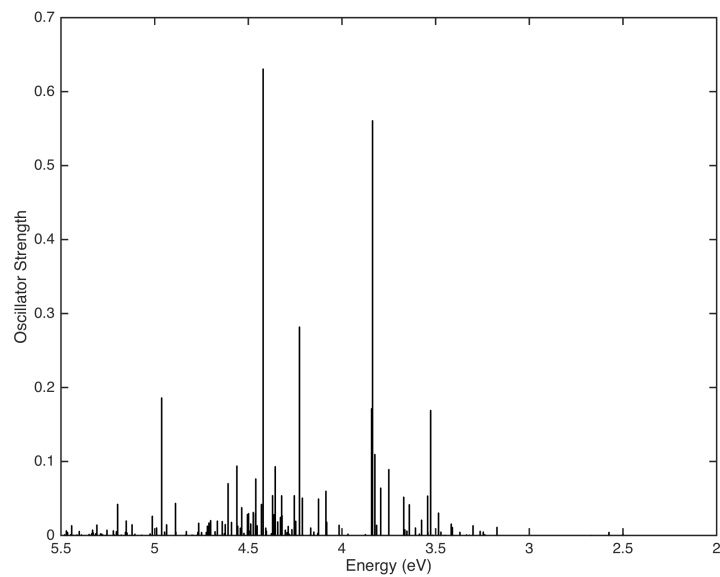
Figure 32: DFT calculated singlet excited states for Eu_COOH. Oscillator strengths are plotted versus energy (eV).

57
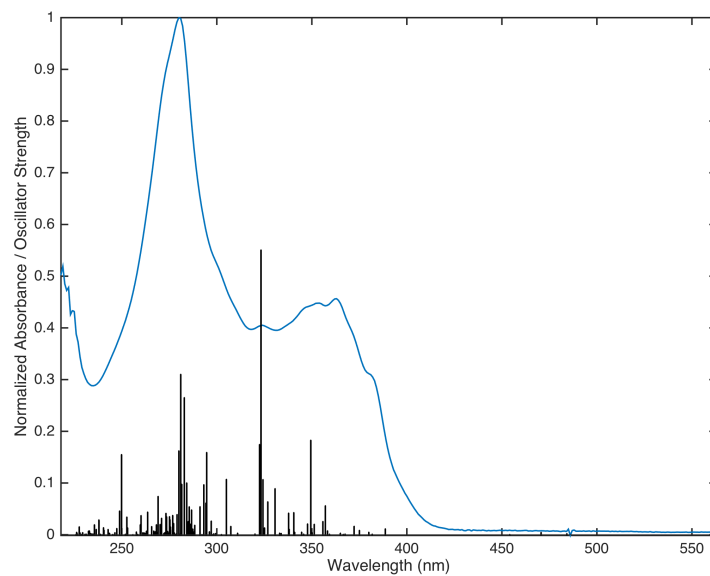
Figure 33: DFT calculated singlet excited states for Eu_ME. Oscillator strengths are plotted versus wavelength (nm)
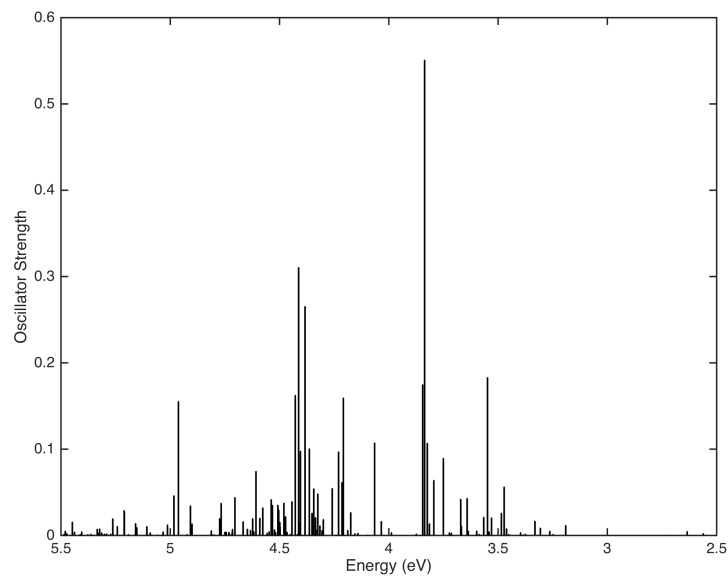
Figure 34: DFT calculated singlet excited states for Eu_ME. Oscillator strengths are plotted versus energy (eV).
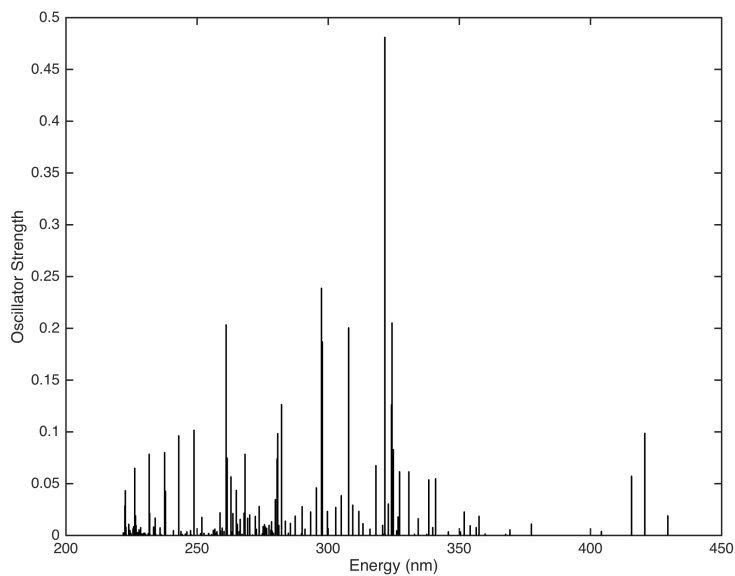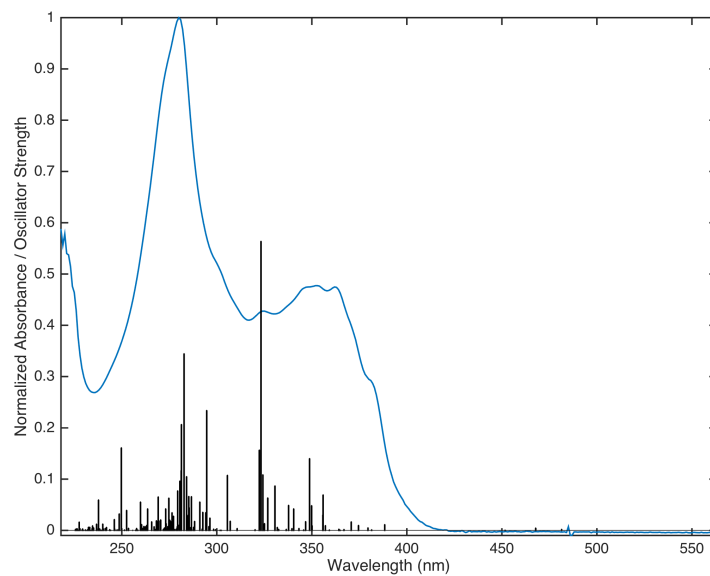
Figure 35: DFT calculated singlet excited states for Eu_EE. Oscillator strengths are plotted versus wavelength (nm)
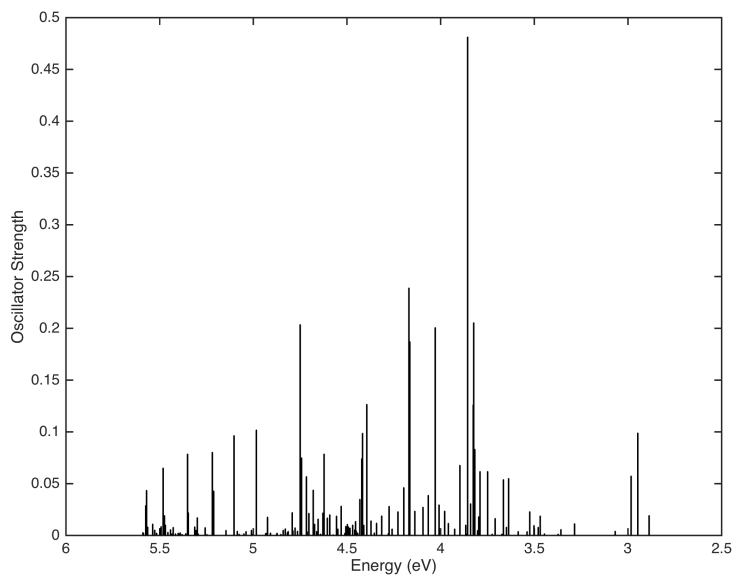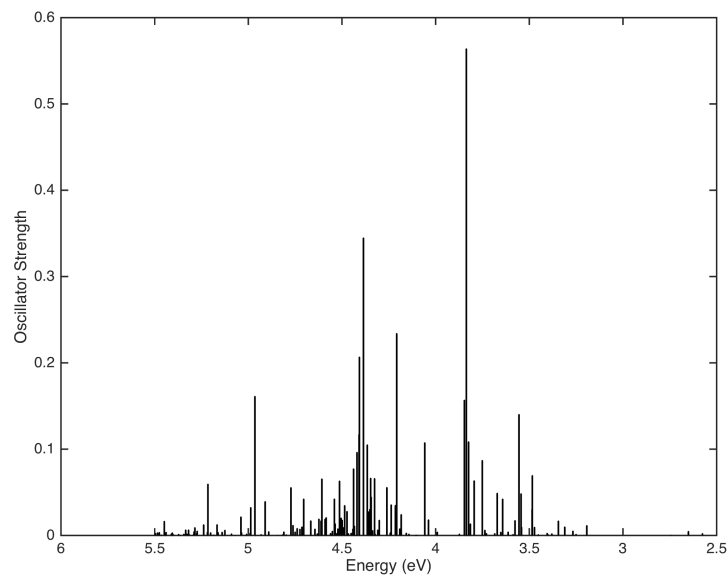

Figure 36: DFT calculated singlet excited states for Eu_EE. Oscillator strengths are plotted versus energy (eV).
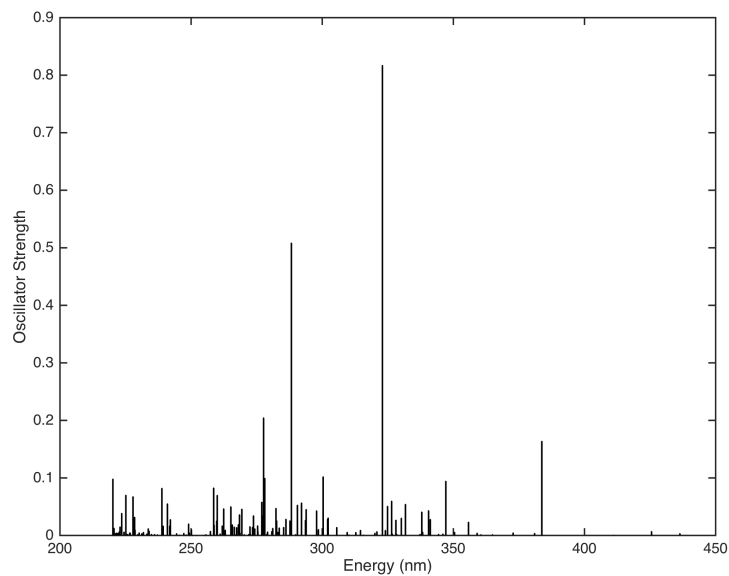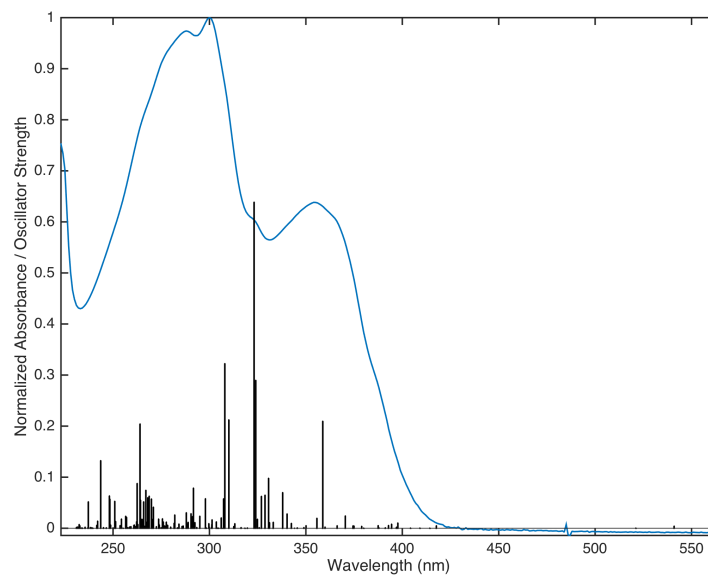
Figure 37: DFT calculated singlet excited states for Eu_NO2. Oscillator strengths are plotted versus wavelength (nm)
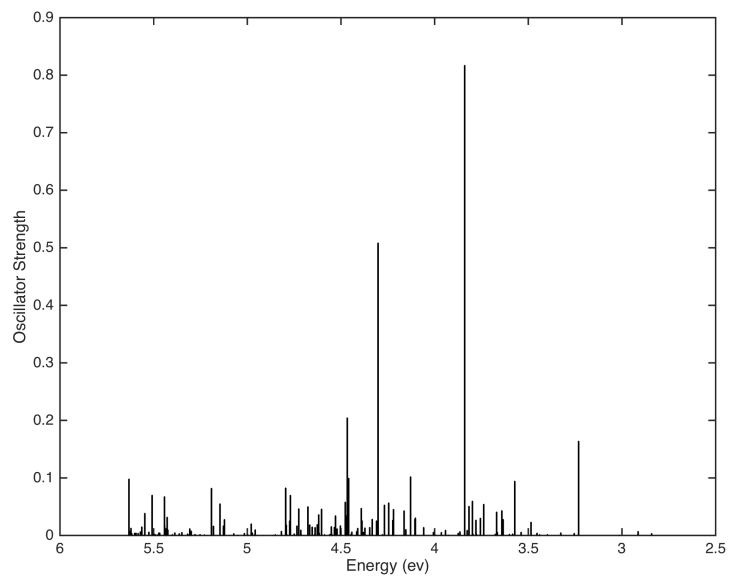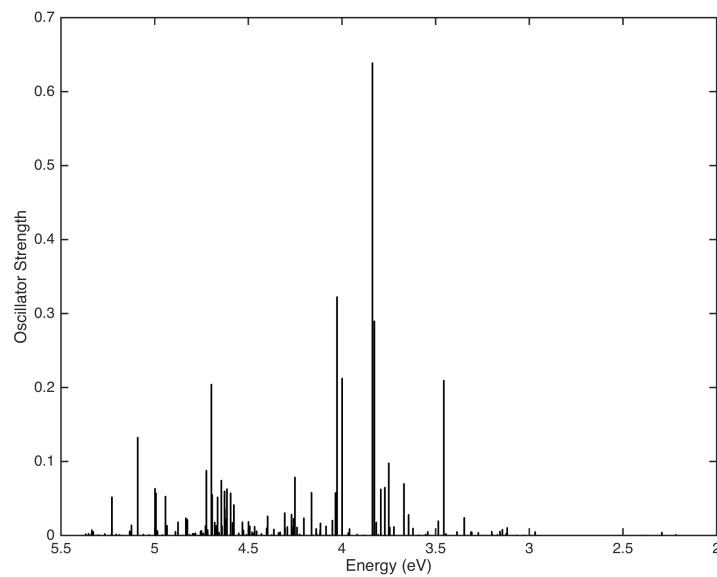

Figure 38: DFT calculated singlet excited states for Eu_NO2. Oscillator strengths are plotted versus energy (eV).

Table 5 lists the oscillator strengths and calculated λ_{max} values for all nine complexes, and the λ_{max} values of the experimental absorption spectrum of Eu(TTA)$_3$DPPZ-Br, Eu(TTA)$_3$DPPZ, Eu(TTA)$_3$DPPZ-EE, Eu(TTA)$_3$DPPZ-ME, and Eu(TTA)$_3$DPPZ-NO$_2$. The oscillator strengths represent the probability of absorption at that wavelength.

Table 5: Calculated and experimentally determined λ_{max} values with the calculated oscillator strengths.

Complex	Exp. λ_{max} (nm)	Calc. λ_{max} (nm)	Oscillator Strength (f)
Eu_NH2		297.42	0.2388
		321.59	0.4812
Eu_Br	278	281.09	0.3679
	354	323.26	0.6270
Eu_COOH		280.49	0.6306
		323.19	0.5607
Eu_H	274	277.52	0.5540
	349	323.21	0.6253
Eu_EE	280	282.76	0.3445
	353	323.25	0.5637
Eu_ME	280	281.01	0.3102
	363	323.25	0.5506
Eu_MeO		288.24	0.5080
		322.95	0.8168
Eu_CH3		280.98	0.5027
		323.22	0.4941
Eu_NO2	300	307.97	0.3225
	353	323.14	0.6387

The calculated higher energy bands have λ_{max} values ranging between 277 nm and 307 nm corresponding to absorption by DPPZ. These absorption bands correspond very well to the experimentally determined absorption band maximums, which are summarized in Table 5. The calculated lower energy λ_{max} absorption values for all nine complexes are around 323 nm which, according to Figure 20, is indicative of absorption by TTA. The calculated

lowest energy λ_{max}'s are blue shifted by about 30 to 40 nm of the experimental lowest energy absorption maximum. Much of the discrepancy between the calculated and experimentally determined absorption band maximums can be attributed to solvatochromic effects as a result of the calculations being performed in the gas phase. More agreeable results are expected by including a dichloromethane solvation model into the calculation.

From the calculated oscillator strengths in Figures 21 to 38 ligand substitution has the greatest effect on where the higher intensity band at around 270 nm is located. Referring back to Figure 20 this absorption band is primarily due to the DPPZ ligand. Qualitatively it would be expected that changes in excited state energies would occur with ligand substitution because of the various substituents attached to the DPPZ ligand. Though there does not seem to be any trend between electron donating or electron withdrawing effects. The band position for the lower energy oscillators is relatively unaffected as a result of absorption by TTA. Similar λ_{max} values are seen in the study by Sun *et al.*[47] for Eu_H and Eu_CH3 where the authors report λ_{max} values of 274 nm and 342 nm for Eu_H and 278 nm and 342 nm for Eu_CH3. These values show good agreement with the experimentally determined and calculated values in Table 5.

4.3   Energy Transfer Analysis

Eu(TTA)$_3$DPPZ-NH$_2$
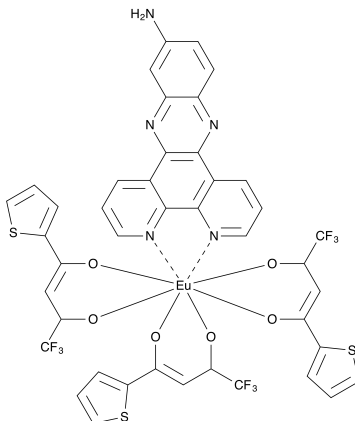
Figure 39: Structure of Eu_NH2

The following section highlights the calculated results for the amine substitution to the DPPZ ligand (DPPZ-NH$_2$). At the time of the writing of this thesis, synthesis of the Eu(TTA)$_3$DPPZ-NH$_2$ (Eu_NH2) complex has not yet been done. Since there is no experimental data, results will be presented as is and without comparison to experiment. Excited state details are provided in Table 6 and plots of the primary orbitals involved in the excited state are presented in Figure 40.

Table 6: The orbital transitions and contribution to the $\lambda_{max} = 321.59$ nm excited state of Eu_NH2.

HOMO Orbital		LUMO Orbital	% Contribution
H - 3	$\rightarrow$	L + 2	5.65
H - 3	$\rightarrow$	L + 3	58.5
H - 3	$\rightarrow$	L + 4	3.25
H - 1	$\rightarrow$	L + 2	6.91
HOMO	$\rightarrow$	L + 4	8.77
HOMO	$\rightarrow$	L + 5	6.24

63

(a) H-3   (b) L+3
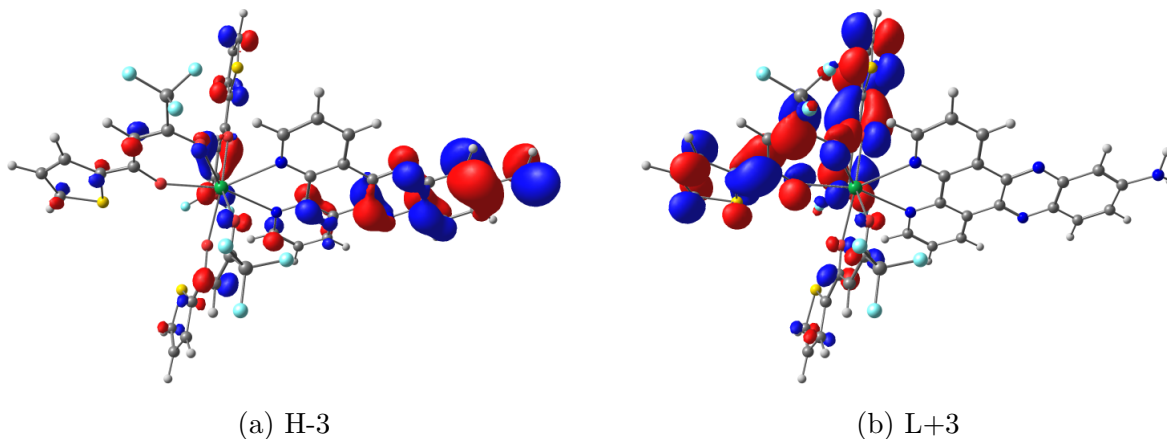
Figure 40: The dominant transition for this excited state is from the H-3 (a) orbital to the L+3 (b) orbital (58.5 %). Analysis of the the orbitals for this transition presents [π(DPPZ-NH$_2$, TTA) $\rightarrow$ π*(TTA)] character implying a LLCT and some intra-ligand charge transfer (ILCT).

The energy of the S$_1$ state was calculated to be 2.8868 eV. Triplet state calculations were performed in order to ascertain the orbitals involved as well as determining the energy of intersystem crossing (ΔE_{ISC}) and the energy transfer gap between the ligand based T$_1$ and the ^{5}D$_0$ excited state of Eu(III) (ΔE_{ET}). The lowest energy triplet state (T$_1$) was calculated to be 2.1065 eV. This T$_1$ excited state is attributed electronic excitations of DPPZ localized $\pi - \pi$* transitions.
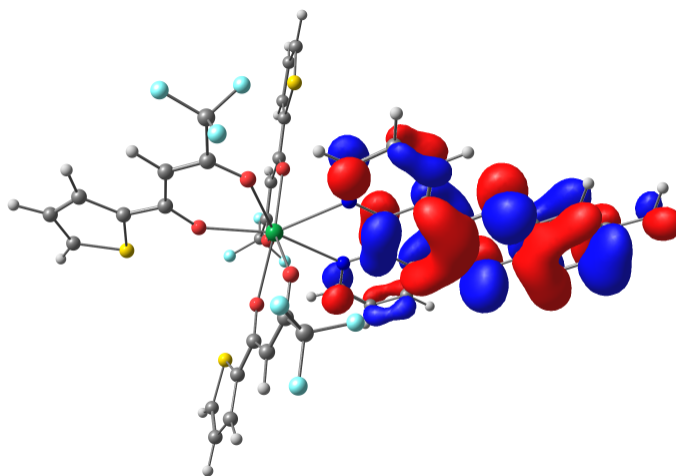
Figure 41: Lowest T$_1$ orbital of Eu_NH2.

Based on the calculated values of the lowest S_1 and T_1 states and based on a value of 2.0193 eV $^5D_0 \rightarrow^7 F_2$ energy, the ΔE_{ISC} and ΔE_{ET} can be calculated for Eu_NH2. The energy of intersystem crossing ΔE_{ISC} was calculated to be 0.7803 eV. The energy transfer gap ΔE_{ET} was calculated to be 0.0872 eV.

Eu(TTA)$_3$DPPZ-MeO

Figure 42: Structure of Eu_MeO.

In this section calculated singlet state and triplet state results for the methoxy substituted DPPZ (DPPZ-MeO) are presented for the Eu(TTA)$_3$DPPZ-MeO (Eu_MeO) complex. At the time of the writing of this thesis synthesis of the Eu_CH3 complex has not yet been done. Since there is no experimental data, results will be presented as is and without comparison to experiment. Excited state details are provided in Table 7 and plots of the primary orbitals involved in the excited state are presented in Figure 43 and Figure 44.

Table 7: The orbital transitions and contribution to the $\lambda_{max} = 322.95$ nm excited state of Eu_MeO.

HOMO Orbital		LUMO Orbital	% Contribution
H - 2	$\rightarrow$	L + 2	11.1
H - 2	$\rightarrow$	L + 3	29.3
H - 1	$\rightarrow$	L + 2	10.8
HOMO	$\rightarrow$	L + 5	31.4

(a) H-1

(b) L+3
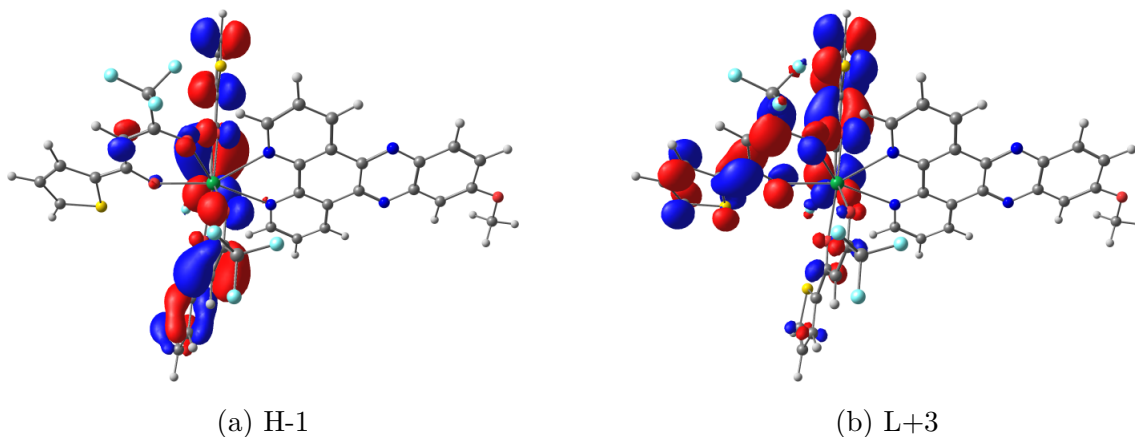
Figure 43: The first dominant transition is the H-1 (a) to L+3 (b) transition, which is (ILCT)[π(TTA) $\rightarrow$ π*(TTA)] in character.

(a) HOMO

(b) L+5
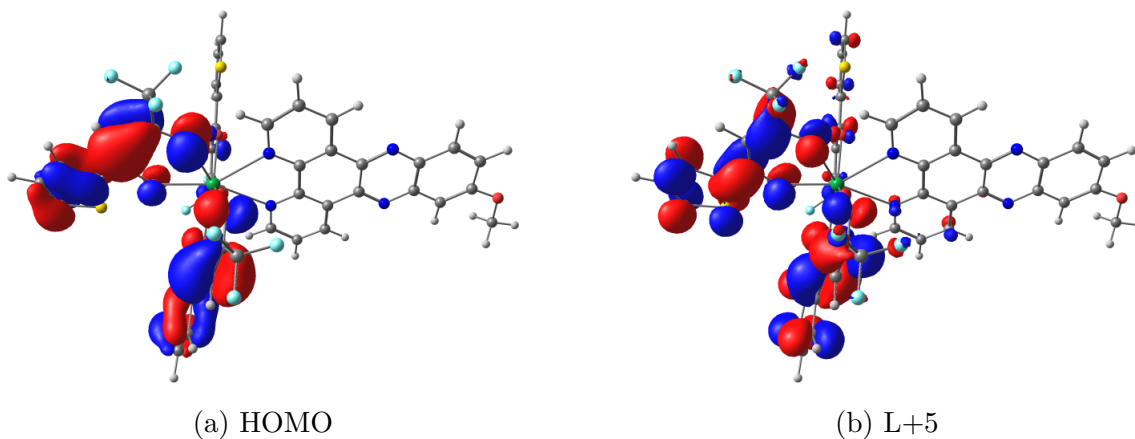
Figure 44: The second dominant transition is the HOMO (a) to L+5 (b) transition which is (ILCT)[π(TTA) $\rightarrow$ π*(TTA)] in character.

The energy of the S_1 state was calculated to be 2.8412 eV, and the T_1 energy was calculated to be 2.3256 eV. The T_1 state is attributed to DPPZ-MeO localized $\pi \rightarrow \pi$* transition.
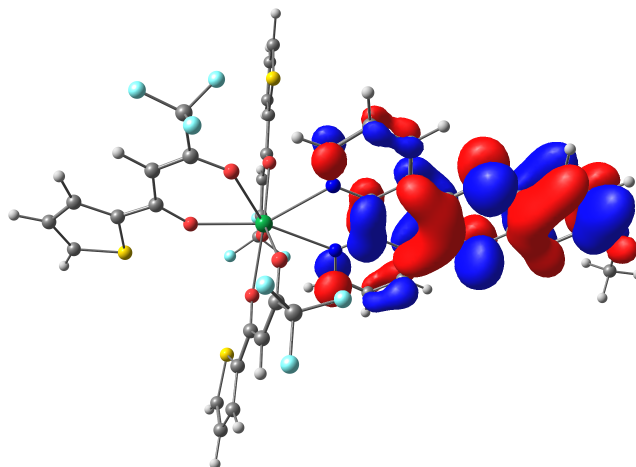
Figure 45: Lowest T_1 orbital of Eu_MeO.

Based on the calculated values of the lowest S_1 and T_1 states and based on a value of 2.0193 eV for the $^5D_0 \rightarrow ^7F_2$ energy, the ΔE_{ISC} and ΔE_{ET} can be calculated for Eu_MeO. The energy of intersystem crossing ΔE_{ISC} was calculated to be 0.5156 eV. The energy transfer gap ΔE_{ET} was calculated to be 0.3063 eV.

Eu(TTA)$_3$DPPZ-CH3
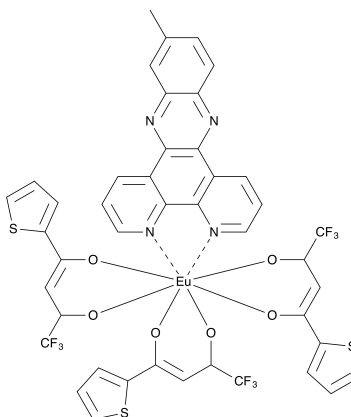
Figure 46: Structure of Eu_CH3

In this section calculated singlet state and triplet state results for the methyl substituted DPPZ (DPPZ-CH$_3$) are presented for the Eu(TTA)$_3$DPPZ-CH$_3$ (Eu_CH3) complex. At the time of the writing of this thesis synthesis of the Eu_CH3 complex has not yet been done.

Since there is no experimental data, results will be presented as is and without comparison to experiment. Excited state details are provided in Table 8 and plots for the two primary orbital transitions involved in the excited state are presented in Figure 47 and Figure 48.

Table 8: The orbital transitions and contribution to the $\lambda_{max} = 323.22$ nm excited state of Eu_CH3

HOMO Orbital		LUMO Orbital	% Contribution
H - 13	$\rightarrow$	L + 3	3.24
H - 11	$\rightarrow$	LUMO	3.53
H - 10	$\rightarrow$	LUMO	9.64
H - 9	$\rightarrow$	L + 2	3.07
H - 4	$\rightarrow$	L + 1	4.67
H - 2	$\rightarrow$	L + 2	7.41
H - 2	$\rightarrow$	L + 3	21.6
H - 1	$\rightarrow$	L + 2	7.21
HOMO	$\rightarrow$	L + 5	22.5

(a) H-2   (b) L+3
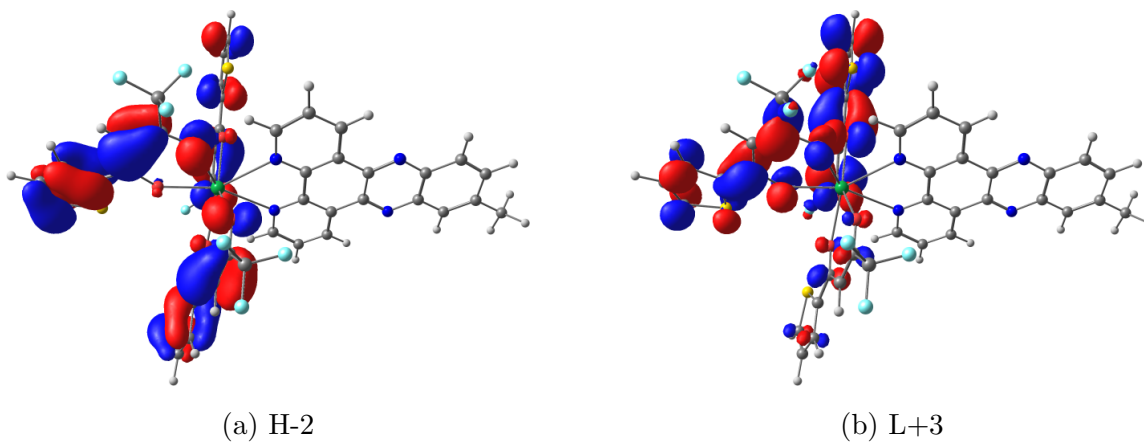
Figure 47: The first primary transition is the H-2 (a) to L+3 (b) transition, which is (ILCT)$[\pi(\text{TTA}) \rightarrow \pi^*(\text{TTA})]$ in character.

(a) HOMO   (b) L+5
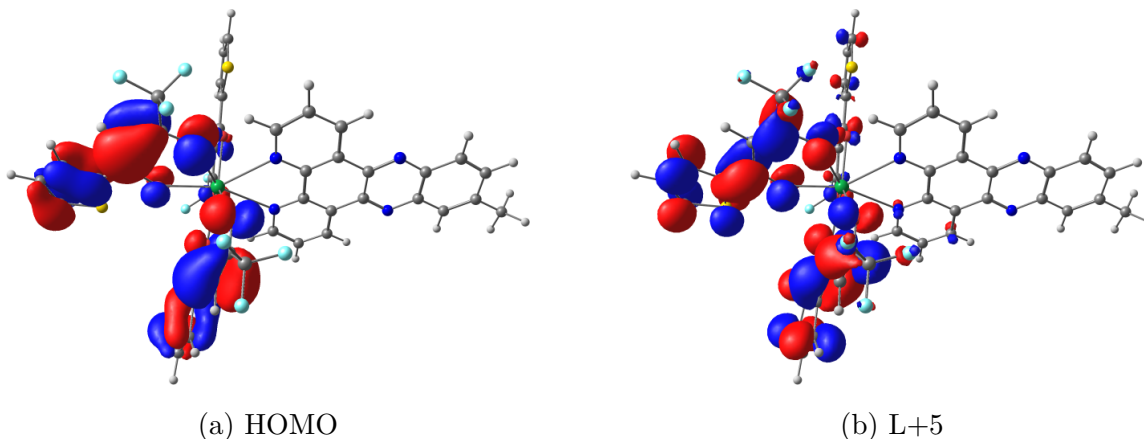
Figure 48: The second primary transition is the HOMO (a) to L+5 (b) transition, which is (ILCT)[π(TTA) $\rightarrow$ π*(TTA)] in character

The lowest energy S_1 state was calculated to be 2.7911 eV. The T_1 energy was calculated to be 2.3183 eV. The T_1 state is attributed to DPPZ-CH$_3$ localized $\pi \rightarrow \pi$* transition.
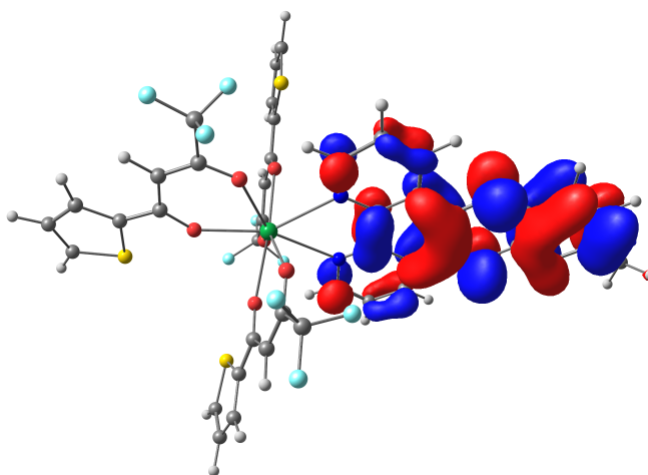
Figure 49: Lowest T_1 orbital of Eu_CH3.

Based on the calculated values of the lowest S_1 and T_1 states and based on a value of 2.0193 eV for the $^5D_0 \rightarrow^7 F_2$ energy, ΔE_{ISC} and ΔE_{ET} can be calculated for Eu_CH3. The energy of intersystem crossing ΔE_{ISC} was calculated to be 0.4728 eV. The energy transfer gap ΔE_{ET} was calculated to be 0.2990 eV.
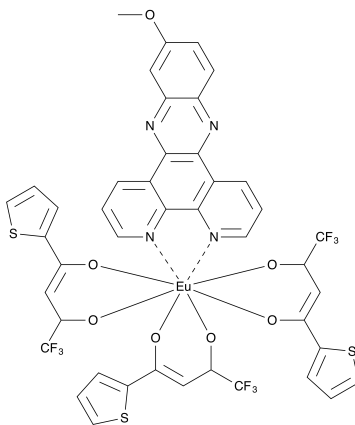
Eu(TTA)$_3$DPPZ
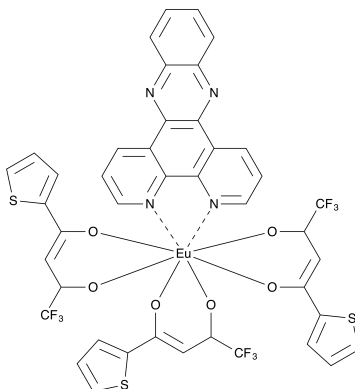
Figure 50: Structure of Eu_H

In this section calculated singlet state and triplet state results for the unsubstituted DPPZ are presented and compared with experimentally determined absorption data. The orbital contributions to the excited state at 323.21 nm is presented in the Table 9. The two primary orbital transitions are visualized in Figure 51 and Figure 52.

Table 9: The orbital transitions and contribution to the $\lambda_{max} = 323.21$ nm for Eu_H

HOMO Orbital		LUMO Orbital	% Contribution
H - 12	$\rightarrow$	LUMO	2.85
H - 10	$\rightarrow$	LUMO	5.83
H - 5	$\rightarrow$	L + 1	2.22
H - 2	$\rightarrow$	L + 2	8.21
H - 2	$\rightarrow$	L + 3	3.37
H - 2	$\rightarrow$	L + 4	24.3
H - 1	$\rightarrow$	L + 2	7.76
H - 1	$\rightarrow$	L + 3	2.43
HOMO	$\rightarrow$	L + 5	28.1

(a) HOMO-2   (b) LUMO+4

Figure 51: The first primary transition is the H-2 (a) orbital to the L+4 (b) orbital, which is (ILCT)[π(TTA) $\rightarrow$ π*(TTA)] in character.


(a) HOMO   (b) LUMO+5

Figure 52: The second primary transition is the HOMO (a) orbital to the L+5 (b) orbital, which is (ILCT)[π(TTA) $\rightarrow$ π*(TTA)] in character.

The S_1 energy was calculated to be 2.7205 eV. The T_1 energy was determined to be 2.3033 eV. The T_1 state is attributed to DPPZ localized $\pi \rightarrow \pi$* transition.
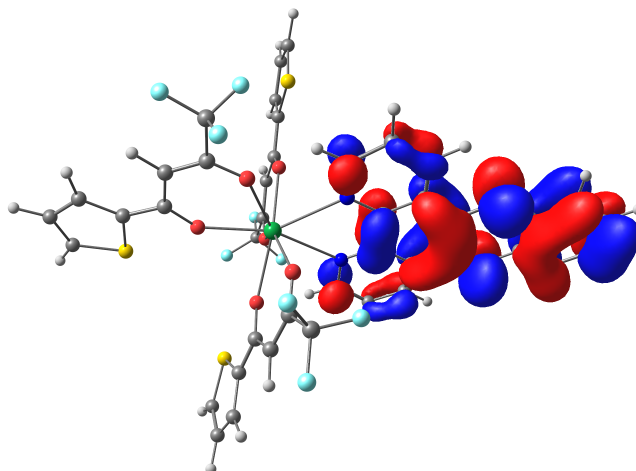
Figure 53: Eu_H triplet orbital.

Based on the calculated values of the lowest S_1 and T_1 states and based on a value of 2.0193 eV for the $^5D_0 \rightarrow^7 F_2$ energy, ΔE_{ISC} and ΔE_{ET} can be calculated for Eu_H. The energy of intersystem crossing ΔE_{ISC} was calculated to be 0.4172 eV. The energy transfer gap ΔE_{ET} to Eu_H's excited state is calculated to be 0.2840 eV.

Eu(TTA)$_3$DPPZ-Br
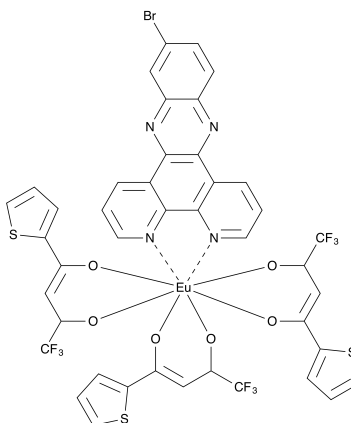
Figure 54: Structure of Eu_Br

The following section highlights the calculated results for the bromine substitution to the DPPZ ligand europium complex Eu(TTA)$_3$DPPZ-Br (Eu_Br). TD-DFT calculations were

performed to determine the electronic structure of the singlet and triplet states as well as to compare to experimental absorption spectra. Orbital contributions to the excited state at 323.26 nm is presented in Table 10. There are two dominant transitions that contribute to this excited state, which are visualized in Figure 55 and in Figure 56.

Table 10: The orbital transitions and contribution to the $\lambda_{max} = 323.26$ nm of Eu_Br.

HOMO Orbital		LUMO Orbital	% Contribution
H - 15	$\rightarrow$	LUMO	5.23
H - 13	$\rightarrow$	L + 3	2.17
H - 13	$\rightarrow$	L + 4	2.63
H - 10	$\rightarrow$	L + 4	2.79
H - 8	$\rightarrow$	L + 4	2.29
H - 5	$\rightarrow$	L + 1	3.48
H - 2	$\rightarrow$	L + 3	8.87
H - 2	$\rightarrow$	L + 4	25.3
H - 1	$\rightarrow$	L + 3	10.2
HOMO	$\rightarrow$	L + 5	27.0

(a)   (b)
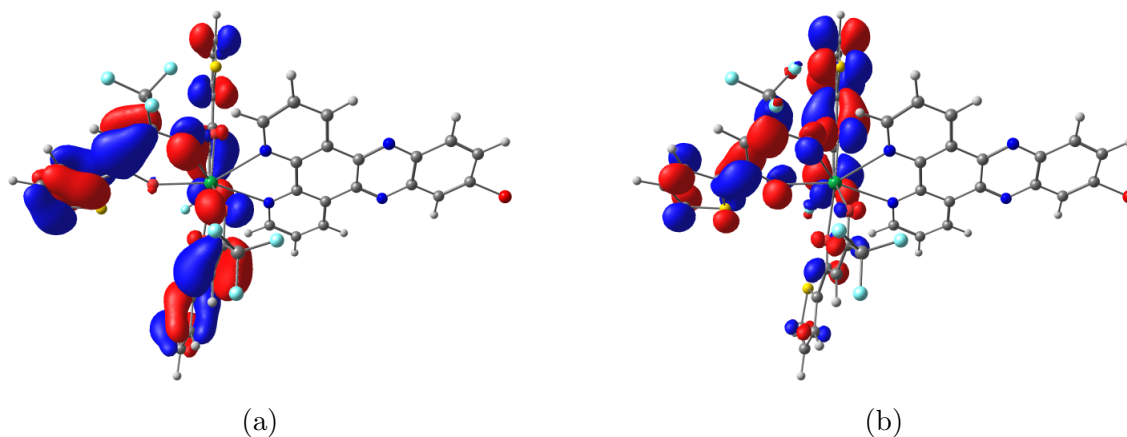
Figure 55: The first dominant transition is the H-2 (a) orbital to the L+4 (b) orbital, which is (ILCT)[π(TTA) $\rightarrow$ π*(TTA)] in character.

(a)   (b)

Figure 56: The second dominant transition is the HOMO (a) orbital to the L+5 (b) orbital, which is (ILCT)$[\pi(\text{TTA}) \rightarrow \pi^*(\text{TTA})]$ in character.

The S_1 energy was calculated to be 2.6008 eV. The calculated T_1 energy was calculated to be 2.2868 eV. The T_1 excited state is attributed to $\pi \rightarrow \pi^*$ excitations localized on the DPPZ-Br ligand.
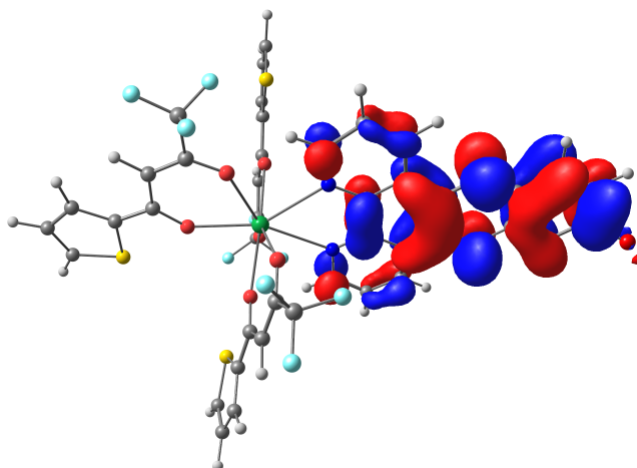
Figure 57: Eu_Br T_1 orbital

Based on the calculated values of the lowest S_1 and T_1 states, and based on a value of 2.0193 eV for the $^5D_0 \rightarrow ^7F_2$ energy, ΔE_{ISC} and ΔE_{ET} can be calculated for Eu_Br. The energy of intersystem crossing ΔE_{ISC} was calculated to be 0.314 eV. The energy transfer to gap ΔE_{ET} was calculated to be 0.2675 eV.

74
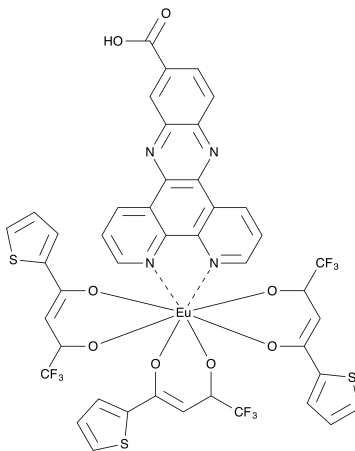
<u>Eu(TTA)$_3$DPPZ-COOH</u>

Figure 58: Structure of Eu_COOH.

In this section calculated singlet state and triplet state results for the carboxylic acid substituted DPPZ (DPPZ-COOH) are presented for the Eu(TTA)$_3$DPPZ-COOH (Eu_COOH) complex. At the time of the writing of this thesis synthesis of the Eu_COOH complex has not yet been done. Since there is no experimental data, results will be presented as is and without comparison to experiment. The orbital transitions involved in the excited are listed in Table 11. There are two dominant transitions that contribute to the excited state, which are visualized in Figure 59 and in Figure 60.

Table 11: The orbital transitions and contribution to the $\lambda_{max} = 323.19$ nm for Eu_COOH.

HOMO Orbital		LUMO Orbital	% Contribution
H - 15	$\rightarrow$	LUMO	13.6
H - 6	$\rightarrow$	L + 1	2.83
H - 2	$\rightarrow$	L + 3	8.84
H - 2	$\rightarrow$	L + 4	23.3
H - 1	$\rightarrow$	L + 3	9.49
HOMO	$\rightarrow$	L + 5	25.7

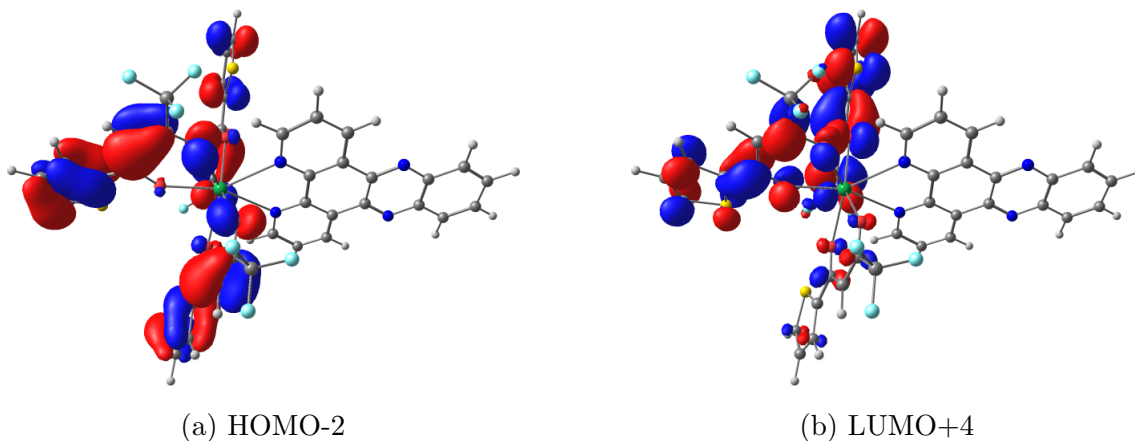(a) H-2   (b) L+4
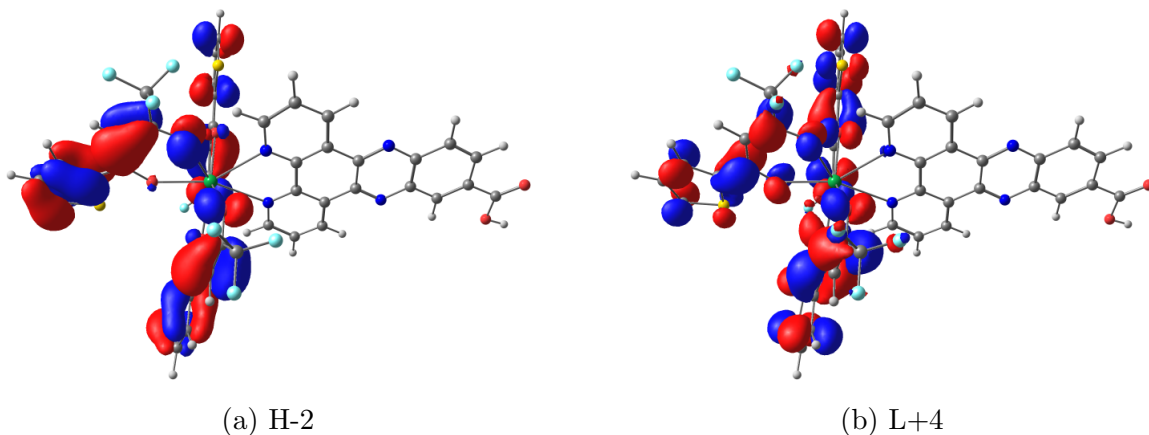
Figure 59: The first dominant transition is the H-2 (a) orbital to the L+4 (b) orbital, which is (ILCT)$[\pi(\text{TTA}) \rightarrow \pi^*(\text{TTA})]$ in character.
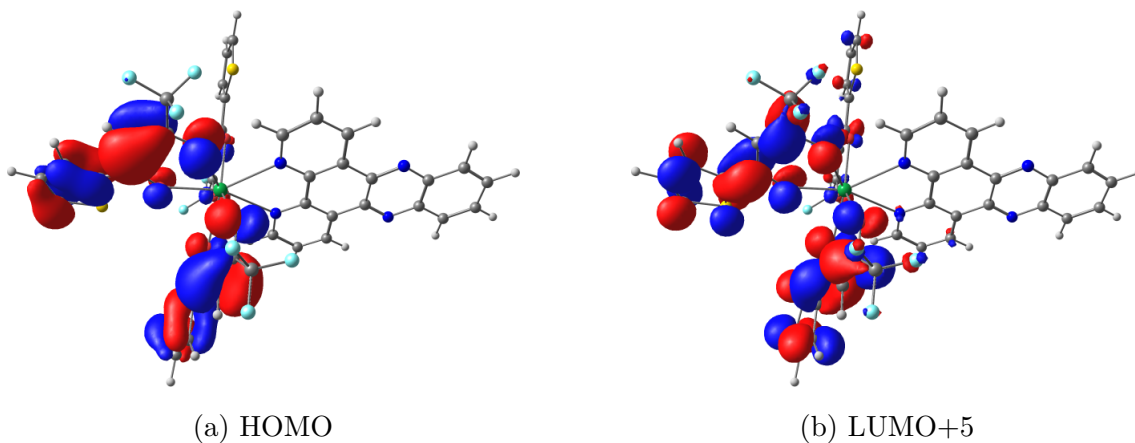

(a) HOMO   (b) L+5

Figure 60: The second dominant transition is the HOMO (a) orbital to the L+5 (b) orbital, which is (ILCT)$[\pi(\text{TTA}) \rightarrow \pi^*(\text{TTA})]$ in character.

The energy for the S_1 state was calculated to be 2.5000 eV. The T_1 energy was calculated to be 2.2722 eV. The T_1 state is attributed to DPPZ-COOH localized $\pi \rightarrow \pi^*$ transition.

Figure 61: Lowest T_1 orbital of Eu_COOH.

Based on the calculated values of the lowest S_1 and T_1 states and based on a value of 2.0193 eV for the $^5D_0 \rightarrow^7 F_2$ energy, ΔE_{ISC} and ΔE_{ET} can be calculated for Eu_NH2. The energy of intersystem crossing ΔE_{ISC} was calculated to be 0.2278 eV. The energy transfer gap ΔE_{ET} was calculated to be 0.2529 eV.

Eu(TTA)$_3$DPPZ-ME
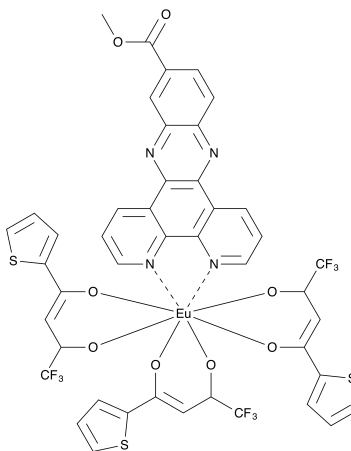
In this section calculated singlet state and triplet state results for the methyl ester substituted DDPZ (DPPZ-ME) of the Eu(TTA)$_3$DPPZ-ME (Eu_ME) are presented and compared with experimentally determined absorption data. The orbital transitions involved in the ex-

cited state at 323.25 nm is presented in Table 12. There are two dominant transitions that contribute to the excited state, which are visualized in Figure 62 and in Figure 63.

Table 12: The orbital transitions and contribution to the $\lambda_{max} = 323.25$ nm of Eu_ME.

HOMO Orbital		LUMO Orbital	% Contribution
H - 15	$\rightarrow$	LUMO	13.7
H - 6	$\rightarrow$	L + 1	3.64
H - 2	$\rightarrow$	L + 3	9.29
H - 2	$\rightarrow$	L + 4	22.5
H - 1	$\rightarrow$	L + 3	9.06
HOMO	$\rightarrow$	L + 5	25.1
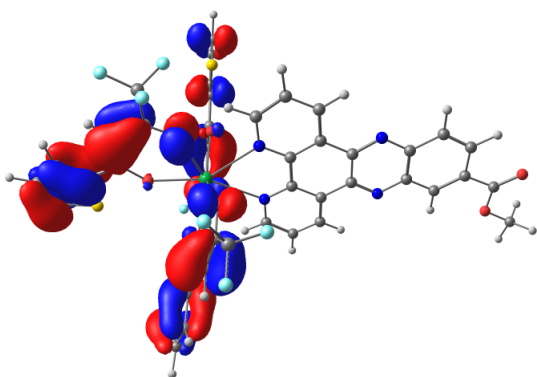
(a) H-2
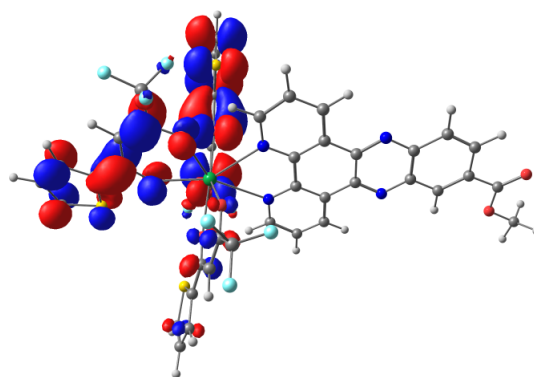
(b) L+4

Figure 62: The first dominant transition is the H-2 (a) orbital to the L+4 (b) orbital, which is (ILCT)$[\pi(\text{TTA}) \rightarrow \pi^*(\text{TTA})]$ in character.
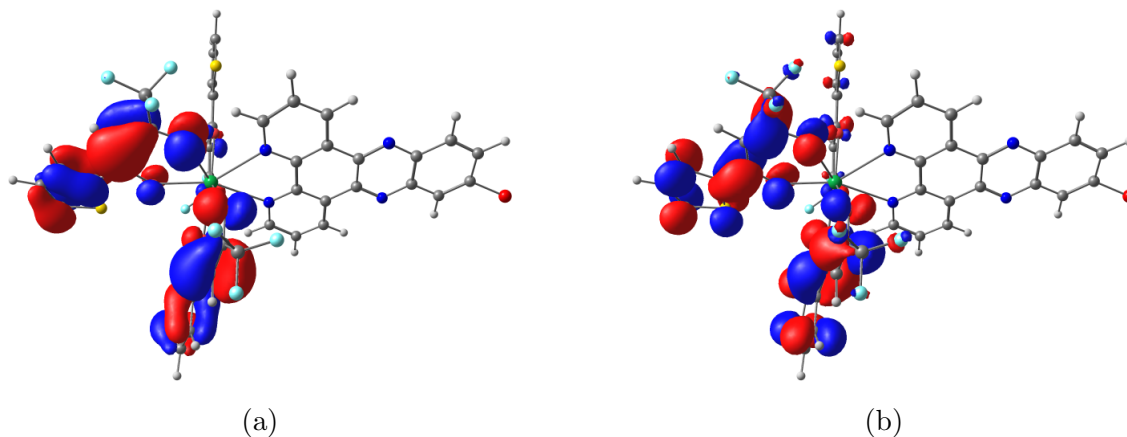
(a) HOMO   (b) L+5

Figure 63: The second dominant transition is the HOMO (a) orbital to the L+5 (b) orbital, which is (ILCT)[π(TTA) $\to$ π*(TTA)] in character.

The energy of the S_1 state was calculated to be 2.5607 eV. The T_1 energy was calculated to be 2.2680 eV. The T_1 state is attributed to DPPZ localized $\pi \to \pi$* transition.

Figure 64: Lowest T_1 orbital of Eu_ME.

Based on the calculated values of the lowest S_1 and T_1 states and based on a value of 2.0193 eV for the $^5D_0 \to ^7F_2$ energy, ΔE_{ISC} and ΔE_{ET} can be calculated for Eu_ME. The energy of intersystem crossing ΔE_{ISC} was calculated to be 0.2927 eV. The energy transfer to gap ΔE_{ET} was calculated to be 0.2487 eV.

Eu(TTA)₃DPPZ-EE
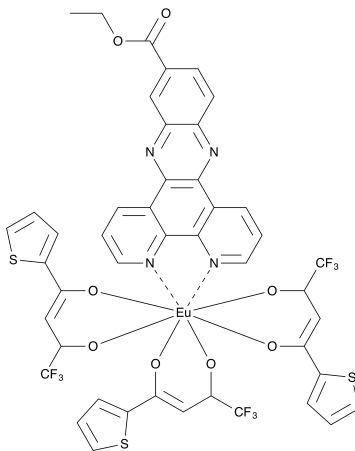
Figure 65: Structure of Eu(TTA)₃DPPZ-EE

In this section calculated singlet state and triplet state results for the ethyl ester substituted DPPZ ligand are presented and compared with experimentally determined absorption data for the Eu(TTA)₃DPPZ-EE (Eu_EE) complex. The orbital transitions involved in the excited state at 323.25 nm is presented in Table 13. There are two dominant transitions that contribute to the excited state, which are visualized in Figure 66 and in Figure 67.

Table 13: The orbital transitions and contribution to the $\lambda_{max} = 323.25$ nm excited state of Eu_EE.

| HOMO Orbital		LUMO Orbital	% Contribution
H - 15	$\rightarrow$	LUMO	11.7
H - 6	$\rightarrow$	L + 1	3.43
H - 2	$\rightarrow$	L + 3	9.50
H - 2	$\rightarrow$	L + 4	22.9
H - 1	$\rightarrow$	L + 3	9.27
HOMO	$\rightarrow$	L + 5	25.6

(a) H-2   (b) L+4
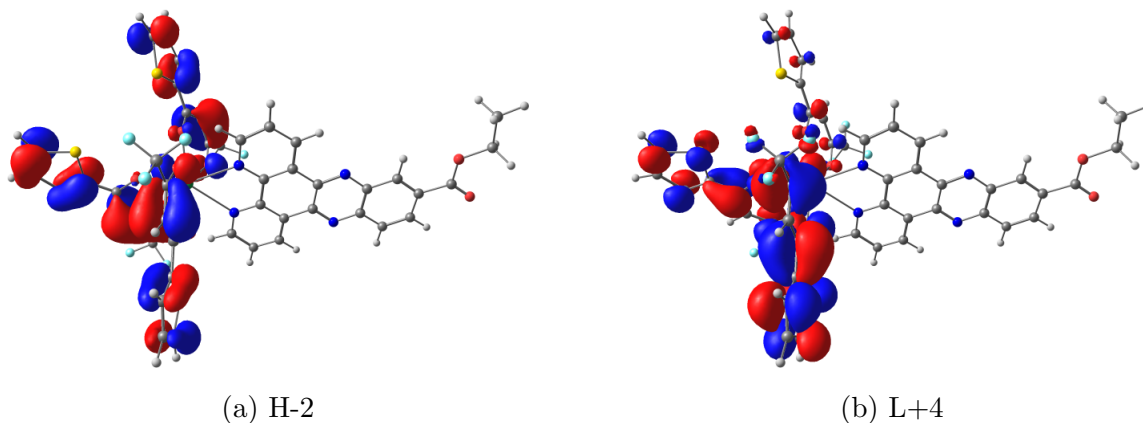
Figure 66: The first dominant transition is the H-2 (a) orbital to the L+4 (b) orbital, which is (ILCT)[π(TTA) $\rightarrow$ π*(TTA)] in character.
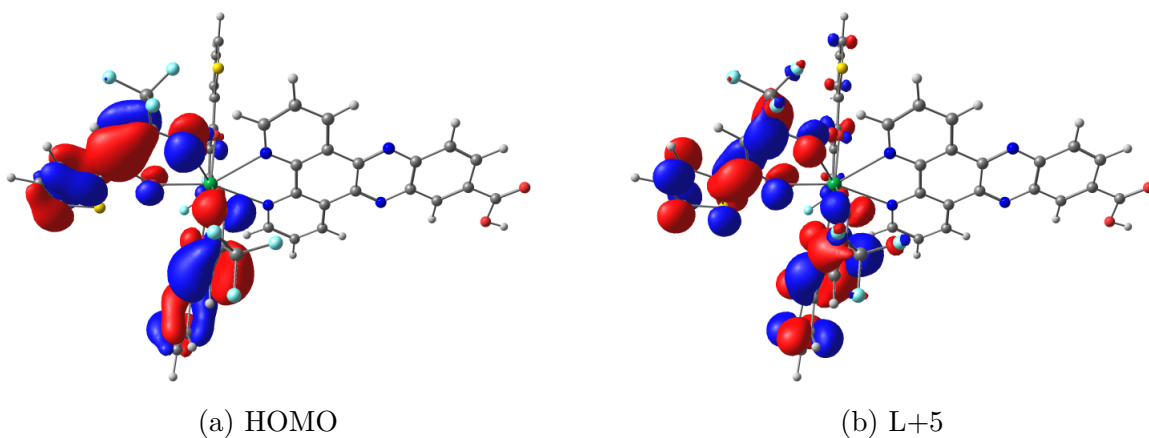

(a) HOMO   (b) L+5
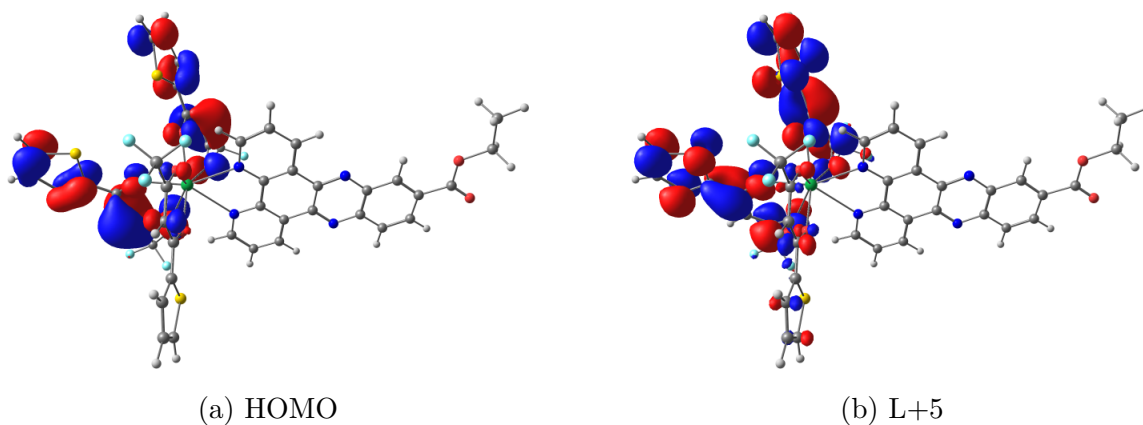
Figure 67: The second dominant transition is the HOMO (a) orbital to the L+5 (b) orbital, which is (ILCT)[π(TTA) $\rightarrow$ π*(TTA)] in character.

The energy for the S_1 state was calculated to be 2.5753 eV. The T_1 energy was calculated to be 2.2675 eV. The T_1 state is attributed to DPPZ-EE localized $\pi \rightarrow \pi$* transition.
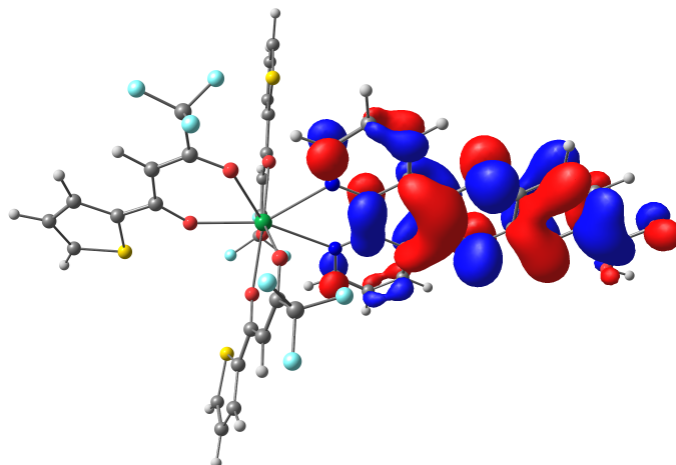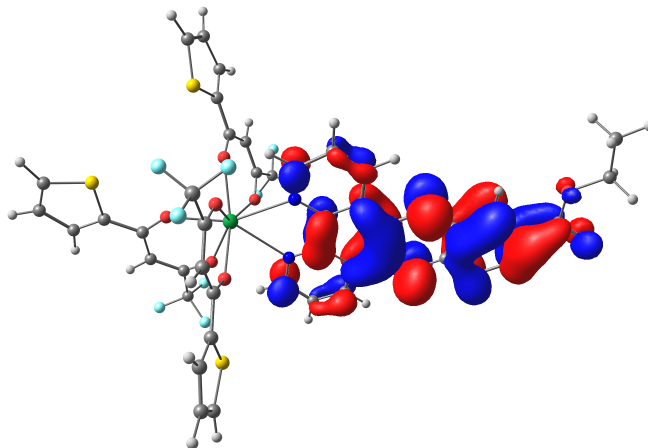
Figure 68: Ethyl ester triplet orbital.

Based on the calculated values of the lowest S_1 and T_1 states and based on a value of 2.0193 eV for the $^5D_0 \rightarrow ^7F_2$ energy, ΔE_{ISC} and ΔE_{ET} can be calculated for Eu_EE. The energy of intersystem crossing ΔE_{ISC} was calculated to be 0.3078 eV. The energy transfer to gap ΔE_{ET} was calculated to be 0.2482 eV.

Eu(TTA)$_3$DPPZ-NO$_2$
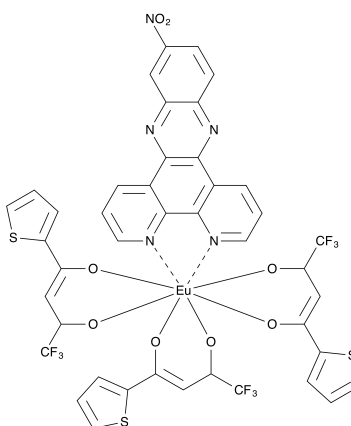
Figure 69: Structure of Eu_NO2

In this section calculated singlet state and triplet state results for the nitro substituted DPPZ (DPPZ-NO$_2$) are presented for the Eu(TTA)$_3$DPPZ-NO$_2$ (Eu_NO2) complex and compared with experimentally determined absorption data. The orbital transitions involved

in the excited state at 323.14 nm are presented in Table 14. There are two dominant transitions that contribute to the excited state, which are visualized in Figure 70 and in Figure 71.

Table 14: The orbital transitions and contribution to the λ_{max} = 323.14 nm excited state of Eu_NO2.

HOMO Orbital		LUMO Orbital	% Contribution
H - 12	$\rightarrow$	L + 3	3.83
H - 12	$\rightarrow$	L + 5	5.82
H - 9	$\rightarrow$	L + 3	3.00
H - 9	$\rightarrow$	L + 5	6.39
H - 7	$\rightarrow$	L + 3	2.57
H - 7	$\rightarrow$	L + 5	4.79
H - 2	$\rightarrow$	L + 3	5.37
H - 2	$\rightarrow$	L + 4	4.69
H - 2	$\rightarrow$	L + 5	20.2
H - 1	$\rightarrow$	L + 3	8.05
HOMO	$\rightarrow$	L + 6	24.0

(a) H-2

(b) L+5
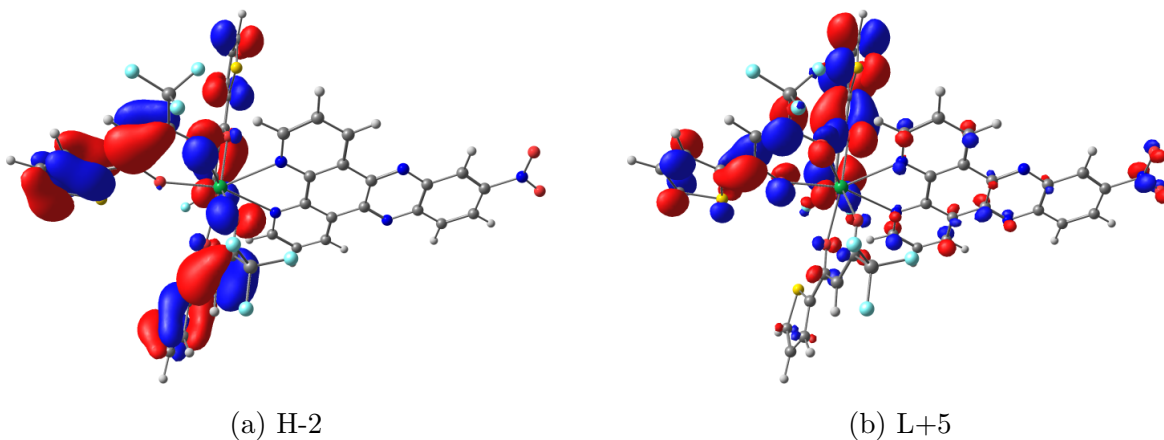
Figure 70: The first dominant transition is the H-2 (a) orbital to the L+5 (b) orbital, which has (ILCT)$[\pi(\text{TTA}) \rightarrow \pi^*(\text{TTA})]$ character as well as (LLCT)$[\pi(\text{TTA}) \rightarrow \pi^*(\text{DPPZ})]$ due to a minimal amount of charge density on the DPPZ ligand.
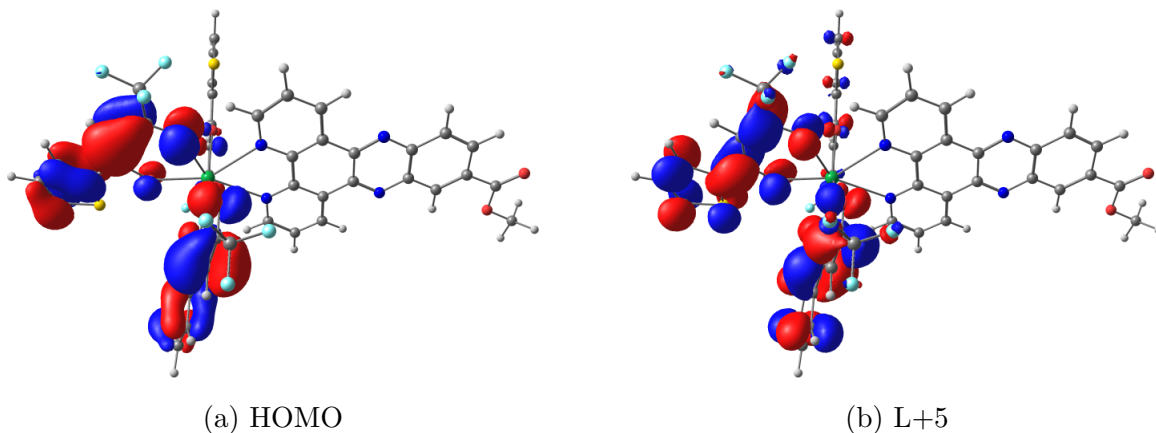
(a) HOMO   (b) L+6
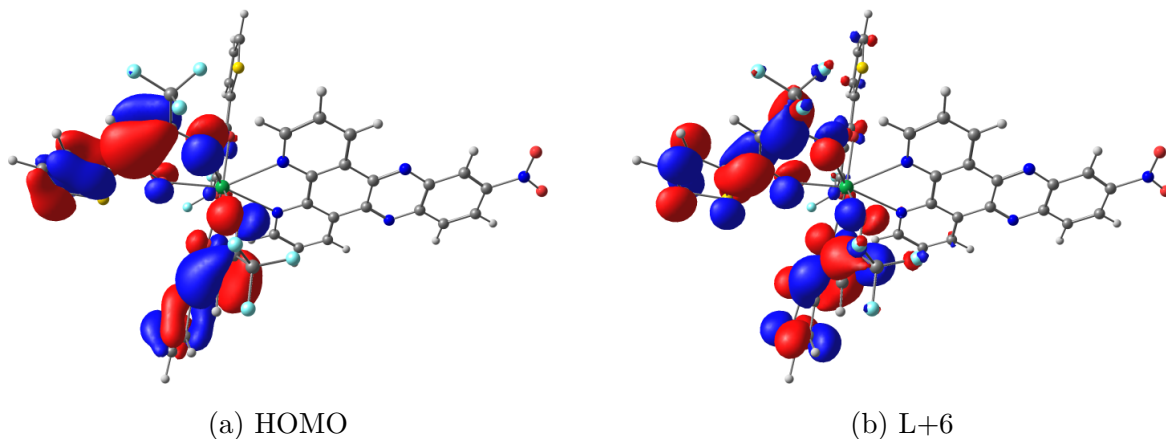
Figure 71: The second dominant transition is the HOMO (a) orbital to the L+5 (b) orbital, which is (ILCT)$[\pi(\text{TTA}) \rightarrow \pi^*(\text{TTA})]$ in character.

The energy of the S_1 state was calculated to be 2.2178 eV. The T_1 energy was calculated to be 2.2147 eV. The T_1 state is attributed to DPPZ-NO$_2$ localized $\pi \rightarrow \pi^*$ transition.
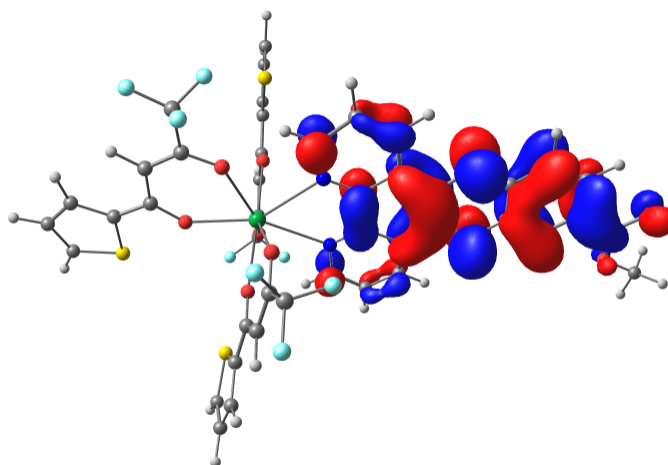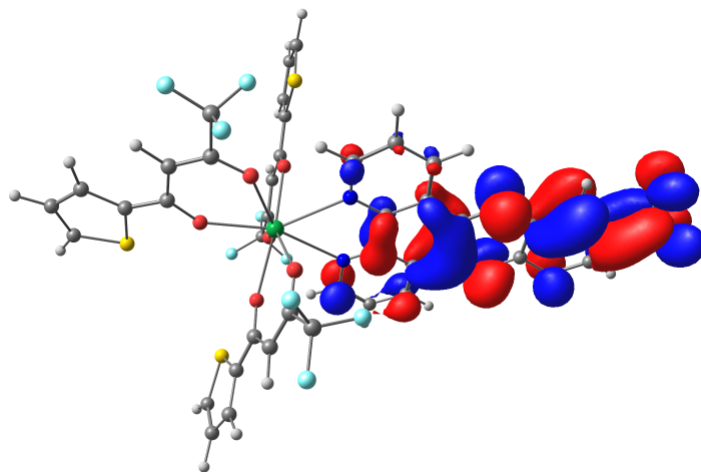

Figure 72: EU_NO2 triplet orbital.

Based on the calculated values of the lowest S_1 and T_1 states and based on a value of 2.0193 eV for the $^5D_0 \rightarrow ^7F_2$ energy, ΔE_{ISC} and ΔE_{ET} can be calculated for Eu_NO2. The energy of intersystem crossing ΔE_{ISC} was calculated to be 0.0031 eV. The energy transfer gap ΔE_{ET} to Eu_NO2's excited state is calculated to be 0.1954 eV.

For all nine complexes the $S_0 \rightarrow S_1$ transition is $\pi \rightarrow \pi^*$ where the HOMO orbital

is located on the TTA ligands and the LUMO orbital is located on the DPPZ ligand (see Appendix E). This indicates that the substituents do not have any great affect on the locality of the S_1 state. The oscillator strength for the $S_0 \rightarrow S_1$ is considerably low indicating that this transition does not play any major role in the absorption spectra.

According to the singlet state and triplet state data initial excitation is from the HOMO, H-1, and H-2 orbitals located on the TTA ligands to the L+3, L+4, and L+5 orbitals also located on the TTA ligands. Referring back to Figure 9 the HOMO, H-1, and H-2 orbitals are all relatively close in energy and unaffected by the ligand substituents. On the other hand there is a large gap in energy between the LUMO and L+1 orbitals. As previously mentioned the energy of the LUMO orbital shows significant dependence on the ligand substituents while the L+1 orbital energy remain relatively unaffected. A notable exception being the Eu_NO2 complex. The effect that the substituents have on the LUMO orbitals and the L+1 and orbitals is not surprising given that the locality of the L+1 orbitals are located on TTA and the LUMO orbital is located on DPPZ.

CALCULATED ΔE_{ISC} AND ΔE_{ET}

Effective sensitization is dependent on several factors. It has been shown that the triplet state energy plays an important role in the efficiency of ligand sensitization[48]. In trying to determine whether intersystem crossing and energy transfer gaps, which depend on the T_1 energy, are effective at sensitizing europium's excited state we must turn to the studies of Latva[48] and Reinhoudt[49], referred to as Latva's empirical rule and Reinhoudt's empirical rule. Based off of trends of luminescent lanthanide complexes with different sensitizer ligands a range of energies were proposed for ideal ΔE_{ISC}, ΔE_{ET} energy gaps. The Reinhoudt empirical rule states that effective sensitization occurs when ΔE_{ISC} is greater than 0.62 eV. The Latva empirical rule states that effective sensitization occurs when ΔE_{ET} is within the range of 0.25 - 0.43 eV. Table 15 summarizes the S_1, T_1, ΔE_{ISC}, and ΔE_{ET} energies.

Table 15: Calculated lowest S_1 and T_1 state energies and ΔE_{ISC} and ΔE_{ET} energy gaps. The $^5D_0 \to {}^7F_2$ transition is used as reference at 2.0193 eV^2. (Blue text indicate quantum yield data available.)

Complex	S_1 (eV)	T_1 (eV)	ΔE_{ISC} (eV)	ΔE_{ET} (eV)
Eu_NH2	2.8868	2.1065	0.7803	0.0872
Eu_MeO	2.8417	2.3256	0.5161	0.3063
Eu_CH3	2.7911	2.3183	0.4728	0.2990
Eu_H	2.7205	2.3033	0.4172	0.2840
Eu_Br	2.6008	2.2868	0.3140	0.2675
Eu_COOH	2.5000	2.2722	0.2278	0.2529
Eu_ME	2.5607	2.2680	0.2927	0.2487
Eu_EE	2.5753	2.2675	0.3078	0.2482
Eu_NO2	2.2178	2.2147	0.0031	0.1954

Figure 73 illustrates the S_1, T_1, ΔE_{ISC}, and ΔE_{ET} energies with reference to the $^5D_0 \to {}^7F_2$ energy of Eu(III). For a reference complex with a good quantum yield we look at Eu(TTA)$_3$Phen. In the paper by Nockemann et $al.$[45] the authors used a direct measurement method with an integrating sphere. With Eu(TTA)$_3$Phen being dissolved in dimethylformamide the authors measured a quantum yield of 36.5 %. In the paper by Nolasco[10] the authors calculated the Eu(TTA)$_3$Phen S_1 and T_1 energy of 3.2457 eV and 2.3393 eV respectively, which gives ΔE_{ISC} and ΔE_{ET} of 0.9063 eV and 0.2068 eV respectively.
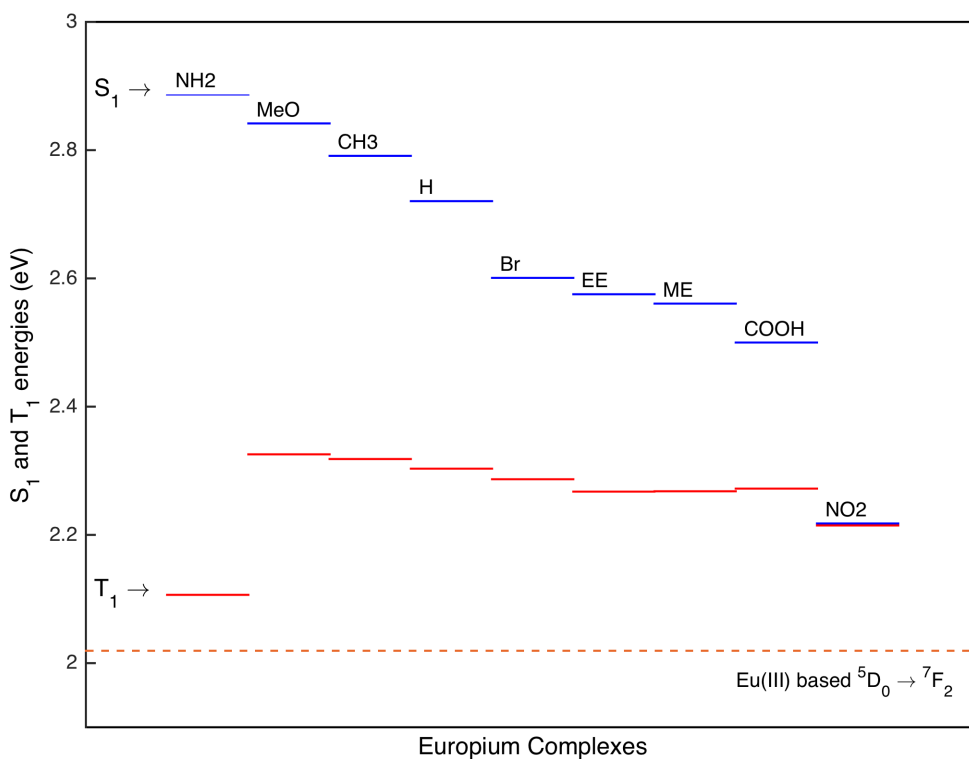
Figure 73: S_1 and T_1 energies of each complex.

The ΔE_{ISC} energy gap for all the complexes fall between 0.78 - 0.003 eV as illustrated in Table 15. The ΔE_{ISC} of 0.9063 eV for $Eu(TTA)_3Phen$ and the empirical threshold value of 0.62 eV suggest that there will be an increase of energy back transfer for all of the complexes except for Eu_NH2 with a ΔE_{ISC} value of 0.7803 eV. This suggests that effective energy transfer will not occur resulting in a decrease in luminescence quantum yield. The ΔE_{ET} energy gap for the complexes all fall within the threshold of 0.25 - 0.43 eV to have effective energy transfer except for Eu_NH2 and Eu_NO2, which are below the acceptable threshold value. The ΔE_{ET} energy gap for $Eu(TTA)_3Phen$ is also below the threshold value with a ΔE_{ET} of 0.2068. In comparing the results in this study to the results in Nockemann and Nolasco it appears as though the ΔE_{ISC} has the greatest effect on the complexes ability to

sensitize Eu(III)'s excited states. This can be seen by how the ligand substiuents affect the S_1 energy in Figure 73

According to the Latva empirical rule the calculated ΔE_{ET} energies suggest that all of the complexes would have effective charge transfer, with some exceptions. The first exception is Eu_NH2 which has a ΔE_{ET} of 0.0872 eV. Because the ΔE_{ET} is so small it is expected to have significant energy back transfer, suggesting emission from T_1 or non-radiative deactivation. The other potential exception would be Eu_NO2. With a ΔE_{ET} of 0.1954 eV the energy gap is slightly below the threshold suggested by Latva, suggesting decreased luminescent quantum yields due to energy back transfer.

There are some interesting trends that are revealed when considering ΔE_{ISC} and ΔE_{ET} in regards to the electron withdrawing and electron donating characteristics of the various ligand substituents. Figure 73 clearly shows that the greatest effect that the substituents have is on the S_1 energy levels with the greatest effect on the S_1 occurring with Eu_NO2. The T_1 energy is only marginally affected except for Eu_NH2 who's triplet state energy is greatly affected by the substituent. Eu_NO2 also has a more modest effect on the T_1 energy but not to the extent that Eu_NH2 does. The common factor relating these two substituents is the presence of the nitrogen atom with the main difference being the oxygen atoms as opposed to the hydrogen atoms. It is possible that the shift affecting the S_1 and T_1 states is indicative of the differences between resonance and inductive effects of the substituents. The electron donating effect of an amine group is through resonance of its lone pair of electrons, and the electron withdrawing effects of the nitro group are primarily inductive due to the positive charge on the nitrogen and to a lesser extent some resonance effects.

Figure 73 also illustrates how ΔE_{ISC} is lower with respect to Eu_H for the electron withdrawing groups (Eu_Br, Eu_COOH, Eu_EE, Eu_Me, and Eu_NO2), and there is an increase of ΔE_{ISC} with respect to Eu_H for the electron donating groups (Eu_MeO and Eu_CH3). The trend for the ΔE_{ET} follows a similar pattern as ΔE_{ISC}, though the effect

is marginalized owing to the T_1 energy being relatively unaffected by the substituents. The ΔE_{ET} is lower with respect to Eu_H for the electron withdrawing groups (Eu_Br, Eu_COOH, Eu_EE, Eu_Me, and Eu_NO2). Contrasting this trend is an increase in ΔE_{ET} with respect to Eu_H for the electron donating groups (Eu_MeO, and Eu_CH3) except for Eu_NO2, which shows a dramatic decrease in T_1 energy as illustrated in Figure 73. This increase in ΔE_{ET} as a result of the increase in the T_1 energy can explained by a resonance and inductive (in the case of Eu_CH3) stabilization of the T_1 orbital.

4.4 Luminescent Quantum Yield

Luminescent quantum yield measurements were done for the five complexes that had been synthesized with $Eu(TTA)_3Phen$ as the reference standard. The mean quantum yield measurements and their standard deviations are summarized in the Table 16.

Table 16: Experimental quantum yield measurements.

Complex	Quantum Yield (%)	Std. Dev.
Eu_Br	6.84	0.90
Eu_H	6.84	2.8
Eu_EE	3.76	0.90
Eu_ME	3.38	0.58
Eu_NO2	9.27	3.7

All of the ligands that have had their quantum yield measured have electron withdrawing substituents. Electron withdrawing groups decrease the ΔE_{ISC} and ΔE_{ET} energy gaps as explained above and illustrated in Figure 73. This points to the expectation that the quantum yields will decrease with respect to Eu_H especially when compared to the ΔE_{ISC} and ΔE_{ET} of $Eu(TTA)_3Phen$ detailed in Nolasco and Nockemann primarily due to energy back transfer from low ΔE_{ISC}.

The results of quantum yield measurements confirm this trend. This is also reflected in the Figure 73 where there is a clear decrease in S_1 energy relative to Eu_H. A notable

exception is the quantum yield of Eu_NO2. Despite being an electron withdrawing group Eu_NO2 presents a comparable quantum yield to Eu_H. A plausible reason is that since the S_1 and T_1 energies are only separated by 0.0031 eV intersystem crossing is bypassed and a direct energy transfer from the S_1 state to europium's $^5D_0$ excited state could occur.
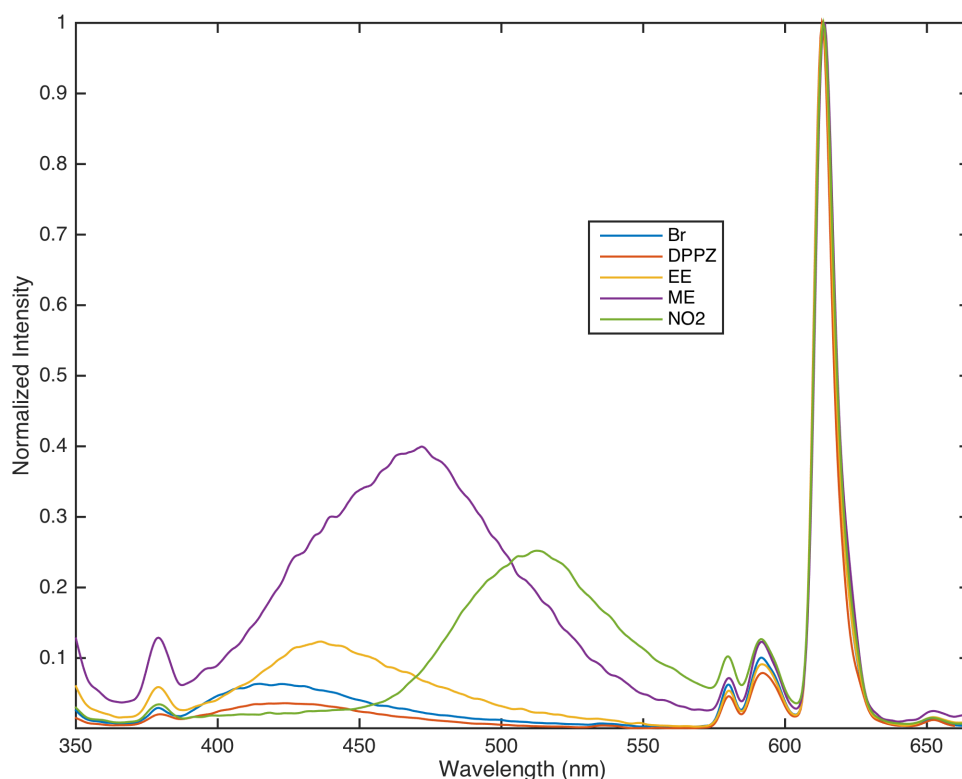
Figure 74: Normalized luminescence

In Figure 74 the luminescence spectra are normalized and plotted against each other. Regarding the S_1 energies of the complexes in reference to Eu_H we see that the S_1 energy decreases in the order of Eu_H > Eu_Br > Eu_EE > Eu_ME > Eu_NO2. The decrease in S_1 energy corresponds to an increase in the redshift of the ligand based luminescence where Eu_NO2 has the greatest redshift when compared to the ligand based emission λ_{max}.

There is also an increase in the amount of ligand based luminescence that also follows the

trend of decreased S_1 energy up to Eu_ME. The Eu_NO2 complex, however, shows a decrease in overall ligand based luminescence. The overall increase in ligand based luminescence is attributed to increased energy back-transfer promoted by a decrease in the ΔE_{ISC} gap primarily due to the effect that the substituents have on the S_1 state. The decrease in overall ligand based luminescence for Eu_NO2 as previously stated is thought to be from an alternate energy transfer pathway. This pathway is thought to be facilitated by the narrow energy gap between the S_1 state and the T_1 state as a result of the nitro group's effect on the singlet state energy. The increased quantum yield of Eu_NO2 and the decrease in ligand based luminescence combined with the value of the ΔE_{ISC} energy gap are strong indicators supporting an alternate energy transfer process.

DFT calculations have been used to investigate the electronic properties of a series of Eu(TTA)$_3$DPPZ-R complexes where R is a series of substituents with various electron donating/withdrawing characteristics. Optimized ground state geometries were performed. Comparison of the calculated molecular geometry of Eu_EE to the X-ray crystal structure showed good agreement. Good agreement was also seen between calculated structures of Eu_H and Eu_CH3 from Li[16]. Incorporation of electron donating groups (NH$_2$, MeO, and CH$_3$) increased the energy of the HOMO orbital, LUMO orbital, and increased the HOMO-LUMO energy gap. Incorporation of electron withdrawing groups (Br, COOH, EE, ME, NO$_2$) decreased the HOMO and LUMO energy as well as decreasing the HOMO-LUMO energy gap.

TD-DFT calculations have been done to determine excited state properties. Excited state oscillator strengths have been plotted in nm and eV. Normalized experimental absorption spectra are plotted with singlet state oscillator strengths. The calculated lowest energy λ_{max} shows good agreement with the experimental lowest energy λ_{max}. The dominant orbital transitions for the lowest energy λ_{max} are almost exclusively $[\pi(\text{TTA}) \rightarrow \pi^*(\text{TTA})]$ transitions indicative of intra-ligand charge transfer. The dominant transition for Eu_NH2 lowest energy λ_{max} is $[\pi(\text{DPPZ-NH2, TTA}) \rightarrow \pi^*(\text{TTA})]$ making it ligand-to-ligand charge transfer in character with some intra-ligand charge transfer.

Lowest energy S$_1$ and T$_1$ were determined by TD-DFT calculations. Within the context of Reinhoudt's empirical rule the only complex that meets this criteria is Eu_NH2 with a ΔE_{ISC} of 0.7803 eV. The Latva empirical rule shows that there is a sufficiently large ΔE_{ET} for all the complexes, except for Eu_NH2, for effective energy transfer. Results also show that for electron withdrawing groups the ΔE_{ISC} and ΔE_{ET} energies decrease with respect to Eu_H. For the electron donating groups the ΔE_{ISC} and ΔE_{ET} will increase with respect

to Eu_H, the only exception being Eu_NH2. The substituents have the greatest effect on the S_1 energy levels. The electron donating groups have higher S_1 energies than Eu_H while the electron withdrawing groups have lower S_1 energies than Eu_H. These lower energies increase the probability of energy back transfer from the T_1 state, which stays relatively unaffected to the substituent effect except for Eu_NH2 and Eu_NO2 to a lesser extent. The lack of energy transfer efficiency can be seen in the lower quantum yields relative to Eu_H as well as the amount of ligand based emission as illustrated in Figure 74 which also corresponds to a redshifting of the ligand based emission. The Eu_NO2 complex shows a decrease in ligand based emission and a comparable quantum yield measurement to Eu_H. Considering the S_1 energy level of Eu_NO2 with the reduction in its ligand based emission it is very likely that energy transfer is occurring through some alternate path such as direct sensitization of Eu(III)'s $^5D_0$ from the ligand based S_0 state.

CHAPTER 6:   FUTURE WORK

We need to collect more data. In order to fully understand how the electron withdrawing/donating characteristics affect the luminescent quantum yield of DPPZ more electron withdrawing groups and electron donating groups should be synthesized, particularlly electron donating groups to get a better balance of substituent characteristics. In addition to collecting quantum yield data on any new complexes, effort should be devoted to getting better more reproducible quantum yield measurements for the complexes that are currently available.

A Geometry Optimization Input File

Sample Gaussian 09 input file for a DFT geometry optimization.

```
1  %nprocshared=16

2  %mem=14GB

3  %chk=<user defined checkpoint file>.chk

4  #p opt=(maxcycle=250) b3lyp/gen pseudo=read nosymm geom=connectivity

5  integral=(ultrafinegrid,acc2e=12) ...
       scf=(novaracc,xqc,maxconventionalcycle=300)

6

7  <user defined calculation title>

8

9  0 1

10

11  <XYZ coordinates of the molecule>

12

13  <Bond connectivity and order>

14

15  S O C N F H 0

16  6-31+G**

17  ****

18  Eu 0

19  MWB52

20  ****

21

22  Eu 0

23  MWB52
```

B   Example Geometry Optimization Output

Example of output for a successful geometry optimization.

```
1          Item               Value     Threshold  Converged?

2   Maximum Force          0.000007    0.000450      YES

3   RMS     Force          0.000001    0.000300      YES

4   Maximum Displacement   0.001221    0.001800      YES

5   RMS     Displacement   0.000260    0.001200      YES

6   Predicted change in Energy=-5.291874D-09

7   Optimization completed.

8      -- Stationary point found.

9                           ---------------------------

10                         !   Optimized Parameters   !

11                         ! (Angstroms and Degrees)  !

12  -------------------------                          ...
      -------------------------

13  ! Name  Definition            Value        Derivative Info. ...
                    !

14  ------------------------------------------------------------------

15  ! R1    R(1,5)               2.4163       -DE/DX =    0.0 ...
                    !

16  ! R2    R(1,6)               2.4124       -DE/DX =    0.0 ...
                    !

17  ! R3    R(1,8)               2.389        -DE/DX =    0.0 ...
                    !

18  ! R4    R(1,9)               2.4221       -DE/DX =    0.0 ...
                    !

19  ! R5    R(1,17)              2.6769       -DE/DX =    0.0 ...
                    !
```

The program will then write to file all of the geometric parameters including bond lengths, bond angles, dihedral angles, cartesian coordinates of each atom, orbital energy eigenvalues, Mulliken charges, and dipole moment. Programs such as GaussView or ChemCraft can be used to parse the out .log and .chk files to extract the computational data. The checkpoint file (.chk) is used in the TD-DFT calculations for the excited state geometry.

C Excited State Input File

Sample Gaussian 09 input file for a singlet state calculation. The singlet state calculation reads the basis set and geometry (line 5) from the checkpoint file of the geometry optimization (line 3). To calculate the triplet states simply amend line 5 with td=(triplet). The default number of states that Gaussian will search for is three, so it is not necessary to specify the number of states since we are only interested in the lowest T_1 state.

```
1   %nprocshared=16

2   %mem=14GB

3   %oldchk=eu_dppz_singlet2.chk

4   %chk=eu_dppz_singlet3.chk

5   #p td=(singlet,nstates=150) b3lyp/checkbasis pseudo=read

6   nosymm geom=checkpoint integral=(ultrafinegrid,acc2e=12)

7   scf=(novaracc,xqc,maxconventionalcycle=300)

8

9   eu dppz singlet

10

11   0 1
```

D   Excited State Output

```
1    Excited state symmetry could not be determined.

2    Excited State  29:      Singlet-?Sym    3.8335 eV  323.42 nm  f=0.0445 ...
        <S**2>=0.000

3        232 -> 246       -0.14060

4        233 -> 246       -0.24792

5        234 -> 246        0.26631

6        235 -> 246        0.51308

7        236 -> 246        0.12951

8        238 -> 246        0.14571

9        243 -> 250       -0.10125

10       245 -> 251        0.10788

11

12   Excited state symmetry could not be determined.

13   Excited State  30:      Singlet-?Sym    3.8361 eV  323.21 nm  f=0.6253 ...
        <S**2>=0.000

14       233 -> 246        0.11941

15       235 -> 246       -0.17070

16       240 -> 247        0.10527

17       243 -> 248       -0.20264

18       243 -> 249        0.12972

19       243 -> 250       -0.34869

20       244 -> 248       -0.19693

21       244 -> 249        0.11031

22       245 -> 251        0.37499
```

The example singlet state output is from Eu_H. There are two states displayed (S_{29} and S_{30}).
Since the symmetry of the molecule was not considered in the calculation (Gaussian keyword:
nosymm) symmetry data is not displayed. The excited state energy is displayed in eV along

with wavelength responsible for the excitation. The oscillator strength f is the probability of the absorption occurring. The <S**2>=0.000 value is the spin contamination of the state, since this is a singlet state there is no spin contamination. Next are displayed the orbitals involved in the excited state along with configuration interaction expansion coefficients.

E   Sample Stampede Batch File

```bash
1  #!/bin/bash

2  #SBATCH -J dppz # Job Name

3  #SBATCH -o job_dppz.%j # Output file name (%j expands to jobID)

4  #SBATCH -e error_dppz.%j # Error file name (%j expands to jobid)

5  #SBATCH -N 1 # Gaussian only uses one node

6  #SBATCH -n 16 # Number of MPI tasks requested

7  #SBATCH -p normal # Queue name -- normal, development, etc.

8  #SBATCH -t 48:00:00 # Run time (hh:mm:ss)

9  #SBATCH -A TG-CHE150032 # You can remove this line if you only have one ...
       allocation

10

11 # make sure we have the module loaded:

12 module load gaussian

13

14

15 # timestamps are helpful

16 echo "job started on $(date)"

17

18 export GAUSS_SCRDIR=$SCRATCH/gaussianTmp/

19

20 # now run Gaussian:

21 g09 < eu_dppz.gjf > eu_dppz.log

22

23 echo "job finished on $(date)"
```

F MATLAB Code

Custom MATLAB program used to make Figures 9 and 73.

```matlab
1  load('MOenergyALL');
2  ev = MOenergyALL;
3  [x,y] = size(ev);
4
5  set(gca,'xtick',[])
6  set(gca,'xcolor',[1 1 1])
7
8  subs = {'Amine' 'Bromo' 'COOH' 'DPPZ' 'EthEster' 'MeEster' 'MeO' ...
       'Nitro' 'Methyl'};
9  k = 0;
10
11 for i = 1:y
12
13     if ev(1,i) == 0
14
15         plot([i (i+1)],[0 0],'w')
16
17     else
18
19         k = k + 1;
20
21         for j = 1:x
22
23             plot([i (i+1)],[ev(j,i) ev(j,i)],'k')
24
25         end
26
27         xval = (i);
28         yval = .25;
29         text(xval,yval,subs(k),'FontSize',10)
30
31     end
32
33 end
34
35 axis tight
36 xlabel('Molecular Orbitals','Color','Black','Fontsize',12)
37 ylabel('Orbital Energy / eV','Color','Black','Fontsize',12)
```

REFERENCES

[1] Binnemans, K. *Coord. Chem. Rev.* **2015**, *295*, 1–45.

[2] Aiga, F.; Iwanaga, H.; Amano, A. *J. Phys. Chem.* **2007**, *111*, 12141–12145.

[3] Martin, R. M. *Electronic Structure*; Cambridge University Press, 2008.

[4] Cramer, C. J. *Essentials of Computational Chemistry*, 2nd ed.; John Wiley & Sons, Ltd, 2004.

[5] Bünzli, J.-C.; Piquet, C. *Chem. Soc. Rev.* **2005**, *34*, 1048 – 1077.

[6] Wang, L.; Li, B.; Zhang, L.; Li, P.; Jiang, H. *Dyes Pigments* **2013**, 26–31.

[7] Tang, C. W.; VanSlyke, S. A. *Appl. Phys. Lett.* **1987**, *51*, 913 – 915.

[8] Hagan, A. K.; Zuchner, T. *Anal. Bioanal. Chem.* **2011**, *400*, 2847 – 2864.

[9] Phillips, T.; Haq, I.; Meijer, A. J. H. M.; Adams, H.; Soutar, I.; Swanson, L.; Sykes, M. J.; Thomas, J. A. *Biochem.* **2004**, *43*, 13657 – 13665.

[10] Nolasco, M. M.; Vaz, P. D.; Carlos, L. D. *New J. Chem.* **2011**, *35*, 2435 – 2441.

[11] Zhang, S.; Winter, P.; Wu, K.; Sherry, A. D. *J. Am. Chem. Soc.* **2001**, *123*, 1517 – 1518.

[12] Freund, C.; Porzio, W.; Giovanella, U.; Vignali, F.; Pasini, M.; Destri, S. *Inorg. Chem.* **2011**, *50*, 5417 – 5429.

[13] Dasari, S.; Patra, A. K. *Dalton Trans.* **2015**, *44*, 19844 – 19855.

[14] Greco, C.; Moro, G.; Bertini, L.; Biczysko, M.; Barone, V.; Cosentino, U. *J. Chem. Theory and Comp.* **2014**, *10*, 767 – 777.

[15] Dolg, M.; Stoll, H.; Preuss, H. *J. Chem. Phys.* **1989**, *90*, 1730 – 1734.

[16] Li, X.-N.; Wu, Z.-J.; Si, Z.-J.; Liang-Zhou,; Liu, X.-J.; Zhang, H.-J. *Phys. Chem. Chem. Phys.* **2009**, *11*, 9687 – 9695.

[17] Atkins, P.; Paula, J. D. *Physical Chemistry*, 10th ed.; Oxford University Press, 2014.

[18] Rosse, D. V., Ed. *Focus on Materials Science Research*; Nova Science Publishers, Inc., 2007.

[19] Souza, A.; dos Santos, M. C. *Chem. Phys. Lett.* **2012**, *521*, 138 – 141.

[20] Berry, M. T.; Reid, M. R.; Richardson, F. S. *J. Chem. Phys.* **1986**, *84*, 2917–2925.

[21] Thomas, L. *Proc. Camb. Phil. Soc.* **1927**, *23*, 542.

[22] Fermi, E. *Rend. Accad. Naz. Lincei* **1927**, *6*, 602.

[23] Born, M.; Oppenheimer, J. R. *Annalen der Physik* **1927**, *389*, 457–484.

[24] Slater, J. C. *Phys. Rev.* **1951**, *81*, 385–390.

[25] Bloch, F. *Physik* **1929**, *57*, 545.

[26] Dirac, P. A. M. *Proc. Camb. Phil. Soc.* **1930**, *26*, 376.

[27] Hohenberg, P.; Kohn, W. *Phys. Rev.* **1964**, *136*, B864.

[28] Kohn, W.; Sham, L. J. *Phys. Rev.* **1965**, *140*, A1133.

[29] Runge, E.; Gross, E. K. U. *Phys. Rev. Lett.* **1984**, *52*.

[30] Ullrich, C. *Time-Dependent Density-Functional Theory*; Oxford University Press, 2012.

[31] Frisch, M. J. et al. Gaussian Inc. Wallingford CT 2016.

[32] Ditchfield, R.; Hehre, W. J.; Pople, J. A. *J. Chem. Phys.* **1971**, *54*, 724.

[33] Hehre, W. J.; Ditchfield, R.; Pople, J. A. *J. Chem. Phys.* **1972**, *56*, 2257.

[34] Hariharan, P. C.; Pople, J. A. *Theor. Chem. Acc.* **1973**, *28*, 213 – 22.

[35] Hariharan, P. C.; Pople, J. A. *Mol. Phys.* **1974**, *27*, 209 – 14.

[36] Gordon, M. S. *Chem. Phys. Lett.* **1980**, *76*, 163 – 68.

[37] Francl, M. M.; Pietro, W. J.; Hehre, W. J.; Binkley, J. S.; DeFrees, D. J.; Pople, J. A.; Gordon, M. S. *J. Chem. Phys.* **1982**, *77*, 3654 – 65.

[38] Jr., R. C. B.; Curtiss, L. A. *J. Comp. Chem.* **1990**, *11*, 1206 – 16.

[39] Blaudeau, J. P.; McGrath, M. P.; Curtiss, L. A.; ; Radom, L. *J. Chem. Phys.* **1997**, *107*, 5016 – 21.

[40] Rassolov, V. A.; Pople, J. A.; Ratner, M. A.; Windus, T. L. *J. Chem. Phys.* **1998**, *109*, 1223 – 29.

[41] Rassolov, V. A.; Ratner, M. A.; Pople, J. A.; Redfern, P. C.; Curtiss, L. A. *J. Comp. Chem.* **2001**, *22*, 976 –84.

[42] Lee, C.; Yang, W.; Parr, R. G. *Phys. Rev. B.* **1988**, *37*, 785?789.

[43] Nockemann, P.; Beurer, E.; Driesen, K.; Deun, R. V.; Hecke, K. V.; Meervelt, L. V.; Binnenmans, K. *Chem. Commun.* **2005**, 4354–4356.

[44] Demas, J. N.; Crosby, G. A. *J. Phys. Chem.* **1971**, *75*.

[45] Nockemann, P.; Beurer, E.; Driesen, K.; Deun, R. V.; Hecke, K. V.; Meervelt, L. V.; Binnemans, K. *Chem. Commun.* **2005**, 4354–4356.

[46] Silva, C. R. D.; Li, J.; Zheng, Z.; Corrales, L. R. *J. Phys. Chem. A* **2008**, *112*, 4527–4530.

[47] Sun, P.-P.; Duan, J.-P.; Lih, J.-J.; Cheng, C.-H. *Adv. Funct. Mater.* **2003**, *13*, 683 – 691.

[48] Latva, M.; Takalo, H.; V.-M.Mukkala,; Matachescuc, C.; Rodriquez-Ubisd, J. C.; Kankarea, J. *J. Lumin.* **1997**, *75*, 149.

[49] Steemers, F. J.; Verboom, W.; Reinhoudt, D. N.; van der Tol, E. B.; Verhoeven, J. W. *J. Am. Chem. Soc.* **1995**, *117*, 9408–414.